# Dynamic Scanning Probe Lithography and Its Applications

by

Resul Saritas

A thesis
presented to the University of Waterloo
in fulfillment of the
thesis requirement for the degree of
Doctor of Philosophy
in
Systems Design Engineering

Waterloo, Ontario, Canada, 2022

**Examining Committee Membership**

The following served on the Examining Committee for this thesis. The decision of the Examining Committee is by majority vote.

| | |
|---|---|
| External Examiner: | Ridha Ben Mrad<br>Professor, Dept. of Mechanical and Industrial Engineering,<br>University of Toronto |
| Co-Supervisor: | Eihab M. Abdel-Rahman<br>Professor, Dept. of Systems Design Engineering,<br>University of Waterloo |
| Co-Supervisor: | Mustafa Yavuz<br>Professor, Dept. of Mechanical and Mechatronics Engineering,<br>University of Waterloo |
| Internal Member: | Parsin Haji Reza<br>Assistant Professor, Dept. of Systems Design Engineering,<br>University of Waterloo |
| Internal-External Member: | Dongqing Li<br>Professor, Dept. of Mechanical and Mechatronics Engineering,<br>University of Waterloo |
| Internal-External Member: | Dayan Ban<br>Professor, Dept. of Electrical and Computer Engineering,<br>University of Waterloo |

## Author's Declaration

I hereby declare that I am the sole author of this thesis. This is a true copy of the thesis, including any required final revisions, as accepted by my examiners.

I understand that my thesis may be made electronically available to the public.

## Abstract

This dissertation presents a novel, benchtop, low-cost, high-throughput direct surface patterning method dubbed dynamic-Scanning Probe Lithography (d-SPL). It employs a scriber mounted via a spring-damper mechanism to a nano-resolution 3D stage. As the scriber traverses the substrate surface, non-uniformity in the surface morphology leads to time-variation in the magnitude and direction of the contact force, which in turn generates scriber vibrations. The spring-damper mechanism dissipates those vibrations and stabilizes the contact force, thereby enabling long and uniform micro and nano patterns on a wide variety of substrates and preventing scriber tip failure.

An analytical model was developed to investigate the dynamics of d-SPL and determine its safe operation conditions and limitations. It was used to investigate and explain, for the first time, a small micro-scale chatter phenomenon observed in the response of d-SPL. The model was validated through comparison to experiments.

d-SPL was utilized for high velocity fabrication of micro and nanochannels at 1 mm/s. The channel dimensions are controlled by the scriber surface contact force. d-SPL also provided the basis for a novel rapid fabrication method that enhances the output power of triboelectric nanogenerators (TENGs) by simultaneously creating centimeter-long nano grooves (NGs) and nano triangular prisms (NTPs) on the surface of polymeric triboelectric materials. The output power of the nano structured TENGs was 12.2 mW compared to 2.2 mW for flat TENGs. A coupled electromechanical model was developed to describe the energy flow through the TENGs. Analytical and experimental results for the proposed TENGs show that they can harvest low-frequency and wide-band vibrations below 10 Hz.

d-SPL can also fabricate long micro and nano wires through a continuous chip removal process. The wire dimensions can be controlled via the tip-substrate contact force while

taking into account the substrate material. Continuous chip removal produced millimeter long, helical shaped gold nano wires out of a 600 nm thick gold layer on a dielectric substrate. Continuous flexible helical polymeric micro wires were obtained by chip removal from a Poly (methyl methacrylate) (PMMA) substrate. The wires were coated with 50 nm Silver (Ag) layer to produce flexible conductive micro-helical wires. It was found that these wires can behave as freely standing cantilever beams.

A low-cost and rapid fabrication of back-gated field effect transistors (BGFETs) was also developed based on d-SPL. A silver layer pre-coated on top of another $SiO_2$ layer was patterned into interdigitated electrodes (IDEs) to form the source and drain of a FET with a channel length of 20 µm. A glycol-graphene mixture was then deposited to create the channel between the source and drain using a nanostage integrated microplotter and allowed to dry naturally. The Ion/Ioff ratio of the fabricated BGFET was calculated from the I-V curve as a $10^3$.

**Acknowledgements**

First of all, I am sincerely thankful to my supervisors Prof. Eihab Abdel-Rahman and Prof. Mustafa Yavuz for their valuable time, continuous support and true guidance throughout my education. I will always be indebted to them for giving me the opportunity to pursue a PhD, and for introducing me to the world of nonlinear dynamics, the field of energy harvesting, benchtop micro and nano fabrication method. I cannot thank them fairly enough for their encouragement, kindly assistance and constructive feedback. My sincere thanks to Assistant Prof. Caglar Elbuken for his help and teaching the field of microfluidics and rapid fabrication methods.

I would like to thank Prof. Ridha Ben Mrad, Prof. Dongqing Li, Prof. Dayan Ban and Assist. Prof. Parsin Haji Reza, for serving on my dissertation committee and their valuable feedback on my thesis.

Moreover, I would like to thank to my post doctoral colleagues Dr. Mahmoud Khater and, Dr. Sangtak Park for their endless help and useful feedback.

I am also so grateful to Dr. Majed Al-Ghamdi and Dr. M. Taylan Das, for their management and help. I feel so fortunate to have such a experienced team members in my group.

I would like to thank my colleagues/family Mohamed Arabi, Alaaeldin Elhady Ahmed, Samed Kocer, Ayman Alneamy, Omar Rasheed, Asif Abdullah Khan, Masud Rana, Benjamin Payeen, Ahmet Gulsaran, and Bersu Bastug Azer for thier collaborative works and transferring the knowledge of different fields among us as well as social activities we had together.

Furthermore, I greatly appreciate help of Micro Tool Company for their contribution of sharp micro carbide scribers with size of 5 µm tip to this study.

Last but not least, I would like to extend my deepest wholehearted thanks to my parents, Rabiye Saritas and Haci Bayram Saritas, my brother Serkan Saritas, and my wife Seyma Eyiol for their prays and support. They will always be in my heart.

## Dedication

*To my grandparents...*

*To my parents, my brother and my wife...*

# Table of Contents

# List of Figures

# List of Tables

# List of Abbreviations

| | |
|---|---|
| **AFM** | Atomic Force Microscope |
| **AC** | Alternating Current |
| **Al** | Aluminum |
| **Ag** | Silver |
| **BGFET** | Back-Gated Field Effect Transistor |
| **DOF** | Degree of Freedom |
| **DC** | Direct Current |
| **DPN** | Dip-Pen |
| **d-SPL** | Dynamic Scanning Probe Lithography |
| **EBL** | E-beam Lithography |
| **FFT** | Fast Fourier Transform |
| **FET** | Field Effect Transistors |
| **FEM** | Finite Element Method |
| **FIB** | Focused Ion Beam |
| **LOC** | Lab-on-a-Chip |
| **LDV** | Laser Doppler Vibrometer |
| **MEMS** | Microelectromechanical Systems |
| **NEMS** | Nanoelectromechanical Systems |

| | |
|---|---|
| **NGs** | Nano Grooves |
| **NIL** | Nano Imprint Lithography |
| **NTPs** | Nano Triangle Prisms |
| **o-SPL** | Oxidation Scanning Probe Lithography |
| **PDMS** | Polydimethylsiloxane |
| **PMMA** | Polymethyl methacrylate |
| **PMGI** | Polymethylglutarimide |
| **PPA** | Polyphthalaldehyde |
| **PTFE** | Polytetrafluoroethylene |
| **PCB** | Printed Circuit Boards |
| **RMS** | Root Mean Square |
| **SEM** | Scanning Electron Microscope |
| **SMU** | Source Measure Unit |
| **SPL** | Scanning Probe Lithography |
| **t-SPL** | Thermal Scanning Probe Lithography |
| **TENGs** | Triboelectric Nanogenerators |
| **2DMs** | Two Dimensional Materials |

# List of Symbols

| | |
|---|---|
| $\omega$ | Natural frequency |
| $\Omega$ | Excitation frequency |
| $z(t)$ | Displacement |
| $v(t)$ | Velocity |
| $c$ | Damping coefficient |
| $F_o$ | Static force |
| $F_s$ | Shear force |
| $F_x$ | Cutting force |
| $F_z$ | Vertical contact force |
| $F_{sn}$ | Shear normal force |
| $F_f$ | Friction force |
| $F_{fn}$ | Friction normal force |
| $\alpha$ | Rake angle |
| $\theta$ | Shear angle |
| $\beta$ | Friction angle |
| $A_s$ | Shear area |
| $\tau_s$ | Shear stress |
| $V_s$ | Scriber velocity |

| | |
|---|---|
| $r$ | Cutting ratio |
| $w$ | Chip width |
| $\theta$ | Friction angle |
| $q(t)$ | Charge |
| $t$ | Time |
| $g$ | Gravity |
| $m$ | Mass |
| $k$ | Spring Coefficient |
| $F_e$ | Electrostatic force |
| $V$ | Voltage |
| $E$ | Electrical field |
| $h$ | Thickness |
| $R$ | Resistance |
| $I$ | Current |
| $A$ | Area |
| $C$ | Capacitance |
| $\epsilon_0$ | Permittivity of air |
| $\epsilon_r$ | PDMS dielectric constant |
| $\sigma$ | Surface charge density |
| $h_s$ | Initial gap |

## List of Publications

A part of this dissertation has been previously disseminated through a provisional patent.

– ***Provisional Patent***

- Saritas, R., Al-Ghamdi, M., , Khater, M., Abdel-Rahman, E., & Yavuz, M. (2020).Dynamic Scanning Probe Lithography. *U.S Provisional Patent* No: 63/090,445

– ***Submitted Papers***

- Saritas, R., Das, T., Rasheed, O., Alhamaydeh, M., Abdel-Rahman, E., & Yavuz, M. (2021). Linear and Nonlinear Metric for Structural Health Monitoring. *Journal of Engineering Mechanics.*

- Khan, AA, Saritas, R., Rana, MM., Tanguy, N., Zhu, W., Mei, N., Kokilathasan, S., Rassel, S., Leonenko, Z., Yan, N., Abdel-Rahman, E., & Ban, D. (2021). Inorganic-organic perovskite/polymer nanocomposite enabling highly integrated uniaxial tristate hybrid nanogenerator for sustainable mechanical energy harvesting. (Accepted) *ACS Applied Materials & Interfaces.*

– ***Published Journal Papers***

- Huang, G., Khan, AA, Rana, MM., Xu, C., Xu, S., Saritas, R., ... & Ban, D. (2020). Achieving Ultrahigh Piezoelectricity in Organic – Inorganic Vacancy-Ordered Halide Double Perovskites for Mechanical Energy Harvesting. *ACS Energy Letters* , 6 (1), 16-23.

- Rana, M. M., Khan, A. A., Huang, G., Mei, N., Saritas, R., Wen, B., ... & Ban, D. (2020). Porosity Modulated High-Performance Piezoelectric Nanogenerator Based

on Organic/Inorganic Nanomaterials for Self-Powered Structural Health Monitoring. *ACS Applied Materials & Interfaces*, 12(42), 47503-47512.

- Khan, A. A., Rana, M. M., Huang, G., Mei, N., Saritas, R., Wen, B., ... & Ban, D. (2020). Maximizing piezoelectricity by self-assembled highly porous perovskite–polymer composite films to enable the internet of things. *Journal of Materials Chemistry A*, 8(27), 13619-13629.

- Kayaharman, M., Das, T., Seviora, G., Saritas, R., Abdel-Rahman, E., & Yavuz, M. (2020). Long-Term Stability of Ferroelectret Energy Harvesters. *Materials*, 13(1), 42.

- Asghari, M., Serhatlioglu, M., Saritas, R., Guler, M. T., & Elbuken, C. (2019). Tape'n roll inertial microfluidics. *Sensors and Actuators A: Physical*, 299, 111630.

– ***Conference Papers***

- Samed, K., Kamel, A., Mukhangaliyeva, L., Saritas, R., Das,T., Reza, PH., Yavuz, M., & Abdel-Rahman. (2022). Varifocal Resonant MEMS Mirrors *IEEE MEMS*

- Kamel, A., Kocer, S., Das,T., Mukhangaliyeva, L., Saritas, R., Reza, PH., Yavuz, M., & Abdel-Rahman. (2021). Demonstration of Resonant Adaptive Mirrors. *21st International Conference on Solid-State Sensors, Actuators and Microsystems*

- Al-Ghamdi, M., Saritas, R., Stewart, K., Scott, A., Khater, M., Alneamy, A., ... & Penlidis, A. (2019, June). Aqueous media electrostatic MEMS sensors. In 2019 *20th International Conference on Solid-State Sensors, Actuators and Microsystems & Eurosensors XXXIII (TRANSDUCERS & EUROSENSORS XXXIII)* (pp. 1254-1257). IEEE.

- Saritas, R., Al-Ghamdi, M., Das, T., & Abdel-Rahman, E. M. (2018, August). A Novel Method for Rapid Microfabrication. *In International Design Engineering Technical Conferences and Computers and Information in Engineering Conference* (Vol. 51791, p. V004T08A022). American Society of Mechanical Engineers.

- Das, MT, Murugan, K., Tetreault, A., Irvine, C., Rosic, A., Saritas, R., ... & Abdel-Rahman, EM (2018, August). A Triboelectric Nanogenerator (TENG) for Pipeline Monitoring. *In ASME 2018 International Design Engineering Technical Conferences and Computers and Information in Engineering Conference* . American Society of Mechanical Engineers Digital Collection.

# Chapter 1

# Introduction

This chapter is divided into four sections, the first section gives a general layout about rapid micro and nano fabrication, and scanning probe lithography methods with highlights and some of difficulties associated with. The motivations behind this research and its objectives are given in the second and third sections, and a thesis outline is discussed at the end of the chapter.

## 1.1 Motivation

Progress in nanotechnology is largely dependent on capability of fabricating nano scale structures at high resolution, consistency and high-volume [1–3]. Advancements in the fabrication of structures from nano to microscale have always been essential in the applications of micro and nanoscience [4, 5]. Thus, the fabrication has always been a critical step towards applications including micro and nano electromechanical systems (MEMS/NEMS), integrated circuits, microfluidics, micro-optics, field effect transistors (FET)

and endless others [6–9]. Using the cleanroom facility, standard lithography methods have been employed over years for fabricating these applications. Optical lithography have been used to pattern structures down to ≈ 1 µm [10], not able to pattern structures in nanoscale due to restriction in its wavelength. However, E-beam lithography (EBL) and focused ion beam (FIB) lithography can achieve patterning nano resolution that would not be possible via optical lithography [11, 12]. However, fabrication in cleanroom facility brings out its own difficulties since it requires multiple complex processes, it is also hard to access and expensive method to be deployed.

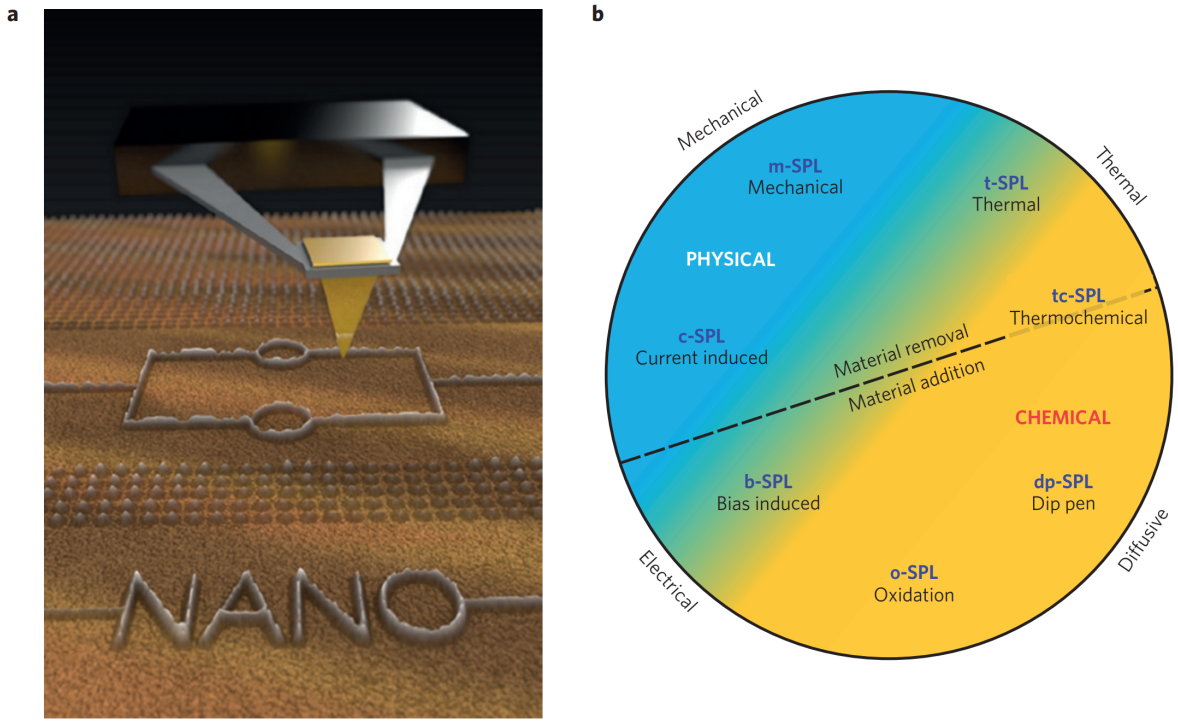


Figure 1.1: (a) A schematic of scanning probe lithography (SPL). (b) Classification of SPL methods according to tip–surface interaction used for patterning, called electrical, thermal, mechanical and diffusive processes. Reproduced with permission [3]. Copyrights 2014. Nature.

Development of novel and low-cost fabrication techniques allows more applications and elevates the progress in academic research as well as industry [13, 14]. Thereby, alternative fabrication methods were developed such as rapid prototyping and scanning probe lithography (SPL) methods that do not seek use of cleanroom facility. Rapid fabrication methods include $CO_2$ laser cutting, inject printing, femtosecond laser method and etc. These are alternative rapid fabrication methods but $CO_2$ laser cutting and inject printing offers limitations in terms of the resolution they can achieve compared to standard lithography, and femtosecond laser has still lack of high cost although it has competitive resolution with respect to optical lithography. These limitations in rapid prototyping motivated exploration of alternative fabrication methods. SPL methods have been proposed to elevate the limitations. They can be classified into two main categories: material removal and addition. They are named according to tip-surface interaction such as thermal, mechanical, current induced, thermomechancial, dip pen, oxidation and bias induced as illustrated in Figure1.1. Over the past few years there has been a number of research papers that demonstrated the efficacy of d-SPL methods to overcome some of difficulties and limitations in the fabrication. On the other hand, each of these SPL methods has still its own limitations such as small area patterning, indirect surface patterning for particularly thermal type SPL, and requiring closed-loop feedback mechanisms for mechanical SPL particularly using AFM setup.

## 1.2 Scope

An ideal fabrication approach shapes various materials such as organics, nano wires, semiconductors and two-dimensional materials (2DMs) deployed in bio and chemical applications [15–18]. In addition, the ideal method should also be rapid, cost-effective and easily

accessible. The EBL and FIB lithography methods have been broadly implemented for fabricating micro and nano devices [19–22]. However, these methods are limited to small area patterning, long operation time, requirement for high vacuum and inability to directly pattern a wide range of materials [23–26]. As mentioned early, these limitations have motivated the exploration of unconventional lithography methods [27].

Many researchers have proposed different approaches by exploiting the surface-tip interactions phenomena. Scanning probe lithography has been developed to lower the cost and alleviate the need for high vacuum [28–30]. It has attracted tremendous attention and gave birth to several variations of the original techniques [31–34]. Their capabilities have enabled the fabrication of the smallest field effect transistors and direct patterning of novel materials, which was otherwise not possible to fabricate using conventional lithographic methods [35]. Although SPL reduced the complexity and cost of fabrication in comparison with EBL and FIB, high throughput and low-cost patterning of large areas has remained an unaddressed issue [36–39]. These limitations been a great deal of research to resolve.

In this research, dynamic Scanning Probe Lithography (d-SPL) is introduced with its own unique features: (i) micron to nano scale thickness resolution, (ii) centimeter size uniform patterning in seconds, (iii) applicability to a wide range of materials, (iv) high throughput and elevating the need for vacuum. This method owes its distinctive abilities to a spring-damper suspension connected to a sharp scriber tip mounted on a programmable 3D nanostage. The suspension mechanism enables the scriber to move up and down, thereby creating an adaptive working distance without a need of complicated feedback systems. The suspension mechanism compensates variations in surface contact force, thus produces long and uniform surface patterns. An optical camera equipped with an 6× objective lens and 2× optical magnifier is attached to the stage to monitor the patterning process. We were able to pattern a 1 cm-long, 2.5 µm-wide,600 nm deep channel in less

than 10 seconds, which is a few magnitude of orders faster than conventional scanning probe lithography methods. Moreover, d-SPL method allows fabrication of micro and nanowires through continuous chip removal process. Lastly, d-SPL is deployed to directly pattern nano thin films to fabricate back-gated field effect transistors (BGFETs).

## 1.3 Research Objectives

In this dissertation, we explain the d-SPL method and its implementation for creating micro and nanochannels, producing micro and nano wires as well as fabrication of filed effect transistors. The main objectives of this research can be summarized as follows:

- Explanation of fundamental working principle of the d-SPL method.
- Implementation of d-SPL for micro and nanochannel fabrication as an application.
- Deploying d-SPL for surface modification of triboelectric films to increase the effective surface area thereby enhancing the output power of triboelectric energy harvesters.
- Fabrication of long and uniform micro and nano wires that are flexible and conductive.
- Demonstration of d-SPL for fabrication of micro and nano scale circuits and direct patterning of nano thin metal films to be used in field effect transistors.
- Use of a microplotter to create a graphene channel between source and drain.

  **Fundamental contributions:**

- Developed an analytical model describing the working mechanism of d-SPL and to simulate the model to investigate its safe operation conditions and limitations.

- Developed a coupled electromechanical model to investigate electromechanical behavior of TENG and to design wide and low-frequency range triboelectric energy harvesters.

## 1.4 Organization of the Dissertation

This research is organized in seven chapters.

- **Chapter 1** discusses a general overview of fabrication methods, the research motivation and main objectives.
- **Chapter 2** gives detailed literature review of rapid fabrication and SPL methods with their applications, limitations and advantages.
- **Chapter 3** discusses the fundamental working principle of the d-SPL, and demonstrates the potential of d-SPL for fabrication of micro and nano channels, as well as micro and nano wires. It also explains fundamental working principle and analytical model developed for the d-SPL.
- **Chapter 4** demonstrates implementation of the d-SPL in triboelectric energy harvesters and also explains a coupled electromechanical analytical model developed for triboelectric energy harvesters to design wide and low-frequency range of TENGs.
- **Chapter 5** demonstrates use of d-SPL method for direct patterning of nano thin metal films for fabrication of nano scale circuits and back-gated graphene field effect transistors.
- **Chapter 6** presents a summary of the most important findings of dissertation and future work.

## 1.5 Contributions

Contribution of collaborators has made this work possible and it is greatly appreciated and acknowledged by the author of this thesis.

- Dr. Mahmoud Khater has been of great help for developing the analytical models in this dissertation.
- Benjamin Payeen and Omar Rasheed have specifically helped in development of nanostage for control algorithm, design and G code execution.
- Dr. Majed Al-Ghamdi and Taylan Das have helped for surface patterning and triboelectric energy harvester experiments.

# Chapter 2

# Background

This chapter presents a detailed review of rapid and low-cost micro fabrication methods and conventional scanning probe lithography methods developed over the years. Examples of applications where they have been used are also presented. The chapter concludes with discussion of the current state of the art and difficulties encountered with micro and nano fabrication.

## 2.1 Rapid Fabrication Methods

Scaling down of device fabrication to nanoscale has always been critically essential to advancement of micro and nanoscience [40]. Cleanroom facilities provide a variety of equipment to enable fabrication of these devices with high resolution. In the cleanroom, micro and nano patterning are the main foci of the fabrication. Optical lithography with ultraviolet light is mainly used for patterning of features larger than 1 µm. This limitation is imposed by the wavelength of the light which precludes the possibility of fabricating

structures at nano scale using the optical lithography. Other lithography methods such as electron-beam [41] and focused ion beam lithography [42] have been introduced to pattern nanostructures. They can pattern structures with high resolution however, they are costly, hard to access and require vacuum technology.

Scientists have attempted to develop less expensive lithography methods, such as soft lithography [43], dip-pen lithography [44, 45], and nano imprint lithography (NIL) [46]. However, all of these fabrication methods still require expensive and time consuming clean-room facilities. On the other hand, rapid prototyping methods have been developed to reduce fabrication cost and time and to eliminate the need for clean room facilities. Some of these methods include micro-milling [47], $CO_2$ laser engraving [48], femtosecond laser engraving[49], and 3D printing [50, 51]. However, the resolution of the laser engraving, printing, and milling technologies are no better than 50 µm [52–54]. This forces devices requiring features smaller than 50 µm back to the cleanroom facility. While femtosecond laser engraving provides much better resolution than those rapid fabrication methods, but it is still an expensive tool.

### 2.1.1 Micro-milling

CNC based micro-milling machine has been recently applied to fabricate microchannels on the surface of Poly(methyl methacrylate) (PMMA) material. Micro-milling tool removes material on surface of PMMA substrate based on predefined trajectory with controllable velocity. David et al [47] demonstrated a CNC micromilling system for ultra-rapid fabrication of microchannels, figure 2.1. The desired pattern is designed in a CAD software, such as SolidWorks, exported as a machine readable Gerber file, and sent to CNC software to process the microchannel fabrication on PMMA. This technique is low-cost effective

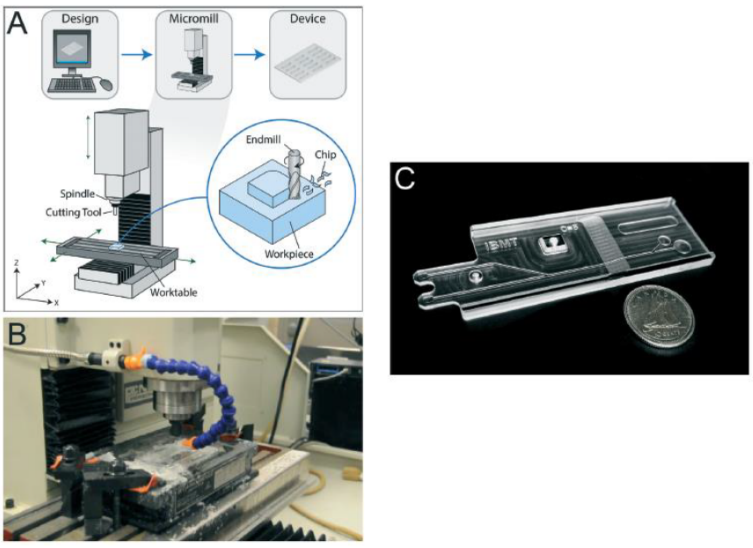


Figure 2.1: (A) A schematic of a CNC micro milling process. It consists of a worktable to provide planar motion, a cutting tool to remove material from the workpiece, and a spindle to spin the cutting tool and to provide vertical motion. (B) A picture of a CNC micro-mill during operation. (C) An image of a micro-milled thermoplastic device. Reproduced with permission [47]. Copyrights 2015. Royal Society of Chemistry.

and ultra-rapid. It does not require any clean room processes [47]. The channel depth and width can be controlled. However, this technique has limitations on channel width imposed by diameter of the cutting tool and its mechanical vibrations. Therefore, it does not allow for further scaling down of microchannel fabrication. Further, surfaces of the patterned channels are not smooth.

### 2.1.2 $CO_2$ laser engraving

Direct $CO_2$ laser cutting (ablation) has been used to fabricate patterns on variety of polymeric substrates such as PMMA. Many research laboratories are using it for microchannel fabrication due to its convenience and rapid processing [48, 55]. A design of interest is drawn in a 2D CAD software, such as AutoCad, exported as Gerber file, and sent to $CO_2$ laser engraving device. The laser beam ablates and grooves the PMMA according to the design [53]. PMMA surface is cleaned using DI water and air compression to remove the PMMA ablates.

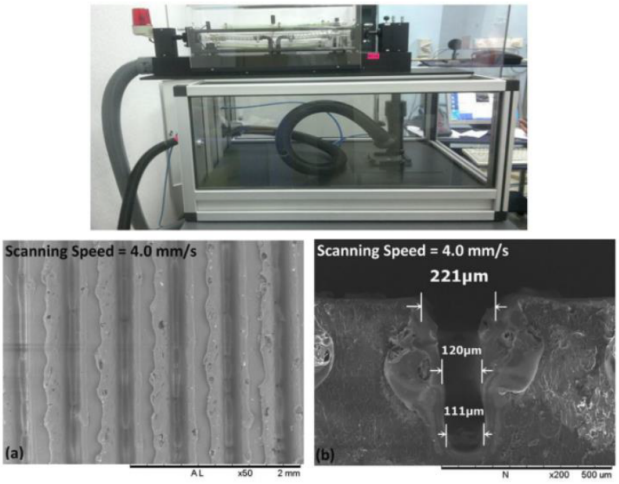


Figure 2.2: Direct $CO_2$ laser cutting setup and SEM images of fabricated microchannels.Reproduced with permission [56]. Copyrights 2016. IOP.

This technique is very rapid, user friendly, and low-cost method. It can fabricate long microchannels on order of centimeters. However, it is restricted to fabrication of microchannels less than 50 µm wide [53]. Laser ablation also occurs on the edges of the channel, and cross sectional area of the channels has the shape of trapezoid. Figure 2.2

shows experimental setup for the $CO_2$ laser cutting the cross section of the channels and laser ablation produced by this method [56].

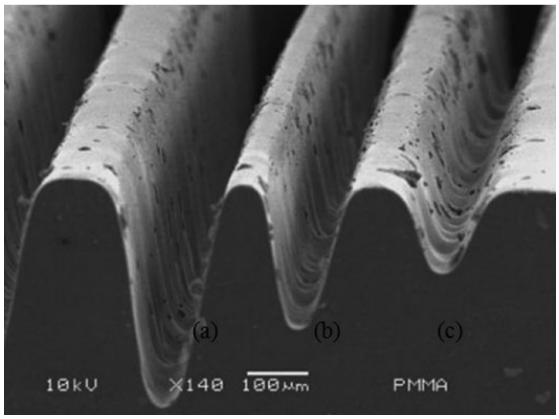


Figure 2.3: SEM image of PMMA substrate with channels of different depths produced by unfocused laser beam (k = 20 mm) with constant laser power of 4 W and scanning speeds of (a) 80 mm/s, (b) 120 mm/s and (c) 150 mm/s, respectively. Reproduced with permission [57]. Copyrights 2010. Springer.

Hong et al. [57] showed that microchannel dimensions can be controlled by adjusting scanning speeds. Lower scanning speeds result in deeper microchannels as shown in figure 2.3 due to a higher number of delivered laser pulses per unit area compared to microchannels fabricated at higher speed.

### 2.1.3 Femtosecond laser engraving

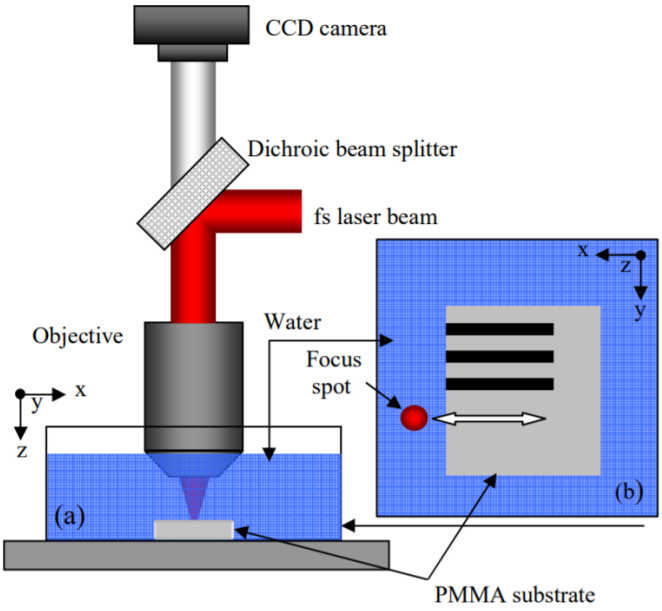


Figure 2.4: Schematic diagram of (a) the experimental setup for fabrication of microchannels and (b) the geometry of that fabricated sample. Reproduced with permission [49]. Copyrights 2016. SPIE.

Day et al. [49] employed a femtosecond laser to fabricate microchannel on the surface of the PMMA immersed in water by applying high repetition nano-joule laser pulses to produce microchannels ranging from 8 to 20 µm in width. A femtosecond pulsed laser generating 80 fs pulses at a repetition rate of 80 MHz was deployed in the experiment. The samples were immersed in water in order to decrease wavefront aberrations, figure 2.4. The water immersion system also assisted the fabrication process by clearing the debris on the edges and inside the channels. After the laser engraving, sample was placed on hot plate for annealing because the laser irradiated area has different density than bulk material [49].

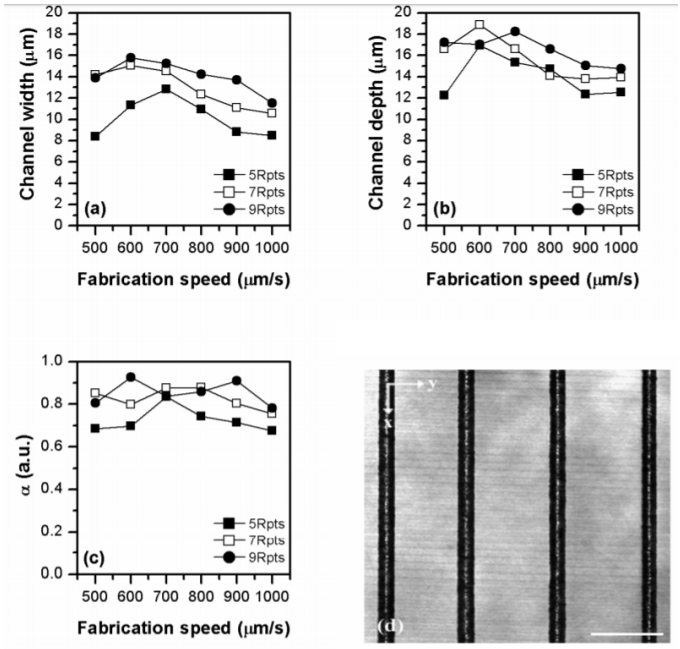


Figure 2.5: Measured microchannel (a) width, (b) depth and (c) ratio of width to depth as functions of the laser traversing speed. (d) Image of microchannels. Scale bar = 50 μm. Reproduced with permission [49]. Copyrights 2016. SPIE.

Figure 2.5 demonstrates effects of laser traversing speed on the dimensions of the microchannels. As the speed of the laser increases, width and depth of the channel decreases from 16 μm to 8 μm and from 18 μm to 12 μm, respectively [49]. This is a non-lithographic and rapid fabrication technique. However, femtosecond laser is expensive, and the achievable microchannel width and depth are limited. Further, channels less than 8 μm wide cannot be fabricated using this technique due to resolution of the laser beam. Finally fabrication of microchannels wider than 10 μm is time consuming for due to need for a slow traversing speed.

### 2.1.4 3D printing

3D printing has been used in variety of applications including fabrication of conductive patterns for printed circuit boards (PCB) [50], scaffolds for human organs, such as kidney and ear [58], and microchannels [59, 60]. Figure 2.6 shows the fabrication flow process of a spiral microchannel using 3D printing method. First, a metal liquid is printed on a substrate then mixture of PDMS base and its curing is poured onto it. Then, HCl solution is driven to flush the metal pattern and empty the channel. Later, the channel is refilled with red dye to demonstrate the pattern [59]. This is a simple and low-cost micro fabrication method. However, it is incapable of creating microchannels less than 100 µm wide.

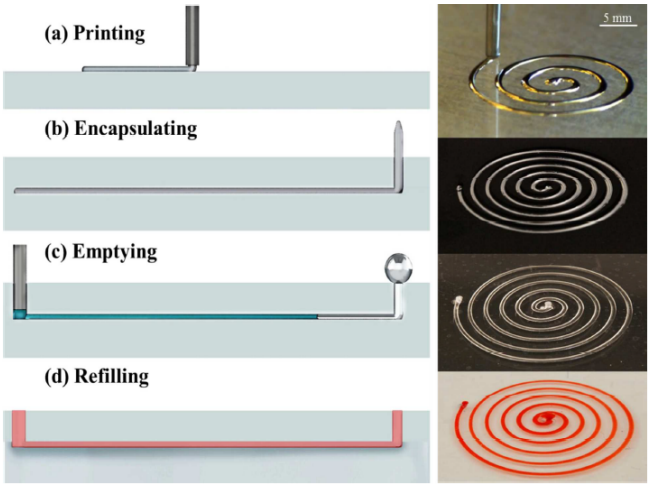


Figure 2.6: Images depicting 3D printing steps. (a) Printing of a liquid metal onto a substrate. (b) Encapsulating the printed pattern in a PDMS. (c) Emptying the metal from the encapsulated channels. (d) Refilling the empty channels with red dye. Reproduced with permission [60]. Copyrights 2016. Royal Society of Chemistry.

## 2.2 Scanning Probe Lithography Methods

### 2.2.1 AFM lithography

Atomic force microscope (AFM) has been used in variety of applications including investigation of surface topography, 3D-imagining, and fabrication of micro and nanochannels [61]. Arda et al. [62] used an AFM tip for micro and nanochannel fabrication. Surface calibration process was first carried out then, sample was placed perpendicular to the tip. Data acquisition system supplied signals to piezoelectric actuator through voltage amplifier [62]. Figure 2.7 shows experimental setup for the fabrication of microchannel using AFM tip.

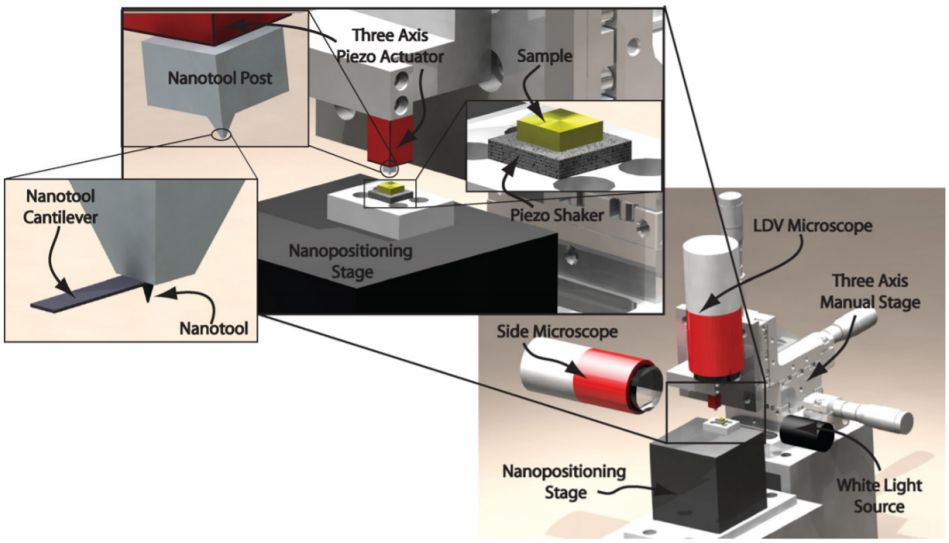


Figure 2.7: An AFM measurement of three channels created on a PMMA surface using the out-of-plane configuration of the nanomilling process. The horizontal axis of the bottom figure is compressed to show all three channels. Reproduced with permission [62]. Copyrights 2012. Elsevier.

AFM lithography offers fabrication of very small features produced from nano to microscale. It initially begins to create nanofeatures and can reach to microscale by multiple processes. But, length of the patterning remains in a few tens of micrometers [26, 63], since AFM tip can be damaged during the patterning due to non-uniform gap between the tip and surface over long distance. Therefore, it disables to pattern long micro or nanofeatures and fabrication of its some applications. For example, fabrication of a simple electrode using AFM method requires considerable time and cost, and more importantly it will be in small micro scale, which is difficult to probe unless use of a probe station. In mechanical scanning probe lithography, plastic deformation always appears on the walls of the channels created, the deformation part can be removed later by mechanical and chemical polishing method [64].

Nano-positioning stage in Z axis was adjusted to obtain desired depth and trace of the channels. Advantages of this technique are considered as: circular or straight microchannel can be fabricated and cost effective comparing to use of nano-lithography devices such as FIB or EBL, and lastly depth of the micro channel can be reduced down to a few hundred nanometers. In contrast, the limitations of this technique are: patterning of the microchannels is on the order of tens of µm, thus not very suitable for large scale microchannel fabrications, and it is very time consuming process and requires surface calibration [62]. Also, the method can pattern materials softer the scriber material. Mechanical wear on the scriber surface might be observed and depending on how relatively scriber material is harder than workpiece.

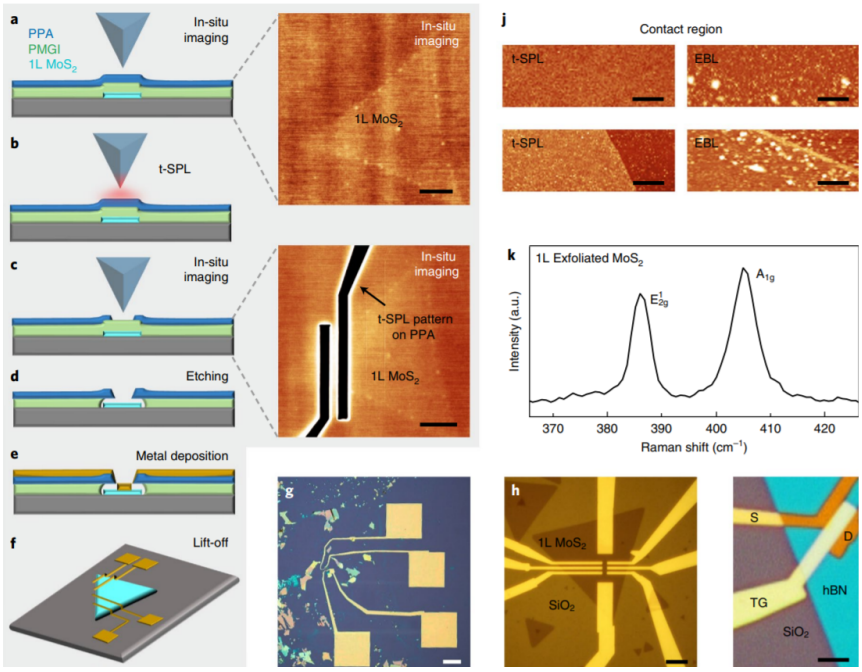


Figure 2.8: Process flow for t-SPL fabrication of a $MoS_2$ transistor and in-situ thermal nano-imaging of the sample topography. Scale bar = 4 µm. Reproduced with permission [65]. Copyrights 2019. Nature.

### 2.2.2 Thermal SPL

Thermal Scanning Probe Lithography (t-SPL) utilizes a tip with a diameter in the range of nanometers to remove the material from a substrate via localized heat. The heat in the tip is generated through an electrical resistance (joule heating).

Figure 2.8 shows the process flow and surface topography of a $MoS_2$ transistor fabricated via t-SPL. The substrate is initially coated with three layers. t-SPL removes the top Polyphthalaldehyde (PPA) layer, figure 2.8 (c), then a polymethylglutarimide (PMGI) layer is etched to deposit the metal contact onto the $MoS_2$ to produce the source and drain of the transistor. This method can pattern nano structures with very high resolution

and provide in-situ nano-imaging of the sample topography without requirement vacuum technology. On other hand, it is a slow process (on the order of 0.1–50 µm/s) and requires indirect surface patterning of specific layers [32]. It is not very applicable to bulk production purposes.

### 2.2.3 Thermochemical SPL

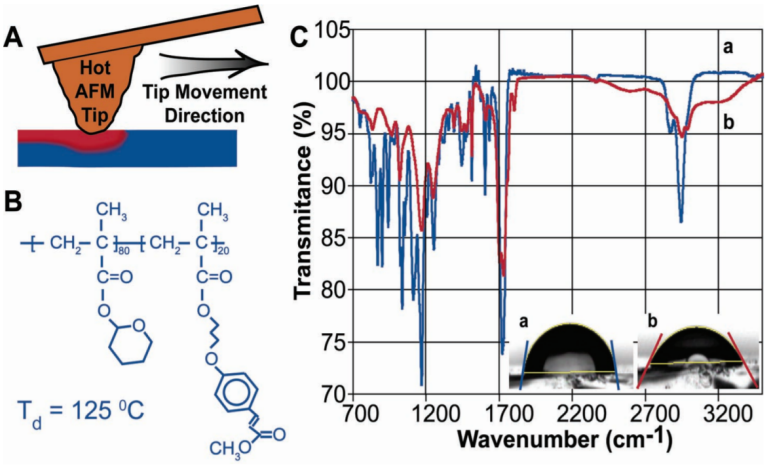


Figure 2.9: Experimental setup demonstrating a resistively heated silicon AFM tip scanning across a copolymer p(THP-MA)$_{80}$ p(PMC-MA)$_{20}$ sample. The heated tip initiates thermal reactions in the polymer film above a certain temperature. Reproduced with permission [66]. Copyrights 2007. ACS.

This nanolithography method employs a resistively heated AFM tip like thermal-SPL. In addition, a chuck heats the substrate heat is deployed to locally change the chemistry of a material rather than mechanical removal process [66, 67]. Figure 2.9 shows the working procedure for the thermochemical SPL.

The heated AFM cantilever was used (2.9 A) to create chemical reactions in surface

functionality of thin polymer films with well defined the trajectory [66]. The distance between tip and surface can be adjusted. It is not necessary to have the tip indenting the surface for this process [66, 67]. Figure 2.10 demonstrates chemically produced patterns in size of 3 µm × 3 µm [66].

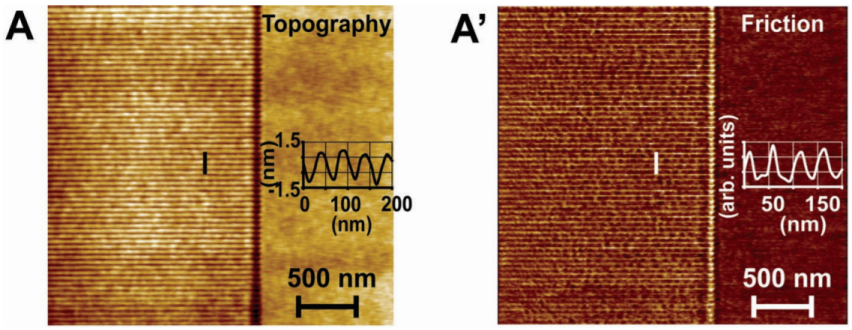


Figure 2.10: (A) 3 µm × 3 µm AFM topography image and (A') corresponding friction image of a cross-linked p(THP-MA)$_{80}$ p(PMC-MA)$_{20}$ film showing a high-density line pattern written chemically on the left side. Reproduced with permission [66]. Copyrights 2007. ACS.

This method has very high resolution in the range of nanometers and does not seek the vacuum technology. On the other hand, challenges of this method are: speed of this technique is limited to velocity scan of the AFM, requiring a feedback control system, and only applicable to specific materials for the functionalization.

### 2.2.4 Dip-pen SPL

In Dip-pen SPL, molecular inks are loaded to a sharp AFM tip, which is subsequently inserted into a scanning probe microscope [68]. The vertical contact between the tip and the scanning probe is controlled by the scanning probe configuration. The ink-loaded tip

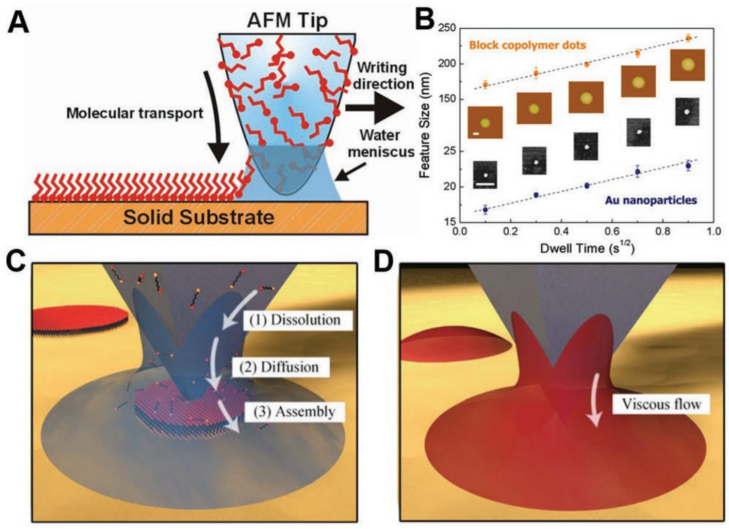


Figure 2.11: Mechanism and ink transport in DPN. A) Schematic representation of DPN. B) Time-dependent feature size increase in DPN with copolymer ink as an example. C) and D) Schematic diagrams of the ink transport processes for diffusive molecular inks and liquid materials, respectively. 'A' Reproduced with permission [68]. Copyrights 1999. AAAS. 'ABCD' Reproduced with permission [69]. Copyrights 2019. Wiley.

dispenses materials onto the substrate through a water meniscus that bridges the tip with the substrate surface as shown in the figure 2.11.

3D portrait fabrication of Monalisa, figure 2.12, was demonstrated using the dip-pen SPL via Zhou et al. [70]. Advantages of this method are: direct material addition, not requiring the vacuum technology, and also providing high resolution. However, main limitations are: small scale fabrication (in other words, it is a slow fabrication process), and requiring a feedback mechanism for finding the surface of the substrate.

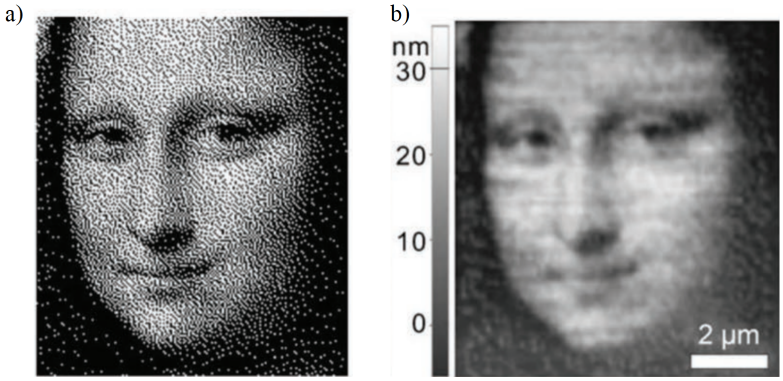


Figure 2.12: (a) Bitmap image of Monalisa and (b) corresponding AFM topographical image of Dip-pen Nanolithography-patterned Monalisa. Reproduced with permission [70]. Copyrights 2011. Wiley.

### 2.2.5 Oxidation SPL

Oxidation scanning probe lithography (o-SPL) is a method that enables the direct modification of small areas with a specific functionality. Silicon, gallium arsenide compounds, tantalum and titanium surfaces were the first materials modified by o-SPL [71]. Water bridge between the tip and the sample is the main point in o-SPL. This water meniscus is formed by gas phase and water molecules on substrate. Water bridge supplies $OH^-$ molecules to create oxidation on the surface of the substrate [71–73]. According to molecular dynamic simulations, formation of the water bridge must have a threshold value which was also experimentally demonstrated [74, 75].

A voltage is applied between sample and the tip. This voltage contributes the oxidation via initiating hydrolysis that produces the $OH^-$ molecules, and electrical field drives these molecules to substrate [71]. Figure 2.13 shows the general scheme of the o-SPL. This method provides high resolution, direct surface modification, and does not seek for vacuum. However, it requires a feedback mechanism and a voltage bias, slow surface modification

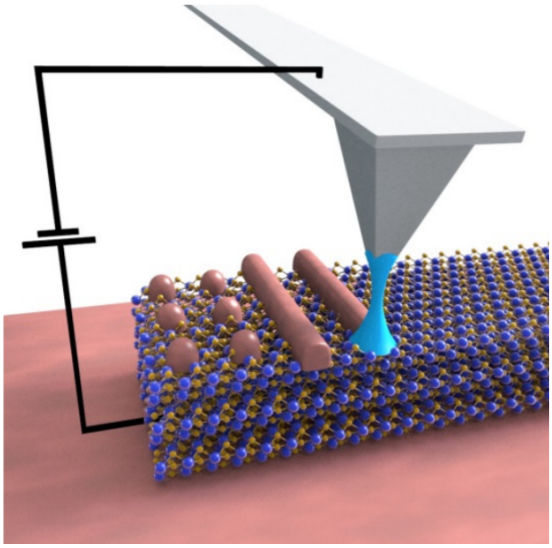

Figure 2.13: General scheme of nanopatterning in o-SPL. Reproduced with permission [73]. Copyrights 2017. IOP.

process, and not applicable to bulk production.

## 2.3 Summary

In summary, different forms of fabrication techniques including rapid and conventional scanning probe lithography methods were reviewed. We discussed and highlighted their advantages and disadvantages as well as their applications. We also presented their different applications such as fabrication of micro and nano channels, and transistors.

It is not always possible to have cleanroom facility or equipment for fabrication of micro and nano features. This has motivated scientists focus on for rapid and low-cost micro and nano fabrication techniques. Many rapid fabrication techniques have been developed using polymer based materials and applied to Lab-on-a-Chip (LOC) systems. Rapid fabrication

methods provides help with cost, time and mass production. But, they most commonly suffer from the perspective of their resolution. There is a still gap for fabrication of features less than 50 µm. Fabricating micro features less than 50 µm still requires using standard lithography process which is hard to access and expensive as mentioned earlier.

On the other hand, scanning probe lithography methods have been developed to allow high resolution, and to alleviate a need of vacuum for the fabrication. However, they are slow processes, require a complex close-loop feedback mechanism since they are employing the AFM stage, and lastly not suitable for the mass production. They are today used in academia and has slow writing speed in the range of 0.1–50 µm/s.

In the next chapter, we introduce a new benchtop, low-cost, and rapid lithography method, namely dynamic scanning probe lithography (d-SPL). The d-SPL's analytical model as well as its experimental and numerical results will be also presented and discussed.

# Chapter 3

# Dynamic Scanning Probe Lithography

In this chapter, we describe the working principle of d-SPL method and demonstrate a benchtop rapid fabrication of micro and nano wires through continuous chip removal process, and micro and nanochannels. A mathematical model of the d-SPL is also developed. Small micro scale chattering was observed in the patterning, for the first time, and then verified and validated through experiments.

## 3.1 Working Principle

The d-SPL method allows fabrication of uniform surface patterning. It only employs a sharp-tip scriber attached to an automated 3D nanostage through a suspension mechanism. The XY (planar) component of the stage carries the work-piece (substrate) as shown in figure 3.1.

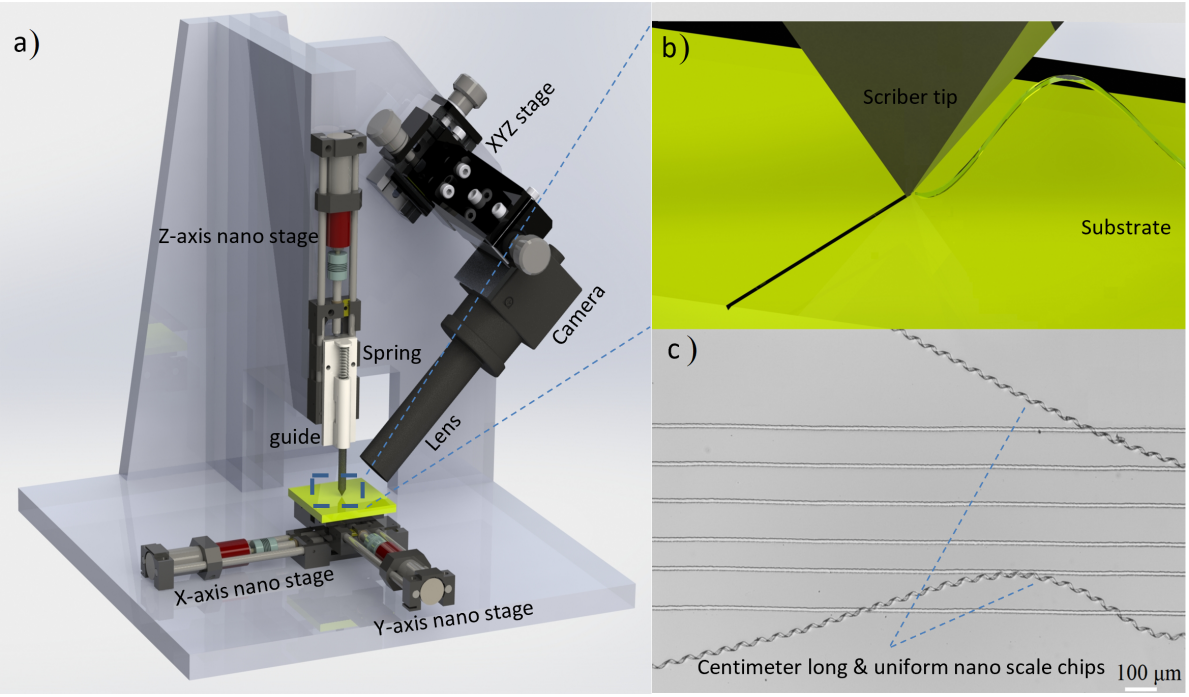


Figure 3.1: Overview of compact dynamic scanning probe lithography setup. (a) A schematic of custom built 3D nano stage with spring-damper assisted suspension mechanism, and a optical camera. (b) Close-up view of the sharp scriber tip and chip removal process. (c) Optical microscope image of multiple uniform, 1 cm long patterns and the removed nano scale chips.

The scriber is attached to the Z-component of the stage through the suspension mechanism. While other arrangements of the system are possible, such as Z-axis nanostage can be integrated with X-Y nanostage. This could introduce cross-talk between the stages therefore producing more mechanical noise in the system. Specifically, decoupling the Z-stage from the XY-stages reduces cross-talk between them. Coupling the X and Y stages into one platform (component) is advantageous to create complex surface features efficiently, thus this arrangement is preferred.

It is cumbersome to maintain perpendicular alignment between the substrate and the tip. It is also cumbersome to align the substrate surface with the planar stage. Moreover, the substrate surface is, in general, not perfectly planar. Since, perfect alignment between tip and substrate is hard to achieve, the suspension mechanism is designed to counteract misalignment. When a rigid scriber encounters changes in the substrate surface height or alignment, it will damage the surface, corrupt the feature, or permanently deform and fail its tip. When the tip is brought to contact substrate, the spring is compressed by a given displacement. This compression in suspension mechanism is designed to alleviate these problems by allowing the scriber tip to move up or down with respect to the substrate surface while regulating (minimizing variation in) the tip-surface contact force, thereby creating a flexible working distance. As a result, the d-SPL can handle both atomically flat as well as rough surfaces as long as the roughness is within the working distance. Passive energy loss mechanisms are embedded in the suspension system to help regulate the tip-surface contact force by absorbing external disturbances as well as residual vibrations due to micro-impacts between the tip and surface asperities. The combined mechanism endows d-SPL with unique capabilities to create uniform centimeter-long surface patterns, such as the microchannels shown in figure 3.2.

Specifically, d-SPL can be used to create positive as well as negative surface features on flexible and rigid substrates as detailed below.

1) Negative patterning: This fabrication process works directly with bare substrate surfaces or thin films deposited or sputtered on top of a substrate. The features of interest are patterned into the surface, such as micro and nanochannels, up to a depth of 1µm and lengths on the order of centimeters. The features created in the surface can also be used as a negative mold to cast polymers, such as PDMS, with similar positive surface feature. The process parameters in this case are:

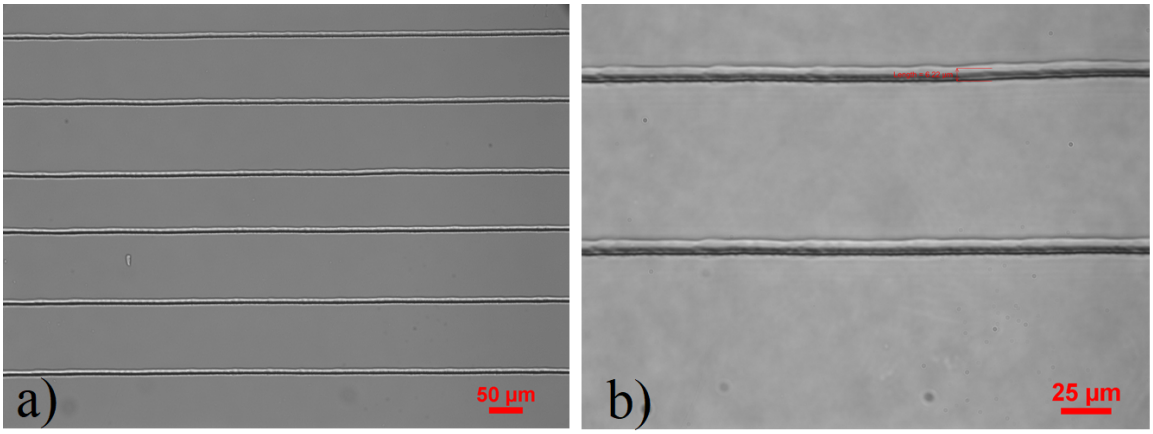


Figure 3.2: (a) Optical images of fabricated micro-channels (b) close view of the channels.

- The scriber-substrate contact force which is calibrated to obtain the desired feature width and depth.
- The scriber material hardness which is selected higher than the substrate hardness to ensure chip removal with minimal tip wear and deformation.

2) Positive patterning: First, a thin metallic or polymeric layer, 1µm or less, is deposited on the substrate by spin coating, sputtering, or chemical deposition. The deposition process parameters are calibrated to reduce adhesion between the layer and the substrate. Patterning is carried out by removing excess surface layer material and leaving only the desired design on the substrate surface. Post-processing includes chip cleanup using compressed air or deionized water washing. It may also include sintering of metallic layers or baking of polymeric layers.

   The process parameters in this case are:

   - The scriber-substrate contact force which is calibrated to guarantee full removal of the surface layer without scouring the substrate.
   - The tip cross-sectional area is selected to achieve the desired pattern resolution.

- The scriber material and tip cross-sectional area are selected to overcome chip removal and friction forces.
- The substrate material hardness is selected higher than that of the scriber top layer to avoid scouring the surface.

## 3.2 Analytical Model

### 3.2.1 Static analysis

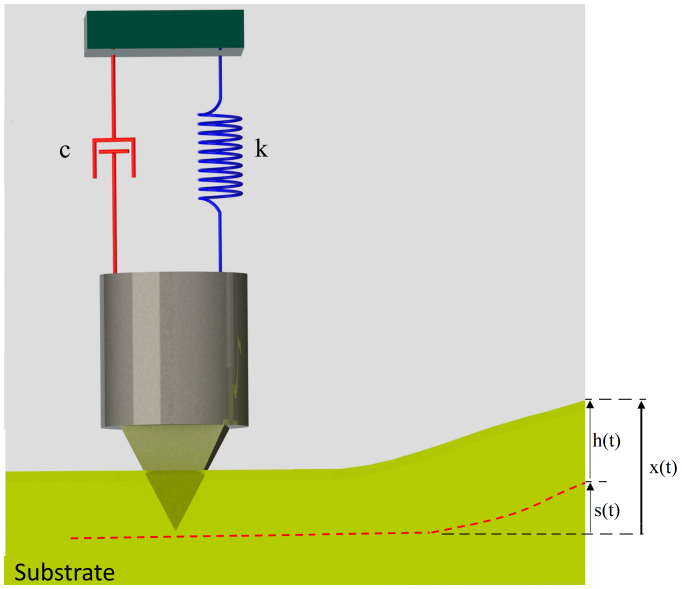


Figure 3.3: Schematic of d-SPL.

After the first contact of the scriber to the substrate, an actuator commands a displacement of along the vertical direction until the scriber penetrates the substrate surface by a initial penetration distance $h_\circ$. It then commands the scriber to follow a predefined trajectory along the substrate surface to create the desired pattern around static equilibrium.

To minimize variations in the vertical contact force due to variations in surface height and properties, the scriber suspension mechanism is provided with a spring such that initial spring compression $l$ is much larger than variations in penetration depth $h_\circ$. A schematic of the d-SPL is shown in figure 3.3.

where $x(t)$ is variation in surface height of the substrate and $h(t)$ is the instantaneous penetration depth.

At static equilibrium the vertical contact force can be written as:

$$F_\circ = kl \tag{3.1}$$

where $k$ is the linear spring stiffness.

The change in the vertical substrate contact force is calculated as:

$$\Delta F = kz \tag{3.2}$$

As can be seen from the Eq. (3.2), $\Delta F$ is dependent on the $k$ and $z$ relative displacement of the scriber with respect to $h_\circ$ the substrate. This change becomes very significant when a spring with larger stiffness is implemented in suspension mechanism for surface patterning. Deploying very large spring stiffness coefficient leads diminishing flexibility of the spring and causes an extensive increase in $\Delta F$, thereby losing the stability of uniformly patterning or causing failure in scriber. However, using a low spring stiffness coefficient enables high flexibility in tip movement and negligible change $\Delta F$ in surface contact force. Considering very low spring stiffness coefficient yields;

$$F_\circ >> \Delta F \tag{3.3}$$

$$l >> z \tag{3.4}$$

Variation in substrate contact force along the centimeter long surface patterning is relatively much smaller than initial surface contact force, thereby including spring suspension mechanism allows uniform surface patterning with negligible variation in the pattern.

### 3.2.2 Dynamic analysis

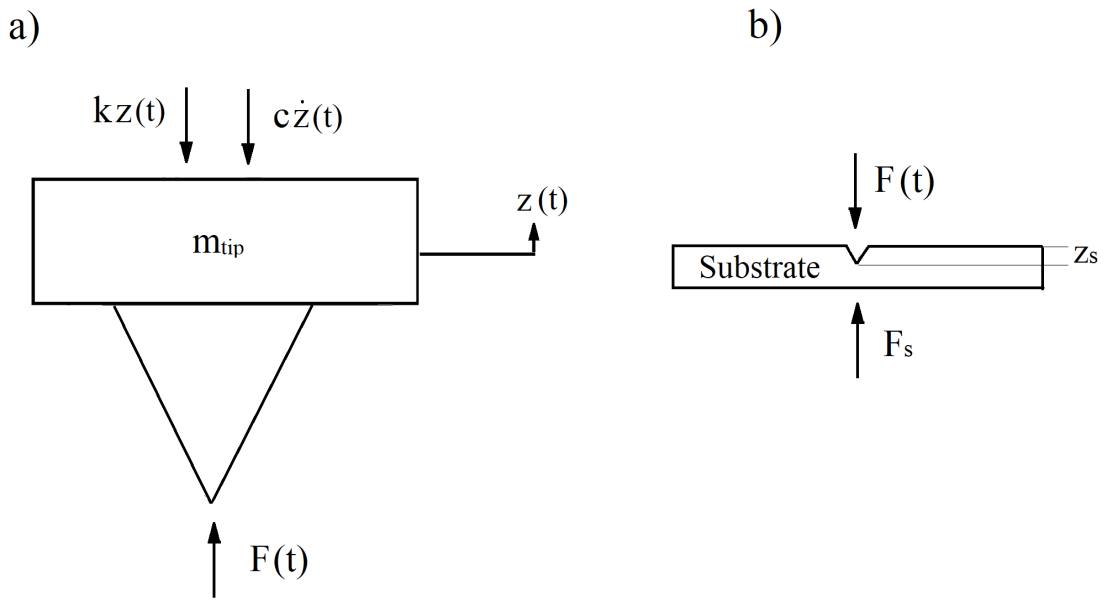


Figure 3.4: Free body diagrams of (a) the scriber and (b) the substrate.

The vertical working distance of the scriber is determined by the stiffness $k$ of the spring. As the stiffness decreases the working distance increases and vice versa. Forces acting on the scriber 3.4(a) and substrate 3.4(b) is demonstrated. Assuming a rigid scriber and a linear spring force-displacement relationship, the scriber's equation of the motion can be written as:

$$m\ddot{z} + c\dot{z} + kz = F(t) \tag{3.5}$$

where $z$ is the relative displacement of the scriber with respect to $h_\circ$ the substrate, $m$ is the scriber mass, and $c$ is a linear damping coefficient representing energy loss mechanisms arising from the interactions of the scriber with its holder, the chip, and the substrate.

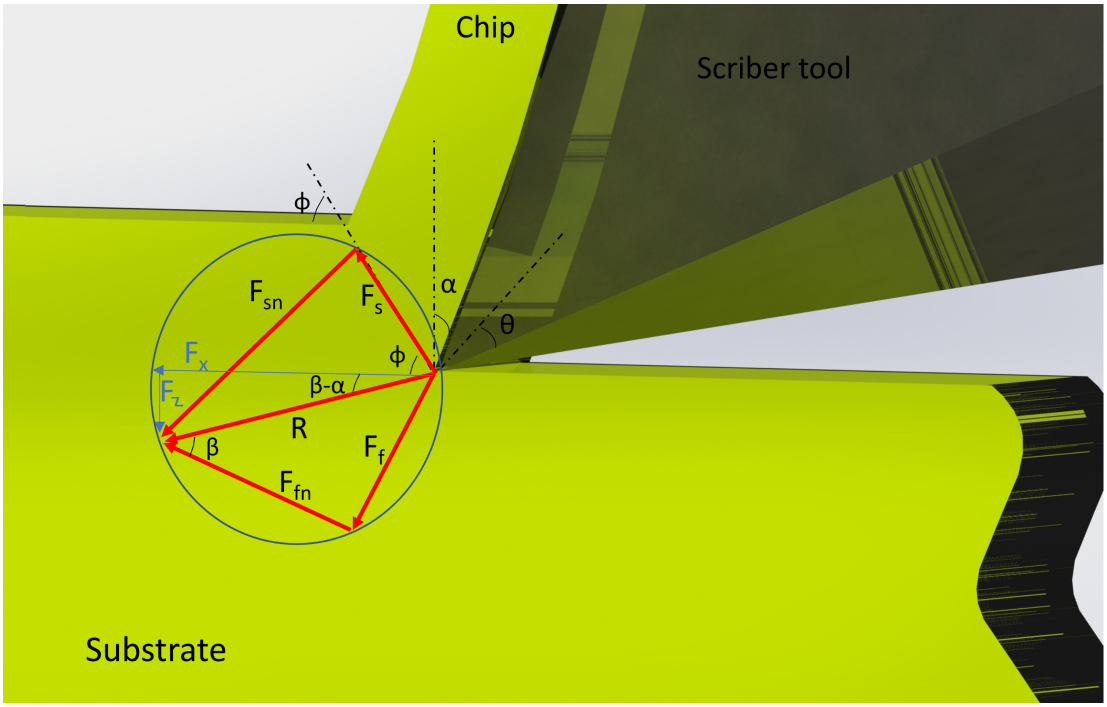


Figure 3.5: Free-body diagram of the cutting process.

The Merchant circle [76] provides a two-dimensional, schematic of forces involved in the cutting process as shown in figure 3.5. The scriber applies a cutting force $F_x$ to remove the chip while applying a normal force $F_z$ on the surface. The resultant force is $R$. Other forces appearing during the cutting process are the shear force acting on the chip $F_s$ and the friction force $F_f$ opposing chip flow over the rake surface. The normal forces necessary to balance the former forces with resultant force are called the shear normal $F_{sn}$ and friction normal $F_{fn}$ forces, respectively. The angles $\alpha$ and $\phi$ are the rake and shear angles, respectively.

The vertical component of the contact force $R$ is given by

$$F_z = \frac{F_s \sin(\beta - \alpha)}{\cos(\phi + \beta - \alpha)} \tag{3.6}$$

where $\beta$ is the scriber friction angle.

$$\tan \beta = \frac{F_f}{F_n}$$

The shear force $F_s$ is equal to the product of the shear stress $\tau_s$ and shear area $A_s$

$$F_s = A_s \tau_s \tag{3.7}$$

Likewise, the shear area is related to the undeformed chip area $A = wt_c$ by

$$A_s = \frac{A}{\sin \phi} \tag{3.8}$$

where $w$ is the chip width and $t_c$ is the chip thickness. The cutting ratio is obtained by applying mass continuity theory, as follows:

$$r = \frac{h}{t_c} = \frac{\sin \phi}{\cos(\phi - \alpha)} \tag{3.9}$$

where $h$ is depth of the cut (scriber indentation depth into surface). For the surface patterning process, we can write the instantaneous surface contact force in vertical direction as

$$F_z = \frac{\tau_s w t_c \sin(\beta - \alpha)}{\sin \phi \cos(\phi + \beta - \alpha)} \tag{3.10}$$

Figure 3.6 shows a schematic for the progress of the chip removal process. The variation in chip thickness over the characteristic time delay $\tau$ is:

$$\Delta t_c(t) = t_c(t) - t_c(t - \tau) \tag{3.11}$$

Substituting Eq. (3.9) into Eq. (3.11) yields

$$\Delta t_c(t) = \frac{h(t) \cos(\phi - \alpha)}{\sin \phi} - \frac{h(t - \tau) \cos(\phi - \alpha)}{\sin \phi} \tag{3.12}$$

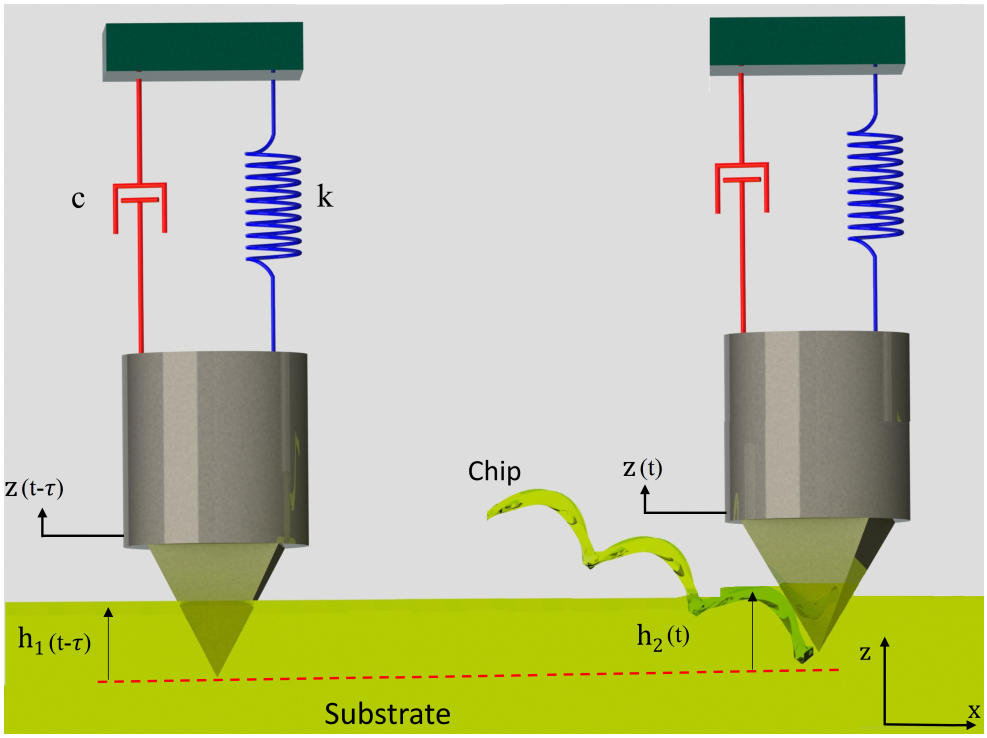


Figure 3.6: Schematic for the cutting process progression over time.

The transnational velocity of the scriber along its planar trajectory can be found as:

$$V_s = w_m r \tag{3.13}$$

where $r$ is radius of the motor shaft

$$\omega_m = \frac{2n\pi}{\tau}$$

is the rotational velocity of the motor shaft, $\tau$ is the motor period, and $n$ is the gearbox ratio. In this case, a high precision servo motor was implemented with a gearbox ratio $n = 1/64$. Therefore the characteristic time of the patterning process can be written as:

$$\tau = \frac{2\pi r}{64 V_s} \tag{3.14}$$

Due to variations in material properties, surface morphology and external disturbances, the depth of cut will vary over a characteristic time $\tau$ from $h(t-\tau)$ to $h(t)$. The resulting vertical reaction force can be represented by:

$$\begin{aligned}\Delta F(t) &= F_z(t) - F_z(t-\tau) \\ &= (t_c(t) - t_c(t-\tau))\frac{w\tau_s \sin(\beta-\alpha)}{\sin\phi\cos(\phi+\beta-\alpha)} \\ &= \Big(h(t) - h(t-\tau)\Big)\frac{w\tau_s \sin(\beta-\alpha)\cos(\phi-\alpha)}{\sin^2\phi\cos(\phi+\beta-\alpha)}\end{aligned} \tag{3.15}$$

where we assume the cutting process parameters remain constant throughout patterning. We can, therefore, rewrite the scriber equation of motions in terms of relative displacement $z(t) = h(t)$ as:

$$\ddot{z} + \frac{c}{m}\dot{z} + \omega_n^2 z = \frac{\Delta F(z)}{m} \tag{3.16}$$

where $\omega_n$ is the natural frequency of the scriber when disengaged from the substrate.

For a wedge-shaped scriber, the width $w$ remains constant as the penetration depth $z$ varies. We can use Eq. (3.15) to rewrite the right hand-side of the equation of motion as

$$\frac{\Delta F(z)}{m} = Cw\omega_n^2\big(z(t) - z(t-\tau)\big) \tag{3.17}$$

where $C$ is a constant relating the scriber geometry and material properties to the shear process

$$C = \frac{\tau_s \sin(\beta-\alpha)\cos(\phi-\alpha)}{k\sin^2\phi\cos(\phi+\beta-\alpha)} \tag{3.18}$$

The value of the $C$ can be obtained by rearranging equation (3.17) to write:

$$C = \frac{1}{wk}\frac{\Delta F}{\Delta h} \tag{3.19}$$

The ratio $\Delta F/\Delta h$ is obtained from figure 3.11 and corresponding average cut width $w$ is found from 3.12. The equation of motion for a wedge-shaped scriber is a linear Delay

Differential Equation (DDE):

$$\ddot{z} + \frac{c}{m}\dot{z} + \omega_n^2 z = Cw\omega_n^2\big(z(t) - z(t-\tau)\big) \tag{3.20}$$

For a cone-shaped scriber, the cone angle $\theta$ relates the chip thickness and width by:

$$w = 2h\tan\theta \tag{3.21}$$

Using this relationship in Eq. (3.15), the right hand-side of the equation of motion can be written as:

$$\frac{\Delta F(z)}{m} = 2\tan\theta\, C\omega_n^2\big(z^2(t) - z^2(t-\tau)\big) \tag{3.22}$$

and the equation of the motion for cone shaped scriber is the nonlinear Delay Differential Equation (DDE)

$$\ddot{z} + \frac{c}{m}\dot{z} + \omega_n^2 z = Cw\omega_n^2\big(z^2(t) - z^2(t-\tau)\big) \tag{3.23}$$

The onset of chatter corresponds to Hopf bifurcation where the scriber tip loses stability at the equilibrium point $z(t) = 0$ and starts to oscillate following harmonic motion of the form:

$$\begin{aligned} z(t) &= a\cos(\Omega t) \\ z(t-\tau) &= a\cos(\Omega t - \Omega\tau) \end{aligned} \tag{3.24}$$

For a wedge-shaped scriber, substituting Eqs. (3.24) into Eq. (3.20) yields

$$\begin{aligned} -a\Omega^2\cos(\Omega t) - \frac{c}{m}a\Omega\sin(\Omega t) + a\omega_n^2\cos(\Omega t) &= aCw\omega_n^2\cos(\Omega t) \\ - aCw\omega_n^2\cos(\Omega t)\cos(\Omega\tau) - aCw\omega_n^2\sin(\Omega t)\sin(\Omega\tau) & \end{aligned} \tag{3.25}$$

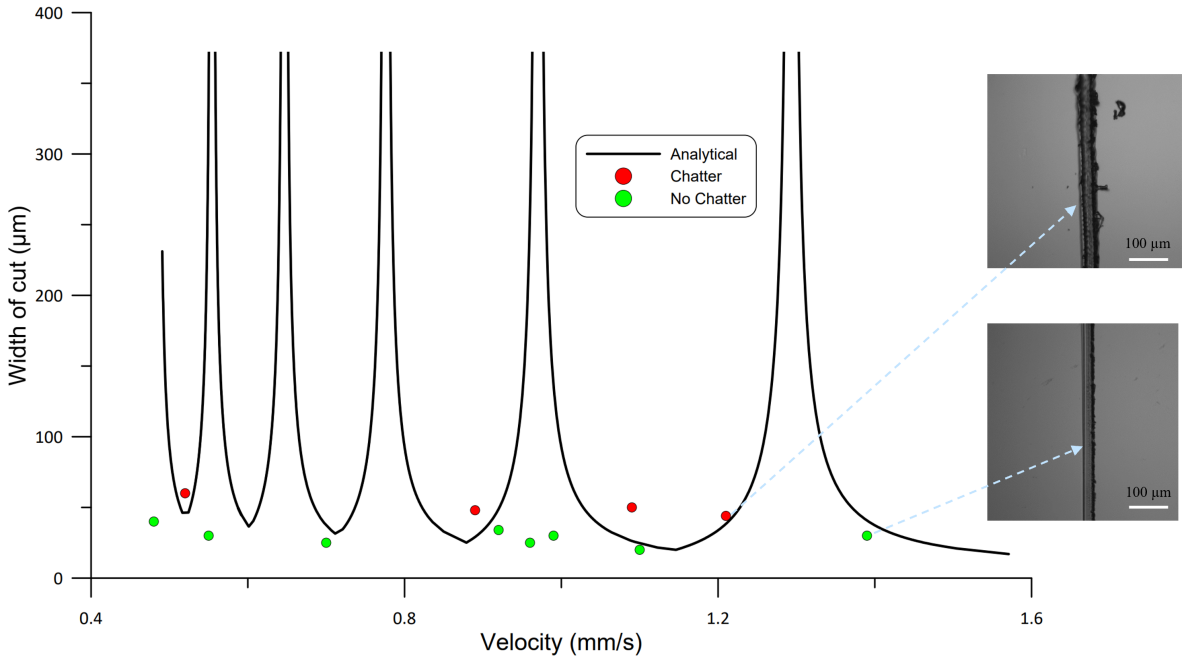


Figure 3.7: Comparison between the analytical and experimental limits of safe patterning zone.

Equating the coefficients of $a\sin(\Omega t)$ and $a\cos(\Omega t)$ on either side of the equation yields:

$$\begin{aligned} -\Omega^2 + \omega_n^2 &= Cw\omega_n^2 - Cw\omega_n^2\cos(\Omega\tau) \\ \frac{c}{m}\Omega &= Cw\omega_n^2\sin(\Omega\tau) \end{aligned} \tag{3.26}$$

We used the scriber and patterning process parameters listed in table 3.1 to solve Eqs. (3.26) for scriber width $w$ and oscillation frequency $\Omega$ at the onset of chatter given the traversing speed and, therefore, $\tau$. We compare, in figure 3.7, the variation in the scriber width at the onset of chatter (Hopf bifurcation) as a function of traversing speed with experimental results for twelve discreet traversing speeds and cut widths. Instances where no chatter was observed are marked in green and instances where chatter was observed, as rough cut edges, are marked in red. The region below the Hopf bifurcation limits

corresponds to stable and safe patterning. The region above the Hopf bifurcation limits corresponds to the regenerative vibrations (chatter) where system is self-excited, unstable and unsafe to create micro features. A good agreement can be seen between experimental and analytical results.

As the width of the cut and scriber velocity increase, the threshold for the chatter (Hopf bifurcation) decreases. Conversely, for smaller micro and nano scale features, chatter is delayed allowing for traversing speed more than 1.5 mm/s for cut widths less than 20 µm.

Table 3.1: Scriber and patterning process parameters.

| | | |
|---|---|---|
| Scriber mass | m (kg) | 0.00347 |
| Damping coefficient | c (N.s/m) | 125 |
| Spring stiffness | k (N/m) | 53.5 |
| Patterning constant | C | 77 x $10^8$ |

## 3.3 Experimental Demonstration

### 3.3.1 Prototypes

Two prototypes of the fabrication station were realized. The first fabrication station, prototype # 1, was made by re-purposing the 3D stage of a microplotter (SonoPlot Inc.). The scriber was attached to an XYZ-stage via a suspension mechanism. The substrate was held fixed on a steel platform by surrounding it with four magnets. The Z-axis was used to approach the substrate and to maintain the scriber-substrate contact force between the throughout the lithography process. The scriber was then commanded, via the microplotter

software interface [77], to move in the XY-plane relative to the stationary substrate, thereby creating the desired patterns.

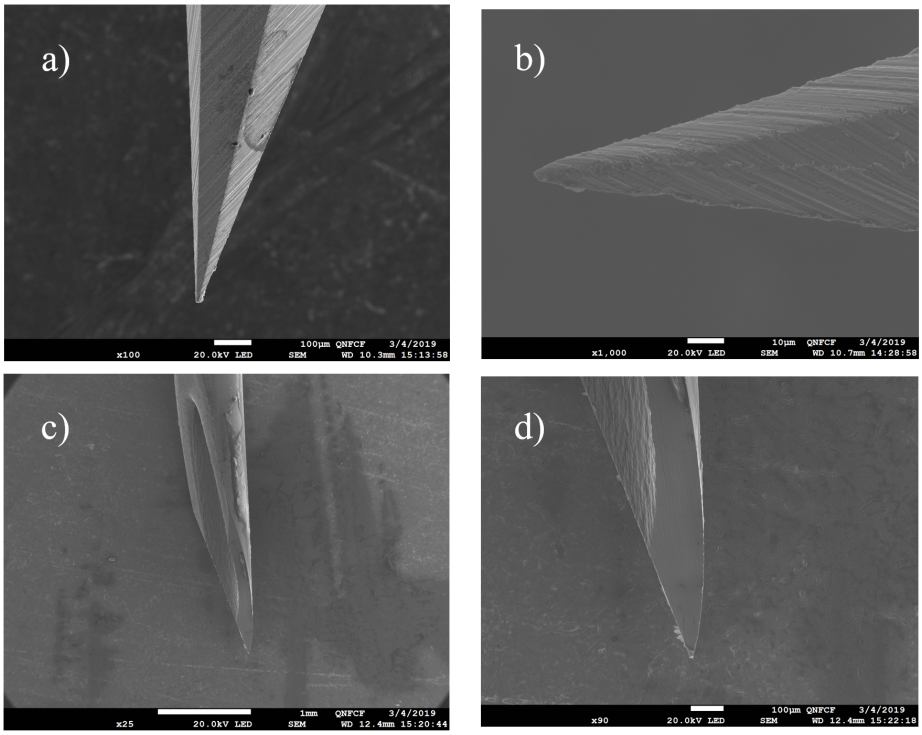


Figure 3.8: SEM images of (a) the tungsten carbide scriber, (b) a close-up view of the carbide tip, (c) the stainless steel scriber, and (d) a close-up view of the stainless steel tip.

Two types of scribers were used to examine the impact of scriber hardness and tip radius on feature characteristics

- stainless steel
- tungsten carbide

SEM images of these scribers are shown in the figure 3.8. The tungsten scriber has an axisymmetric tip cross-section and a tip radius of 3µm. The stainless steel scriber has an asymmetric cross-section with two sharp edges.

The accuracy of the stage is listed as 25 µm [77]. A Point Grey camera and a proximity series 18mm/2.00 lens are attached to the frame and used to monitor the progress of the fabrication process. Optical image of microplotter experimental setup is shown in figure 3.9.

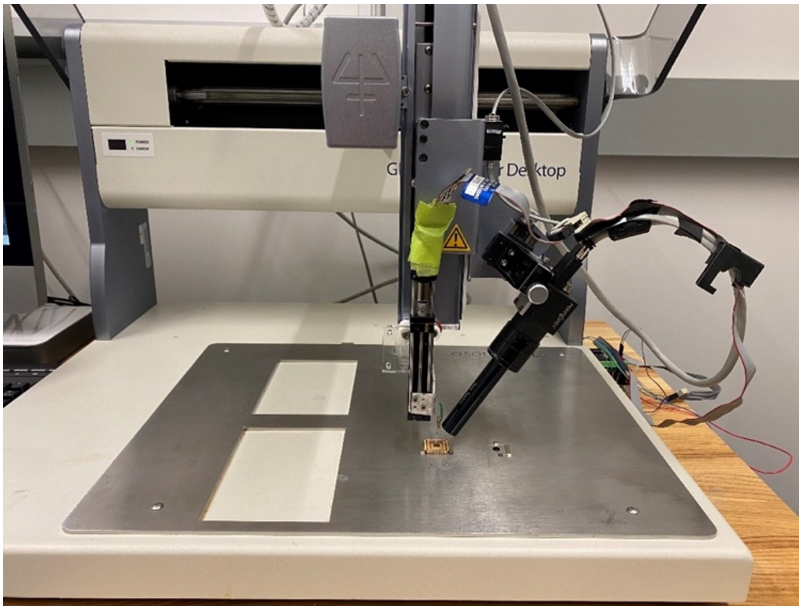

Figure 3.9: Microplotter experimental setup.

The channels shown in figure 3.2 are an example of negative patterning using prototype #1 and stainless steel scribers. In this case, the channel pitch was set to 52.5 µm. However, the figure shows that it varies from 25 µm to 100 µm due to inadequate stage accuracy. Therefore, a second prototype utilizing a purpose-built nano-resolution stage was developed.

The second fabrication station, prototype # 2, was made of three National Aperture (MM-3M-EX-2) servo motors, and each with a working range of 60 mm and an accuracy of 500 nm. They were assembled into a specially designed rigid stage. A controller was

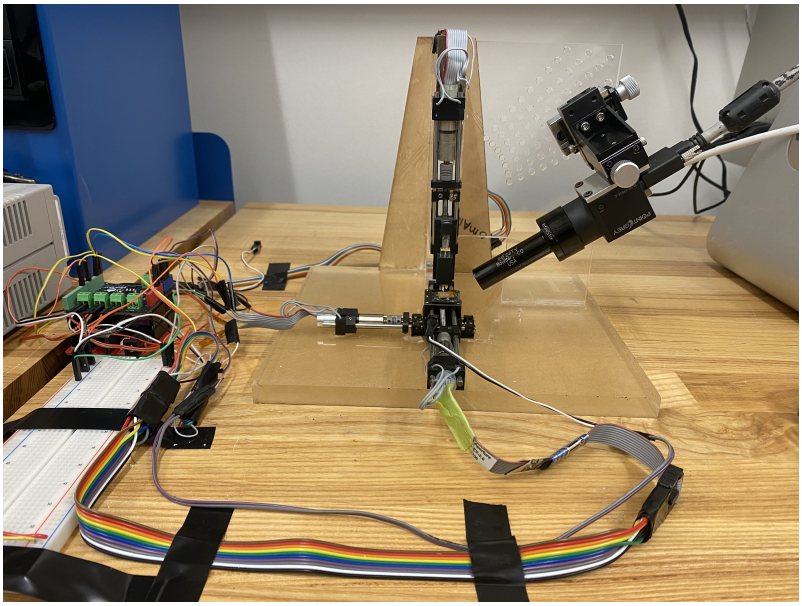

Figure 3.10: Custom built 500 nm resolution 3D nanostage for d-SPL method.

developed based on the Teensy 4.0 board to drive the motors. The same scribers and suspension mechanism described above were also used in this case. Custom control algorithm was developed to address the issues and to have flexible control in the patterning process. Optical image of the custom 3D nanostage and control setup were shown in the figure 3.10.

### 3.3.2 Calibration and characterization

First, the fabrication station is implemented to obtain relationship between substrate contact force and depth, and width. Multiple events are carried out to acquire repeatability and uniformity of d-SPL method. Relationship between force and depth, and width can be found in figure 3.11 and figure 3.12 respectively. As can be seen from these figures, an example for the creation of 5 µm width and 500 nm depth channel, 500 mN force is required using the tungsten carbide scriber. Both figures show that depth and width of

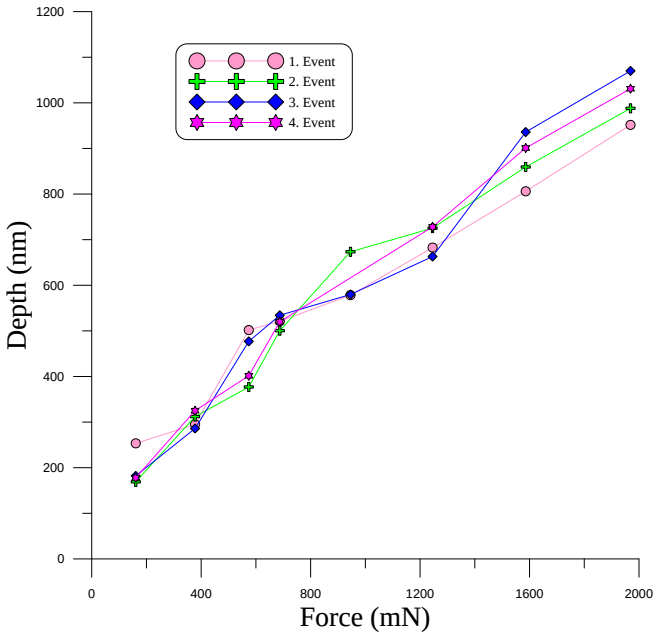


Figure 3.11: Force-depth relationship on a PMMA substrate.

channel increases linearly with proportional of the force applied. However increase in the depth is greater than width since higher stress occurs towards tip patterning tool. These events show that d-SPL method can produce the features repeatably.

The following methods were used to characterize the patterned substrates:

- A Veeco white-light profilometer was used to extract the surface profiles which were then processed to obtain the relationships of applied force to width and depth of the surface features.

- A Bruker Atomic Force Microscope (AFM) was deployed to obtain 3D surface topography of $15 \times 15\,\mu m^2$ areas of the patterned substrates.

- A JEOL JSM-7200F Scanning Electron Microscope (SEM) was used to image the

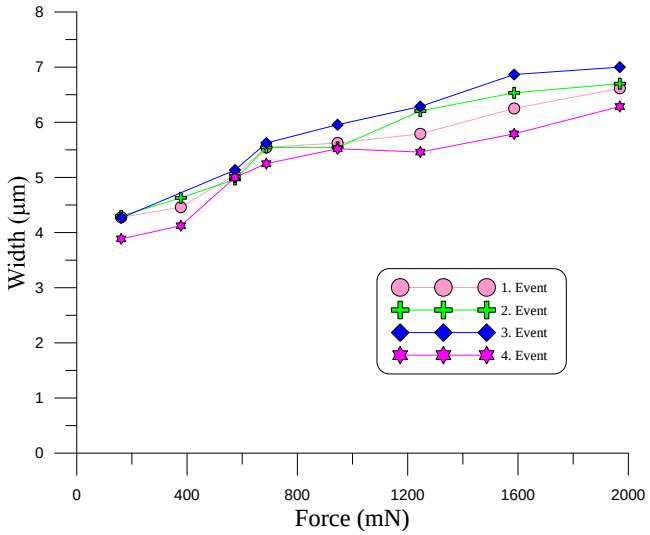


Figure 3.12: Force-width relationship on a PMMA substrate.

scribers tips and micro and nanowires.

- A Nikon microscope was used to acquire optical images of the finished substrates.

### 3.3.3 Formation of continuous and discontinuous chips

Chip formation can be divided into two categories: continuous and discontinuous chip removal processes. Continuous chip formation is a process of shear without fracture. Only plastic deformation occurs during this process. Discontinuous chip formation is a process of shear with fracture. Thereby, plastic deformation and fractures occur during this process. The chip formation type relies on the cutting conditions and the material properties of the workpiece [78]. It is known that decrease in the rake angle or an increase in cut depth might result in discontinuity in the chip formation. Various cutting velocity values and with different tool shapes were investigated to understand the numerical modelling for the

continuous chip formation in metal cutting and it was found that morphology of chip can be influenced by the cutting parameters[79, 80]. We also experimentally observed that cutting velocity and rake angle are to have an effect in the formation of the chip from continuous to discontinuous formation. In the experiments, it was also observed that chips are forming into the shape of helical curling.

## 3.4 Results and Discussion

### 3.4.1 Prototype # 1

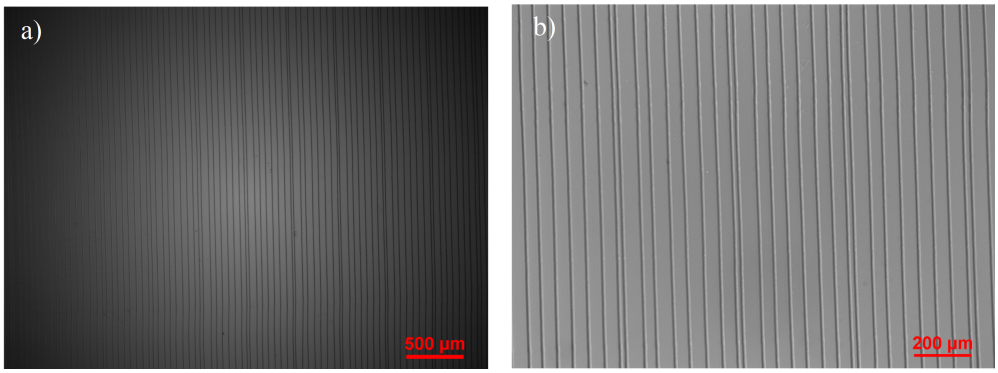


Figure 3.13: (a) Approximately 85 channels patterned on PMMA substrate. (b) Magnified optical images of patterns.

Prototype # 1 was used to an array of 6000 1 cm-long microchannels with a pitch of 50 µm in a PMMA substrate. When it patterns the PMMA substrate, plastic deformation and material fracture can be observed depending on the sharp edges of scriber tip. Figure 3.13(a) shows a few millimeters long eighty five channels patterned on PMMA substrate.

Uniformity and repeatability of the channels produced by d-SPL method can be seen

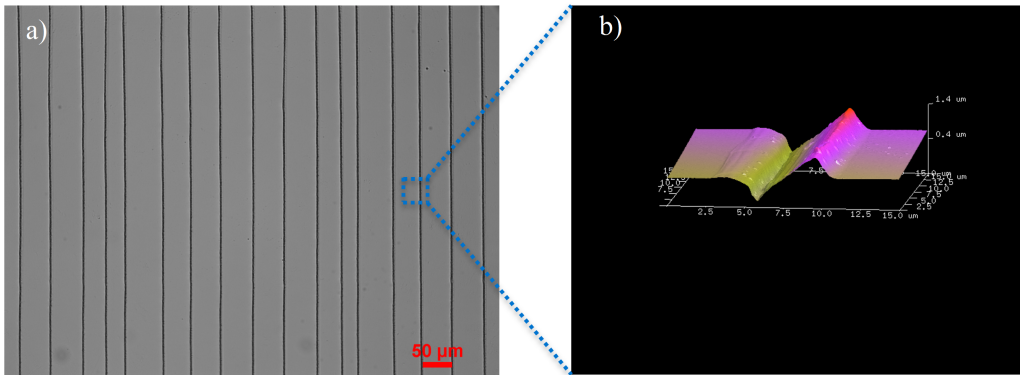


Figure 3.14: (a) Closer view of the channels with scale bar 50 µm. (b) AFM image of the 15 x 15 $\mu m^2$ area that shows patterned groove and material flow due to plastic deformation.

in figure 3.13(b). Multiple, uniform and repeatable patterns are 1 centimeter long, and 2.5 µm wide and 600 nm deep. Figure 3.14(a) depicts magnified optical image of patterns with scale bar of 50 µ, and figure 3.14(b) shows AFM image of a small micro scale of the pattern in area of 15 $\times$ 15 $\mu m^2$. It can be seen from the AFM image that there is only plastic deformation occurred in this event because the tip has one sided sharp edge, therefore the tip created material flow on the edge of pattern. Since features are created by using the prototype # 1, pitch between the channels are not equal due to the stage accuracy.

It is not possible to show centimeter long micro channels and all patterns under the optical microscope because of the limit in the field of view. To be able to observe the variation in the channels, cross section profiles of one centimeter long channel in the beginning, middle and end of the channel were measured using an AFM and the results are shown in the figure 3.15. It is observed that there is a slightly (negligible) variation during one centimeter long patterning.

When a scriber tip with sharp edges was used for the patterning, helical shaped continuous PMMA chips and plastic deformation are observed. Since sharp edges creates high

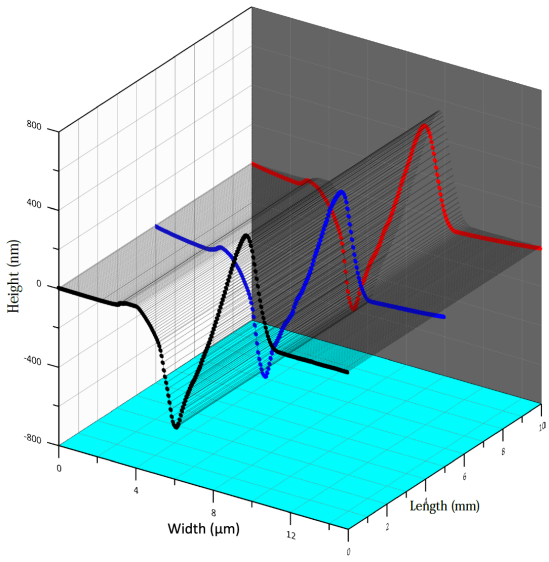


Figure 3.15: Cross section profiles of 1 cm long the nanochannels measured in the beginning, middle and end points of the channel using an AFM.

stress on the edge of grooves that is adequate to remove the PMMA material. Regardless of sharp edges implemented, material flow due to plastic deformation appears to always exist in the patterning event. Figure 3.16(a) demonstrates optical image of the patterned multiple channels and PMMA chips. Figure 3.16(b) and (d) depict closer view of the channels and the chips respectively. The figure 3.16(c) approximately 2.5 mm long helical shaped PMMA chips. Moreover, long chips are also considered as another remarkable proof of the uniformity and repeatability of the d-SPL method introduced here.

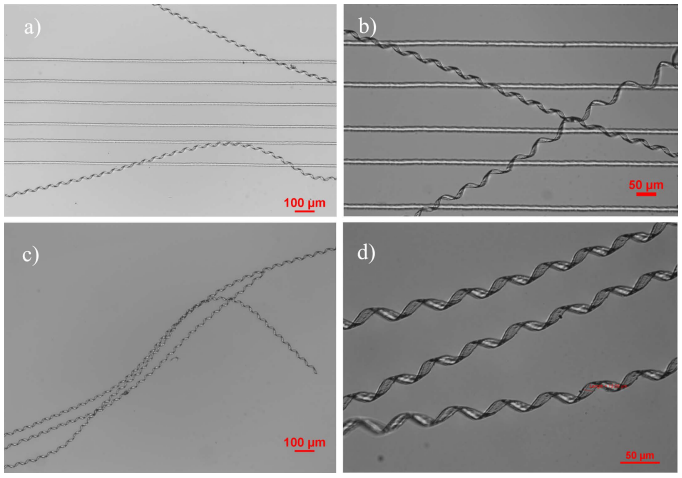


Figure 3.16: (a) Optical image of channels and helical shaped PMMA chips created by tungsten tip with sharp edges via d-SPL method. (b) closer view of the channels and the chips. (c) An image of 2.5 millimeter long three PMMA chips removed from PMMA. (d) Closer views of the long chips showing details.

### 3.4.2 Prototype # 2

Since microplotter has an accuracy of 25 µm, it is not employed for the patterns that require high precision control, particularly for the positive patterning. Because, positive patterning must have the design completely isolated from the material. When the chip is removed from the material, there should not be any skipping the surface patterning as well as having a constant pitch as commanded. Thereby, custom built 3D stage with nano resolution is developed and implemented for the positive and negative patterning with high accuracy. Positive patterning is more applicable to fabrication of the electrodes with high capacitance.

During the continuous chip removal process, micro and nano wires are formed in the shape of the helical. Initially, 600 nm thin gold film deposited on a substrate were deployed

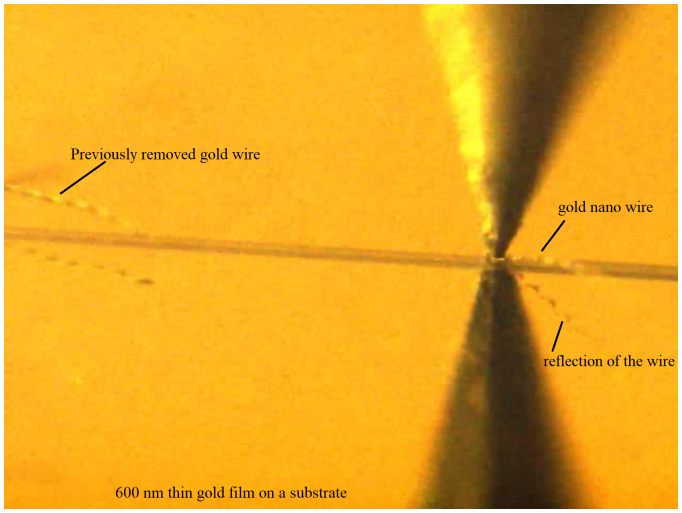


Figure 3.17: Real time optical image of gold nano wires fabricated via d-SPL method through continuous chip removal process

to remove the chips via d-SPL using the 3D nanostage. Figure 3.17 shows an optical image taken during the real time fabrication of continuous helical chips forming gold nano wires. SEM images of the fabricated helical gold nano wires were obtained and demonstrated in the figure 3.18. According to the SEM characterization, the dimensions of the wire are: 600 nm thick, 10 µm wide and a few millimeters long. Then, modal analysis of the nano wire was carried out through a non-contact measurement method using the Laser Doppler Vibrometer (LDV). Fabricated helical shaped gold nano wire was subjected to thermal noise excitation under the LDV and free mechanical response of the nano wire in the air was measured over Fast Fourier Transform (FFT) domain. Figure 3.19(a) shows modal analysis results of the gold nano wire under the thermal noise excitation. Figure 3.19(b) shows optical image of the gold nano wire and laser spot where the FFT measurements were obtained.

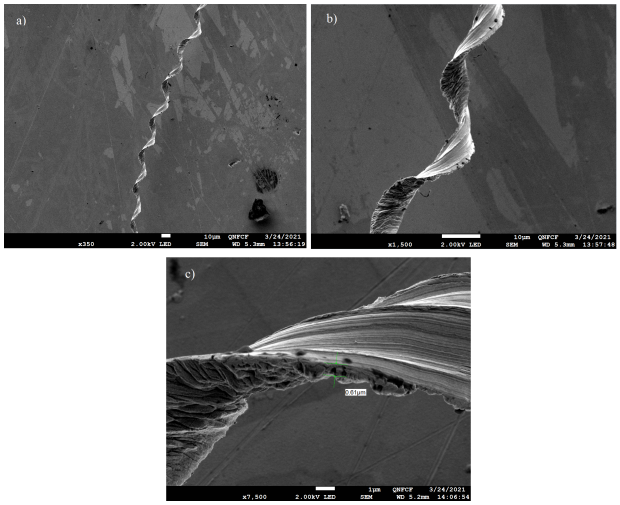


Figure 3.18: SEM images of gold nano wire. (a) The part of uniform and millimeter long gold nano wire. (b) Close-up view of the wire. (c) Gold nano wire thickness and bottom surface of the wire.

$$Q = \frac{F_c}{F_h - F_l} \tag{3.27}$$

The first five natural frequencies of the nano wire were found to be in the range of 40 kHz. Quality factor of the first natural frequency is found to be 49 using the half bandwidth power given in the equation 3.27. Where Q is the quality factor, $F_h$ higher cut-off frequency and $F_l$ is the lower cut-off frequency.

The d-SPL method was then deployed to remove the chips on a PMMA substrate using the tungsten carbide scriber. Millimeter long helical PMMA micro wires were produced. The length of the wire can be controlled by the input command given to Teensy microcontroller. These wires were then coated with thin layer of silver using sputtering to make the wires conductive and reflective. SEM images of helical silver coated PMMA micro wires were then obtained and demonstrated in the figure 3.20. The wire dimensions are varying

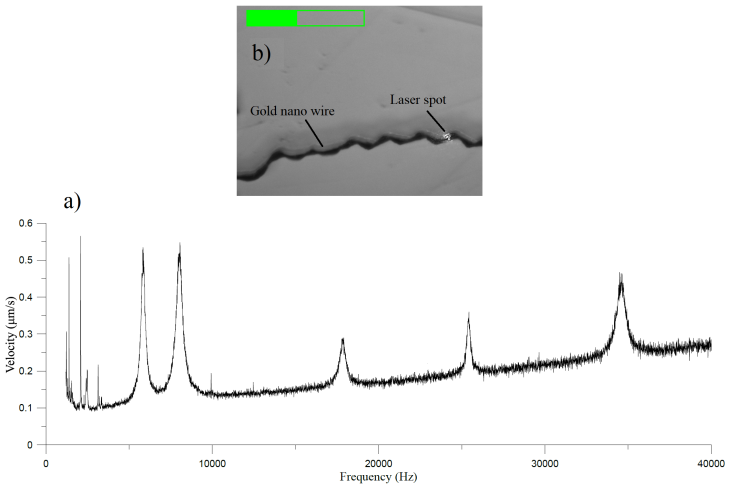


Figure 3.19: (a) Modal analysis of gold nano wire under the thermal noise. (b) Optical image of gold nano wire and laser spot where the FFT measurements were obtained.

from 50 to 100 µm wide and 1 to 3 µm thick depending on the initially defined tip-substrate contact force. As it can be noticed from the figure 3.20, some of these wires can withstand as suspended helical beam. The modal analysis of these micro wires were also carried out. The wires subjected to thermal noise excitation and the free mechanical response of these micro wires in the air was measured over FFT domain using the LDV. Figure 3.21(a) shows modal analysis of the silver coated PMMA micro wire. Figure 3.21(b) shows optical image of the silver coated PMMA wire and laser spot where the FFT measurements were obtained. The first five natural frequencies measured are below 30 kHz. The quality factor of the first peak was found to be about 50.

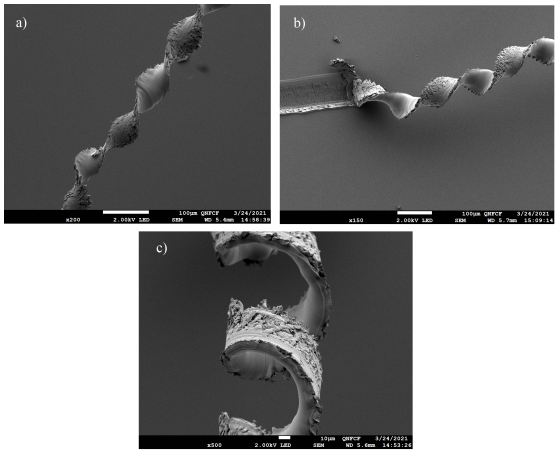


Figure 3.20: SEM images of silver coated PMMA micro wires.

## 3.5 Summary

We demonstrated a novel, benchtop, and low-cost, micro and nano fabrication method dubbed dynamic scanning probe lithography method (d-SPL). It employs a scriber mounted to a 3D nanostage and supported by a spring-damper suspension mechanism to fabricate centimeter long uniform nanoscale surface patterns in seconds. The spring in the support mechanism alleviates problems arising from misalignment between the scriber and surface from surface topography by allowing the scriber tip to move up and down and regulates (minimizes) variations in the spring-surface contact force, thereby creating a flexible working distance. The damper absorbs the scriber residual vibrations due to external disturbances and micro-impacts between the scriber tip and surface asperities. As a result, d-SPL can handle both atomically flat as well as rough substrate surfaces as long as their roughness are within the system working distance. The mechanism also helps to reduce scriber tip wear and failure.

The method enables rapid fabrication of long micro and nanochannels. Combined with

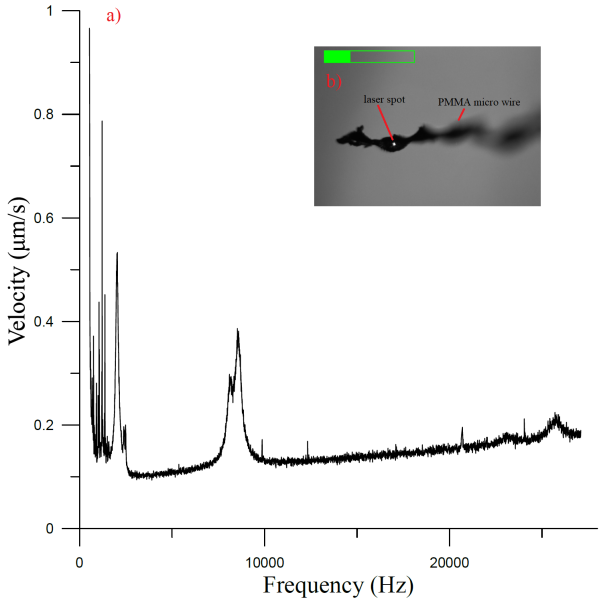


Figure 3.21: (a) Modal analysis of the silver coated PMMA micro wire under the thermal noise. (b) Optical image of the wire and laser spot where the FFT measurements were obtained.

polymer casting techniques, it can be used to create both positive and negative surface features. The d-SPL method produced features in 2.5 µm wide, 600 nm deep 1 centimeter long. Feature dimensions can be controlled by scriber contact force and scriber tip size.

Using the d-SPL method, micro and nano wires can be also fabricated through continuous chip removal process. Some wires were observed to stand as suspended beam and they were characterized and their frequency response was measured using the LDV. It was experimentally found that these wires have quality factors about 50. Nano wires produced via d-SPL are 600 nm thick and can be as long as 5 millimeter.

To fundamentally understand mechanical behavior of the d-SPL method, an analytical model was developed to explain the functioning principle of the d-SPL as well as its safe

operation conditions and limitations. Small micrometer scale chattering in patterning was also observed for the first time, which was also validated through experiments.

# Chapter 4

# Triboelectric Energy Harvesters

In this chapter, d-SPL method has been deployed for rapid and low-cost surface modification of the triboelectric films. Nano Grooves (NGs) and nano triangular prisms (NTPs) were created on the negative triboelectric film to increase the effective contact area and thereby enhancing the output power of the TENGs.

We also developed an electromechanical analytical model to fully understand fundamental behavior of the TENG device and to design low-frequency and wide-band triboelectric energy harvesters. The results obtained from the model then were validated through experiments.

## 4.1 Introduction

Demand for distributed electrical power has seen a significant growth as Internet of Things applications come to market creating demand for dense sensor networks made of many millions of nodes [81, 82]. Localized power supply is an attractive approach to power those

networks, which is driving a search for new power supply modalities. Waste mechanical vibrations is a promising distributed power source readily available in many environments [83–86].

Waste vibrations have been converted into electrical energy using piezoelectric [87], electromagnetic [88] and electrostatic nanogenerators [89]. All of these methods are potentially clean, highly efficient and environment friendly [90]. A new type of electrostatic nanogenerators, triboelectric nanogenerators (TENGs), were introduced in 2012 [91]. TENGs convert mechanical vibrations into electrical energy by exploiting the triboelectric effect to provide the voltage source necessary for electrostatic induction [92–94]. Upon separation of a metallic and a dielectric film, the metal loses electrons becoming positively charged while the dielectric gains electrons becoming negatively charged [95, 96]. The two charged films serve as a voltage source within a variable capacitor [97]. In turn, the capacitor drives current between its plates as they move with respect to each other under the influence of mechanical vibrations [98].

TENGs can provide a power density in the range of $mW/cm^2$ sufficient to power many autonomous sensor nodes and other self-powered portable electronic devices [99–101]. A variety of materials with opposite polarity have been implemented in TENGs to improve their efficiency, particularly polytetrafluoroethylene (PTFE) and poly-dimethylsiloxane (PDMS) are frequently chosen as negative triboelectric material due to their high tendency to receive electrons [102–104].

The output power of TENGs has also been enhanced by creating nanostructured triboelectric surfaces, thereby increasing the contact area between the two triboelectric films. This allows more freely moving electrons to leave the metallic film to the dielectric film resulting in a higher voltage drop between the two films and increasing the output power of TENG [105–107]. Two classes of fabrication methods have been adopted to achieve this

goal. The first creates those structures using oxides, by etching of $TiO_2$ nanowires and nano-sheets into Ti films [108], chemical synthesize of $SiO_2$ nanoparticles on $SiO_2$ films [109], and growing of ZnO nanorods on indium tin oxide (ITO) films [110], or metals, by etching of gold flowers into gold films [111]. The second creates nano-features, such as PDMS nanopillars [112], PDMS triangular pyramids, and PDMS triangular ridges [111], by molding polymers using standard imprint lithography (SIL).

Currently, the creation of those nano-features requires use of cleanroom facilities, for electrochemcial deposition [113, 114] or standard soft lithography [115], thereby imposing cost and access barriers on TENGs technology. Alternatively, available low-cost and rapid fabrication methods such as $CO_2$ laser ablation method are not able to produce features less than 50 µm which limits the maximum surface area, in turn power generation. In this study, we employ a novel and low cost bench-top d-SPL method to fabricate micro and nano features. The method allows us to introduce massive arrays of one centimeter long nano grooves (NGs) and nano triangular prisms (NTPs) on a Poly(methyl methacrylate) (PMMA) substrate. It employs a micro-resolution 3D stage equipped with a micro-sized tip via a spring-damper system. In total, twelve thousand NGs and NTPs are patterned on a $6 \times 5\,\mathrm{cm}^2$ PMMA substrate, which is then used as a mold to transfer those features into PDMS substrates using spin coating. The fabricated PDMS films serve as the negative triboelectric layer while aluminum (Al) foil is used as the positive triboelectric layer. The output power of the fabricated TENG is compared to that of an identical TENG made using a flat surface PDMS layer. Some of these triboelectric materials are shown in the figure 4.1.

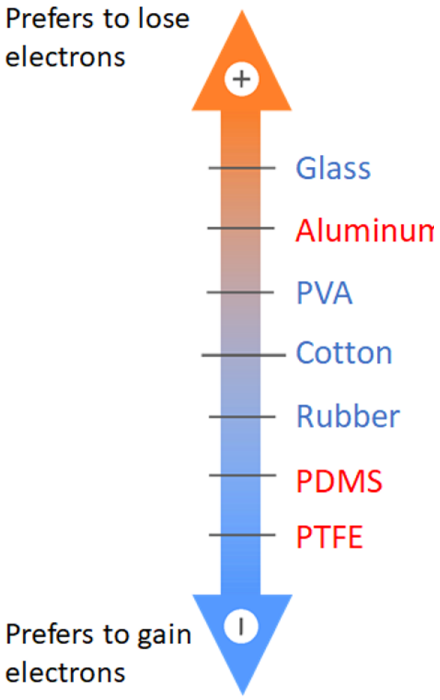


Figure 4.1: List of positive and negative some triboelectric materials.

## 4.2 Working Principle

Figure 4.2 shows a schematic of the harvesting elements and their interaction throughout the harvesting cycle. The TENGs generates an alternating current as the external (host) vibrations cycle the harvesting elements through contact and separation states and the TENG undergoes the corresponding triboelectrification and electrostatic induction stages. Initially, the two electrodes are neutral and separate from each other. Under external vibrations, the top Al electrode and PDMS film come into contact. At this point, triboelectric charge generation begins as electrons are injected from Al to PDMS.

As separation begins, the top plate moves upward under the influence of the springs

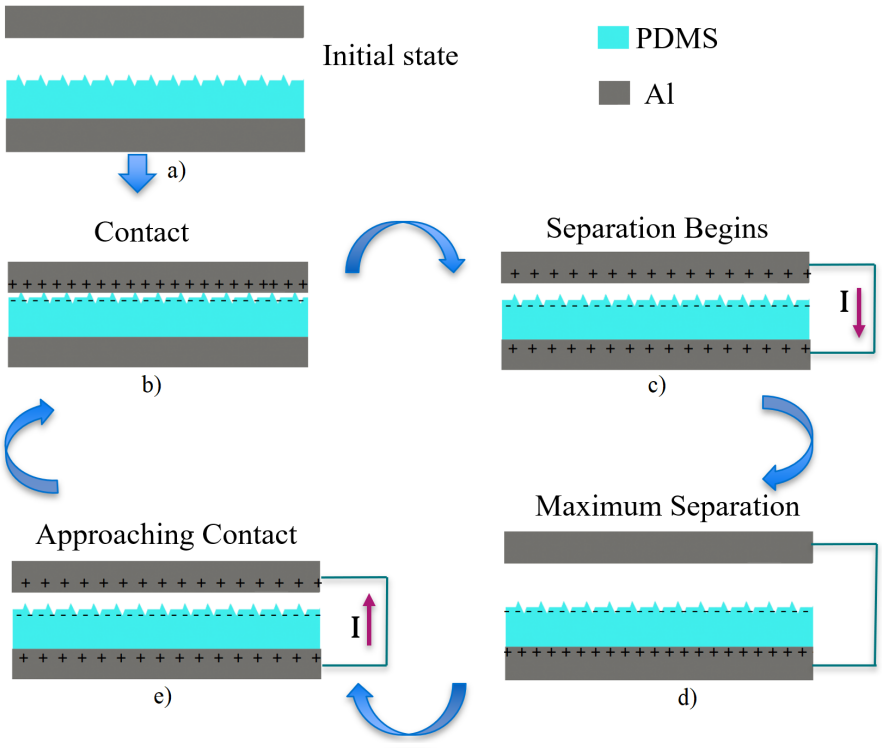


Figure 4.2: (a) Initial state and no mechanical force applied. (b) Al foil and thin PDMS film are brought into contact by applying external force. (c) Withdrawing the force results in a separation, and electrons began to move from bottom electrode to top electrode, an AC current flows forward through a connected wire due to potential difference between electrodes. (d) All positive triboelectric charges are screened to bottom electrode due to electrostatic induction. (e) After reapplying the force and approaching the contact, electrons are screened back to bottom electrode as a result of the induction.

restoring force acting against the internal electric field between the charges distributed on the two triboelectric surfaces. As a result, electrons flow from the bottom (negative) electrode to the top (positive) electrode under the influence of electrostatic induction between the PDMS film on the bottom electrode. This process terminates when the top plate reaches maximum separation distance. As it reverses direction and approaches the bottom plate, current flows in the reverse direction as electrons flow from the top electrode under the influence of the electrostatic induction of the PDMS film on it to the bottom electrode. The cycle terminates with the triboelectric films coming back into contact.

## 4.3 Analytical Model

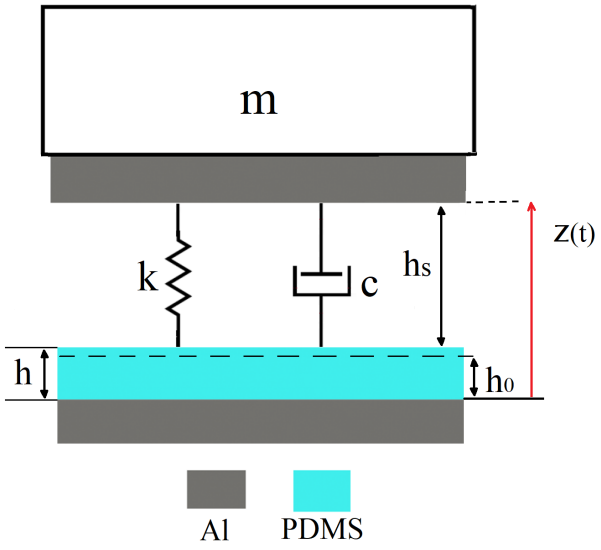


Figure 4.3: A schematic to model triboelectric nanogenerators.

Mahmoud et al. [116] introduced an analytical model for out-of-plane electrostatic micro-power generators (MPGs). They present a coupled electromechanical model for

wide-band and low-frequency energy harvesters. Bendame et al. [88] developed an impact based electromagnetic vibration energy harvester and validated a piecewise-linear model for it. An electrical model for contact mode triboelectric nanogenerators (TENGs) was introduced by Niu et al [95]. They also presented an analytical relationship between a resistive load and output power. Building on the model by Bendame et al. [88], Ibrahim et al [117] presented a coupled electromechanical model for triboelectric energy harvesters. The does not account completely for the electrostatic force. Therefore, it is useful to develop of complete and consistent model for TENGs.

Herein, we developed an analytical model for wide-band and low-frequency TENGs since vibrations in the environment are predominantly less than 10 Hz. Figure 4.3 shows a schematic for contact mode of TENGs. We define the relative displacement between the lower surface of sprung (inertial) mass $m$ electrode and the base as

$$z(t) = x(t) - y(t) \tag{4.1}$$

where $x(t)$ is absolute displacement of the sprung mass and $y(t)$ is absolute displacement of the base. The potential difference between them can be written as:

$$V = E_1 h + E_2(z - h) \tag{4.2}$$

where $E_1$ and $E_2$ are electrical fields in the dielectric film and the air gap, respectively and $h$ is the undeformed thickness of the PDMS film. The fields $E_1$ and $E_2$ are given by [95]

$$E_1 = \frac{-q}{\epsilon_0 \epsilon_r A} \tag{4.3}$$

$$E_2 = \frac{-q + A\sigma}{\epsilon_0 A} \tag{4.4}$$

where A is the contact area, $\epsilon_0$ and $\epsilon_r$ are the permittivity of air and relative permittivity of PDMS film, respectively, $h_s$ is the gap between the PDMS surface and the top electrode,

and $h_0$ is the thickness of the fully compressed PDMS. The charge on the electrodes is dubbed as $q$ whereas the density of the negative charge distribution on the PDMS surface is dubbed $\sigma$.

Substituting Eqs. (4.3) and (4.4) into Eq. (4.2) yields

$$V = \frac{-q}{\epsilon_0 \epsilon_r A} h + \frac{-q + A\sigma}{\epsilon_0 A}(z - h) \tag{4.5}$$

If the top and bottom electrodes are connected through a resistor. Voltage across a resistor can be written as:

$$V = IR = \frac{dq}{dt} R \tag{4.6}$$

Setting equations (4.5) and (4.6) equal to each other yields

$$\frac{dq}{dt} = \dot{q} = \frac{-q}{R\epsilon_0 A}\left(\frac{h}{\epsilon_r} + (z - h)\right) + \frac{\sigma}{R\epsilon_0}(z - h) \tag{4.7}$$

The TENG variable capacitor is made of two capacitors connected in series. A capacitor $C_2$ between the top electrode and the PDMS surface and a capacitor $C_1$ between the PDMS surface and the bottom electrode. When the TENG is in non-contact, their individual capacitances are given by:

$$C_1 = \frac{\epsilon_r \epsilon_0 A}{h} \tag{4.8}$$

$$C_2 = \frac{\epsilon_0 A}{z - h} \tag{4.9}$$

and their total capacitance is calculated as:

$$C = \frac{\epsilon_0 \epsilon_r A}{h + \epsilon_r (z - h)} \tag{4.10}$$

The electrostatic force between the parallel-plates of this capacitor can be derived by applying Castigliano 's theorem to the electrostatic potential as:

$$F_e = -\frac{q^2}{2\epsilon_0 A} \tag{4.11}$$

When the TENG is in contact, its variable capacitor is made of a single capacitor filled with the PDMS layer under compression between the two electrodes. The potential difference can then be written as:

$$V = E_1 z \tag{4.12}$$

Substituting Eq. (4.3) into Eq. (4.12) yields

$$V = \frac{-q}{\epsilon_0 \epsilon_r A} z \tag{4.13}$$

Setting equations (4.13) and (4.6) equal to each other yields

$$\dot{q} = -\frac{q}{R\epsilon_0 \epsilon_r A} z \tag{4.14}$$

The TENG variable capacitor during the contact is given by:

$$C = \frac{\epsilon_r \epsilon_0 A}{z} \tag{4.15}$$

and electrostatic force is found as:

$$F_e = -\frac{q^2}{2\epsilon_0 \epsilon_r A} \tag{4.16}$$

The equation of motion for the sprung mass $m$ can be written as:

$$m\ddot{z} = -F_s - F_d - F_e - m\ddot{y} \tag{4.17}$$

$F_s$ is the net force of the springs acting on the mass and $F_d$ is the damping force.

The coupled electromechanical system is composed of the equation of motion of the sprung mass given in Eq. (4.17), and the current equation through the resistive load

$$\dot{q} = \begin{cases} \frac{-q}{R\epsilon_0 A}\left(\frac{h}{\epsilon_r} + (z-h)\right) + \frac{\sigma}{R\epsilon_0}(z-h) & z > h \\ -\frac{q}{R\epsilon_0 \epsilon_r A} z & z \leq h \end{cases} \tag{4.18}$$

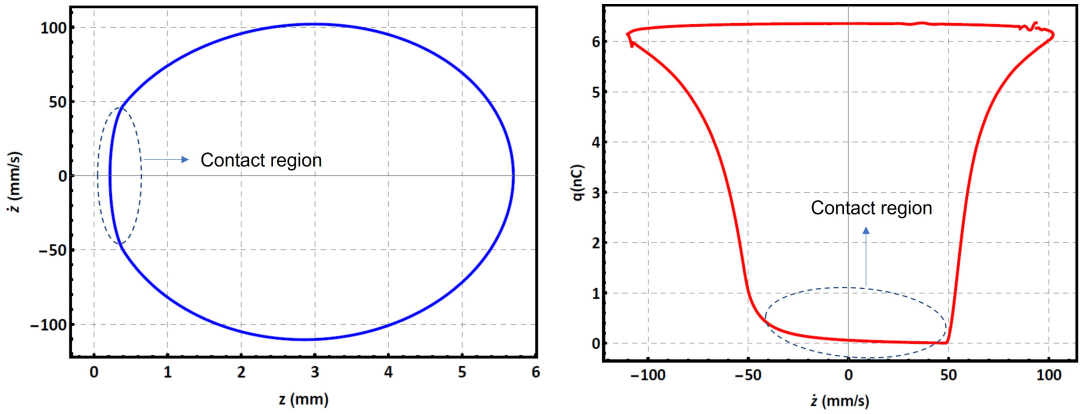


Figure 4.4: Phase portraits of (a) the displacement-velocity and (b) the velocity-charge of the TENG for a base acceleration with $a_\circ = 0.3g$ and $\Omega = 6\,\text{Hz}$, and the resistor $R = 79\,\text{M}\Omega$.

The net spring forces can be expressed as:

$$F_s = \begin{cases} k_1(z - h - h_s) & z > h \\ k_1(z - h - h_s) - k_2(z - h) & h_0 < z \leq h \\ k_1(z - h - h_s) - k_2(z - h) + k_3 z & z \leq h_0 \end{cases}$$

where $h + h_s$ is the length of the support springs while the mass is at the equilibrium position, $k_1$ is the effective stiffness of the springs, $k_2$ is the linear stiffness of the PDMS layer, and $k_3$ is the stiffness of the fully compressed PDMS layer stiffness.

The damping forces can be expressed as

$$F_d = \begin{cases} c_1\dot{z} & z > h \\ c_1\dot{z} + c_2 z^2\dot{z} & z \leq h \end{cases}$$

where $c_1$ is a linear viscous damping coefficient and $c_2$ is a nonlinear damping coefficient representing energy losses due to impact and viscoelasticity during contact.

Electrostatic forces can be expressed as

$$F_e = \begin{cases} F_e = -\frac{q^2}{2\epsilon_0 A} & z > h \\ F_e = -\frac{q^2}{2\epsilon_0 \epsilon_r A} & z \leq h \end{cases}$$

The couple electromechanical model can be expressed in piecewise form as follows:

$$h < z \;\Rightarrow \begin{cases} m\ddot{z} = -k_1(z-h-h_s) - c_1\dot{z} + \frac{q^2}{2\epsilon_0 A} - m\ddot{y} \\ \dot{q} = \frac{-q}{R\epsilon_0 A}\left(\frac{h}{\epsilon_r} + (z-h)\right) + \frac{\sigma}{R\epsilon_0}(z-h) \end{cases}$$

$$h_0 < z \leq h \;\Rightarrow \begin{cases} m\ddot{z} = -k_1(z-h-h_s) + k_2(z-h) - c_1\dot{z} - c_2 z^2\dot{z} + \frac{q^2}{2\epsilon_0\epsilon_r A} - m\ddot{y} \\ \dot{q} = -\frac{q}{R\epsilon_0\epsilon_r A} z \end{cases}$$

$$z \leq h_0 \;\Rightarrow \begin{cases} m\ddot{z} = -k_1(z-h-h_s) + k_2(z-h) - k_3 z - c_1\dot{z} - c_2 z^2\dot{z} + \frac{q^2}{2\epsilon_0\epsilon_r A} - m\ddot{y} \\ \dot{q} = -\frac{q}{R\epsilon_0\epsilon_r A} z \end{cases}$$

The electromechanical system was solved numerically in Mathematica using a shooting method to obtain the steady-state response. The system response was simulated under the harmonic base excitation

$$\ddot{y}(t) = a_\circ \cos(\Omega t)$$

where $a_\circ$ and $\Omega$ are the amplitude and frequency of base acceleration. The system parameters used in the simulations are listed in Table 4.1.

The behavior of the TENG was further explored by plotting the phase portraits of system, namely the phase portrait of the mechanical subsystem (displacement-velocity),

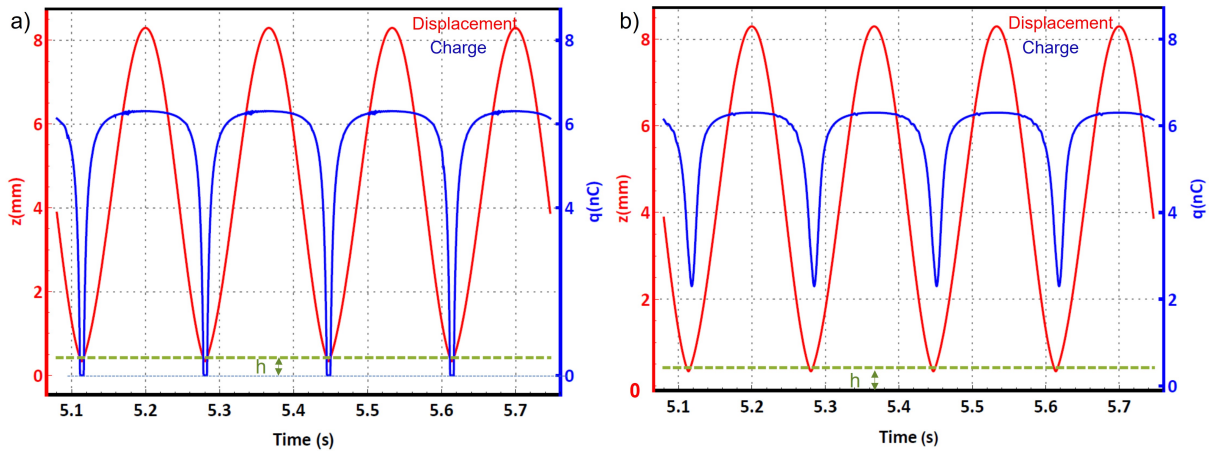


Figure 4.5: The simulated steady-state relative displacement of the sprung mass $z(t)$(red line) and charge $q(t)$ generated (blue line) through the resistor $R = 1\,\mathrm{M\Omega}$ (a), and the resistor $R = 79\,\mathrm{M\Omega}$ (b), over 4 excitation periods under a base acceleration with an amplitude and frequency of $a_\circ = 0.3\,\mathrm{g}$ and $f = 6\,\mathrm{Hz}$.

figure 4.4(a), and that of the electromechanical subsystem (velocity-charge), figure 4.4(b). The contact phase of the TENG can be seen in the phase portrait of the mechanical subsystem. During the contact mode, The displacement of the sprung mass does not change as its velocity changes. The charge was found to be minimum when velocity of the sprung mass is approximately 50 mm/s.

The steady-state response to a base acceleration with an amplitude and frequency of $a_\circ = 0.3\,\mathrm{g}$ and $f = 6\,\mathrm{Hz}$ is shown for using a harvesting resistor of $R = 1\mathrm{M\Omega}$, figure 4.5 (a) and the resistor of $R = 79\,\mathrm{M\Omega}$ figure 4.5 (b). The displacement of the sprung mass with respect to the base $z(t)$ is shown as a red line over $4T$, where $T = 1/f$ is the excitation period. The associated capacitor charge $q(t)$, shown as a blue line, reaches a maximum of $q_{max} \approx 6\,\mathrm{nC}$. Contact occurs when the displacement (red line) drops below the green line demarcating the undeformed thickness of the PDMS layer $h$.

Table 4.1: List of the parameters used to numerically obtain frequency response curve of TENG.

| Parameter | symbol (unit) | value |
|---|---|---|
| Mass | m (kg) | 0.110 |
| Linear damping coefficient | $c_1$ (N.s/m) | 2.04 |
| Nonlinear (contact) damping coefficient | $c_2$ (N.s/m) | 10 |
| Effective stiffness of the springs | $k_1$ (N/m) | 159 |
| Linear stiffness of PDMS | $k_2$ (N/m) | 6700 |
| Stiffness of fully compressed PDMS | $k_3$ (N/m) | 41760 |
| Gap between PDMS and top electrode | $h_s$ (mm) | 3.85 |
| Permittivity of air | $\epsilon_0$ ($F.m^{-1}$) | 8.85 x $10^{-12}$ |
| Area of PDMS | A ($cm^2$) | 30 |
| Relative permittivity of PDMS | $\epsilon_r$ | 2.35 |
| Thickness of PDMS | h (µm ) | 420 |
| Surface charge density | $\sigma$ (µC/$m^2$ ) | 2.15 |
| Resistor | R (Ω ) | 79 x $10^6$ |

The penetration depth of the sprung mass into the PDMS layer is $h - z = 100$ µm. This is the lowest point in the mass travel downward, beyond which it reverses direction. The capacitor charge reaches a value of $q(t) \approxeq 0$ during contact for a resistive load of $R = 1\,\mathrm{M\Omega}$, figure 4.5 (a). However, the charge reaches a minimum value of $q(t) \approxeq 2.2\,\mathrm{nC}$ for a resistive load of $R = 79\,\mathrm{M\Omega}$. The phase delay of the charge with respect to displacement is negligible for $R = 1\,\mathrm{M\Omega}$. It increases with $R$ in proportion to discharge circuit time constant $\tau = RC$ and reaches $\phi = 0.3°$, figure 4.5(b), for a resistive load of $R = 79\,\mathrm{M\Omega}$.

The capacitor charge $q(t)$ settles to a maximum value over an extended interval centered around maximum separation for both value of resistors, which indicates that all electrons created during contact were swept from bottom electrode to top electrode. This also indicates that the interval within the harvesting cycle where displacement is in that range

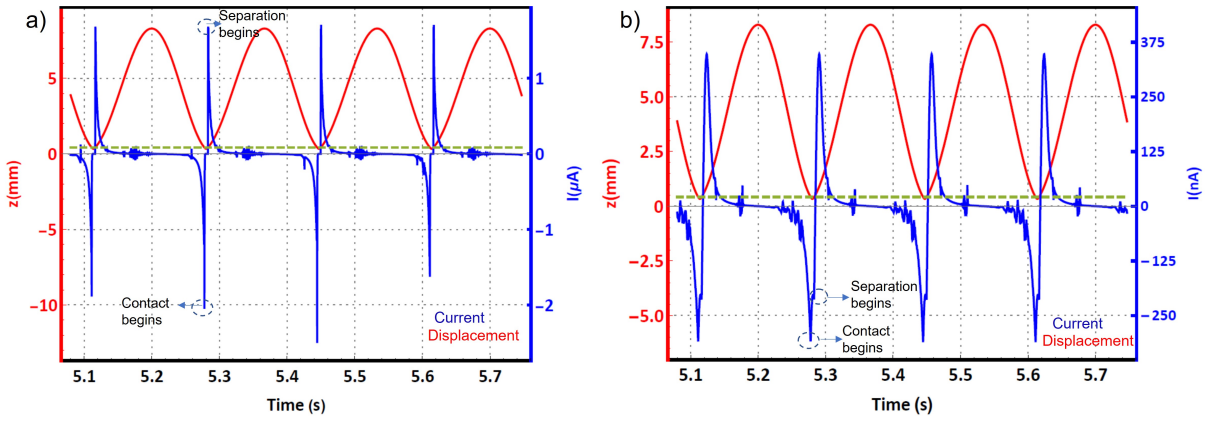


Figure 4.6: The simulated relative displacement $z(t)$ (red line) of the sprung mass and current $\dot{q}(t)$ (blue line) through (a) a resistor $R = 1\,\mathrm{M\Omega}$ and (b) a resistor $R = 79\,\mathrm{M\Omega}$, over 4 excitation periods under a base acceleration with an amplitude and frequency of $a_\circ = 0.3\,\mathrm{g}$ and $f = 6\,\mathrm{Hz}$.

($z(t) \leq 6\,\mathrm{mm}$) of negligible value to energy harvesting. Further work should be directed and finding ways to minimize this interval without compromising the overall performance of the TENG.

The simulated current $\dot{q}(t)$ through the harvesting resistors was evaluated as the derivative of the charge with respect to time. It is shown in figure 4.6 as a blue line in conjunction with the mass displacement (red line). The peak-to-peak current was found to be $\dot{q}_{pp} \approx 3.7$ μA for a resistive load of $R = 1\,\mathrm{M\Omega}$. It appears over a short interval centered around contact as shown in figure 4.6(a). The peak-to-peak current was found to be $\dot{q}_{pp} \approx 700$ nA for a resistive load of $R = 79\,\mathrm{M\Omega}$ as shown figure 4.6(b). The negative current peak appears during contact while the positive peak appears during the separation. Separation beginning point of the parallel plates might differ because of the time delay resulted from a resistive load of $R = 79\,\mathrm{M\Omega}$, as shown in figure 4.6.

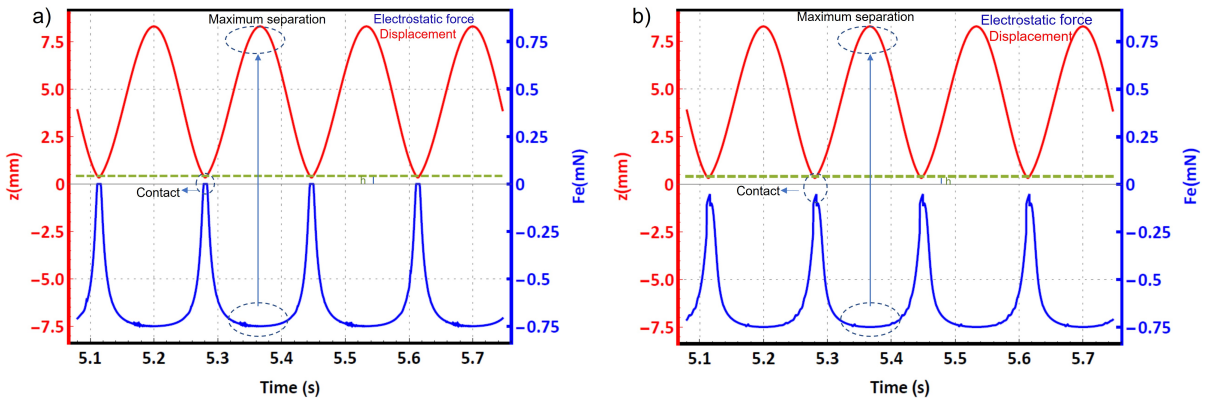


Figure 4.7: The simulated relative displacement $z(t)$ (red line) of the sprung mass and electrostatic force $F_e$(blue line), through the resistor $R = 1\,\mathrm{M\Omega}$ (a), and the resistor $R = 79\,\mathrm{M\Omega}$ (b), over 4 excitation periods under a base acceleration with an amplitude and frequency of $a_\circ = 0.3\,\mathrm{g}$ and $f = 6\,\mathrm{Hz}$.

The model was also used to investigate the relationship between the electrostatic force $F_e$ and displacement of the sprung mass $z(t)$. The results are shown in figure 4.7. The maximum electrostatic force (blue line) between the capacitor plates (red line) $F_e \approx 0.75\,\mathrm{mN}$ occurs during separation over an interval centered around maximum separation for $R = 1\,\mathrm{M\Omega}$ and $R = 79\,\mathrm{M\Omega}$. Minimum electrostatic force occurs during contact at maximum penetration point for both resistors. It is noted that the electrostatic force does not drop to zero during the contact for larger resistive loads. For example, for a resistive load of $R = 79\,\mathrm{M\Omega}$, the electrostatic force drops to a minimum of $F_e \approx 0.75$ µN as shown in figure 4.7(b).

The frequency response curve of the TENG is important tool to maximize harvesting of waste mechanical energy from the environment. It was evaluated experimentally under a base acceleration with an amplitude of $a_\circ = 0.3\,g$ over the frequency range $\Omega = [4, 9]\,\mathrm{Hz}$ in increasing steps of 0.25 Hz. The resistive load was set to $R = 79\,\mathrm{M\Omega}$. The output RMS voltage of the TENG was measured using an oscilloscope at each step. It was also simulated

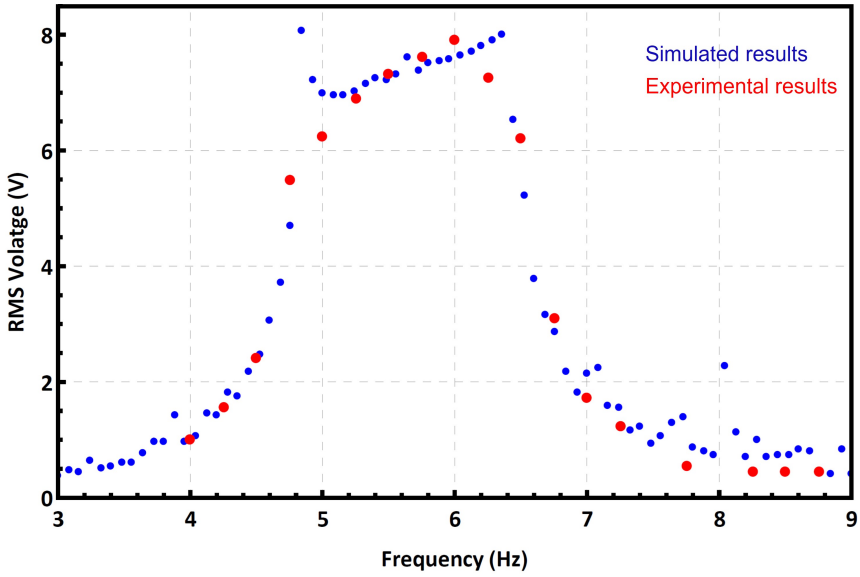


Figure 4.8: Comparison between the simulated and experimental frequency-response curves of the TENG under base acceleration excitation with an amplitude of $a_\circ = 0.3\,g$.

under same conditions except that frequency range was set to $\Omega = [3, 9]$ Hz and step to 0.1 Hz. The results obtained from the model (blue line) are compared to those obtained from the experiment (red line) in the figure 4.8. The results show that the model is in good agreement with experimental results. The TENG can harvest the mechanical energy over a wide and low-frequency range between 4.5 and 6.7 Hz. Maximum RMS voltage was found to be 8 V at approximately 6.4 Hz.

## 4.4 Experimental Methods

### 4.4.1 Fabrication of nano-structured films

The fabrication method employs a micro scale needle (scriber) mounted to a micro-resolution 3D stage (Prototype # 1) via a spring-damper suspension mechanism. As the needle traverses the polymeric substrate surface, non-uniformity in the morphology of the substrate surface and external vibrations (disturbances) generate time-variation in the magnitude and direction of the contact force, which in turn leads to needle tip vibrations. The spring-damper suspension mechanism acts to dissipate those vibrations and stabilizes the contact force, thereby generating uniform features in the substrate. An optical camera equipped with an 6× objective lens and 2× optical magnifier is attached to the stage to monitor the patterning process. Figure 4.9(a) shows the fabrication setup used to pattern the PMMA substrate.

The desired pattern and a constant contact force are defined in an interface software SonoGuide [77] which translates it into a 3D trajectory written in machine language. The controller of the micro-stage follows that trajectory as it traverses the needle tip over the substrate surface while tracking the process using the optical camera. Upon first contact, the of Z-axis actuator commands a displacement resulting in the tip penetrating the substrate surface with an average displacement of h(t).

The feature dimensions, width and depth, are controlled by varying the substrate tip contact force while feature length is commanded by the micro-stage set to desired value. The sharpness of the needle (scriber) tip, and the hardness of the substrate determine whether patterning results in plastic deformations or chip removal processes. In this case, the contact force and the needle tip orientation with respect to the trajectory were cali-

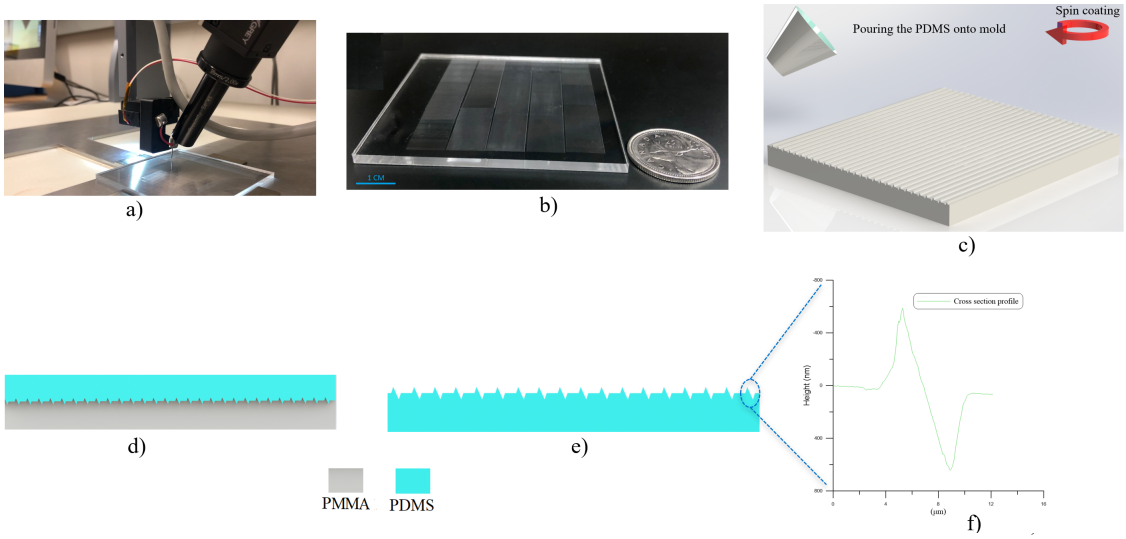


Figure 4.9: Optical image of experimental setup showing spring and damper assisted patterning process on a PMMA substrate (a). Six thousand array for both NGs and NTPs fabricated on the substrate in the area of 6 $\times$ 5 cm$^2$ (b). PDMS spin coating onto the substrate mold to transfer those features (c). Curing process for the coated PDMS (d). Peeling-off PDMS from the mold (e). The cross section profile shows small part of NGs and NTPs transferred to PDMS (f).

brated to only plastically deform the PMMA substrate. As the deformation created NGs in the surface, the material flowing out of them created NTPs on their edges resulting in the simultaneous creation of two nano features in a single patterning event. The dual nano features increase the effective surface contact area, thus enhancing triboelectricity. The patterned PMMA substrate, shown in figure 4.9(b), exhibiting an array of 6,000 and one centimeter long NGs and NTPs, is then used as a mold to cast PDMS films.

The PDMS base and its curing agent are mixed at a weight ratio of 5:1 and spin coated on the PMMA mold, figure 4.9(c). The mold and cast PDMS, figure 4.9(d), are placed for 5 minutes on a hot-plate for curing at 80° C. Multiple spin coating and curing cycles are undertaken to reach a thickness of 420 µm. The PDMS film is then peeled off from the mold and surface patterns are shown schematically in figure 4.9(e). After the peeling it off, reversal structures are observed on the PDMS as expected. The surface topography of the fabricated PDMS film was measured using an atomic force microscope (Bruker AFM). Figure 4.9(f) shows the cross-sectional profile of the NG and NTP on the fabricated PDMS film. The bases of the NGs and NTPs were was measured to be 2.5 µm wide and their apexes were measured to be 600 nm high.

### 4.4.2 Fabrication of TENGs

The TENG consists of structural support elements and triboelectric harvesting elements. The former includes two backbone PMMA plates, $8 \times 8\,\mathrm{cm}^2$ in area and 0.87 cm in thickness, to provide structural support and an an inertial energy to harvesting mass. Four linear guides, 60 mm long and 3.2 mm in diameter steel rods, are placed at the four corners of the plates to maintain alignment between the plates as they oscillate against each other under host vibrations. Four concentric steel springs, 24 mm long with outer diameter of 4.8 mm,

inner diameter of 4.5 mm, and equivalent spring stiffness of 159 N/m, are housed around the linear guides to maintain separation between the plates. A $6 \times 5\,\mathrm{cm}^2$ PMMA stage is attached to the bottom backbone plate using double-sided tape to control the capacitive gap. The harvesting elements are the PDMS film and two Al foil films, all with identical planar dimensions to the stage.

### 4.4.3 Setup and characterization

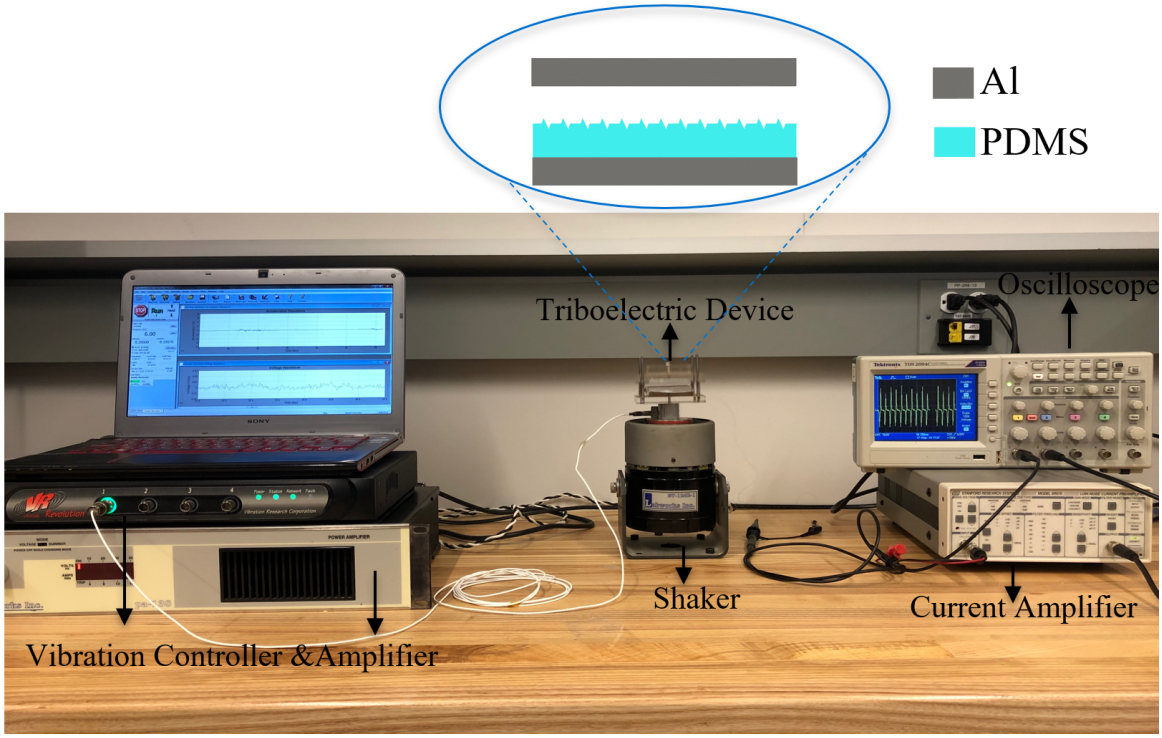


Figure 4.10: Experimental setup for the TENG.

Surface topography pictures of the fabricated mold and PDMS film are produced using an optical microscope and atomic force microscopy (Nikon Inverted Microscope, and Bruker

AFM respectively). Shaker is excited by an amplifier (LABWORKS pa-138) and it is controlled by a vibration controller (VR9500 Revolution) by receiving a feedback from an accelerometer attached to the shaker. The output voltage of the TENG is measured by using a Oscilloscope (Tektronix-TDS2004C) with a probe input impedance of $R = 79\,\mathrm{M}\Omega$. Lastly, the short-circuit current of the TENG is measured using a low noise current amplifier (SRS Stanford Research Systems-SR570 Pre-amplifier). An image of experimental setup for TENG is shown in the figure 4.10.

## 4.5 Results and Discussions

Conventional low-cost fabrication methods are not applicable to produce features less than 50 µm, which disables further improvement in effective contact area, in turn, output power of TENGs. However, d-SPL fabrication method provides high resolution in surface patterning, thereby introducing a larger number of nano and micro features in a given area. The method is deployed to pattern centimeter long nano features including nano grooves and nano triangle prisms on PMMA substrate. When the sharp tip patterns the surface of PMMA, the deformation creates NGs in the surface, the material flowing out of them creates NTPs on their edges resulting in the simultaneous creation of two nano features in a single patterning event. The dual nano features increase the effective surface contact area. Figure 4.11(a) shows optical microscope images of uniformly patterned 2.5 µm wide and 600 nm deep and 1 cm long pairs of NGs and NTPs. The area shown, $4 \times 3$ mm$^2$, exhibits 85 pairs of NGs and NTPs. A close-up view of the patterns in an $0.75 \times 0.565\,\mathrm{mm}^2$ area of is shown in Figure 4.11(b), and an AFM image of the plastically deformed NGs and flown NTPs, in the area of $15 \times 15$ µm$^2$ is shown in Figure 4.11(c). The AFM image distinctly illustrates the both nano groove and plastically deformed material flow (nano

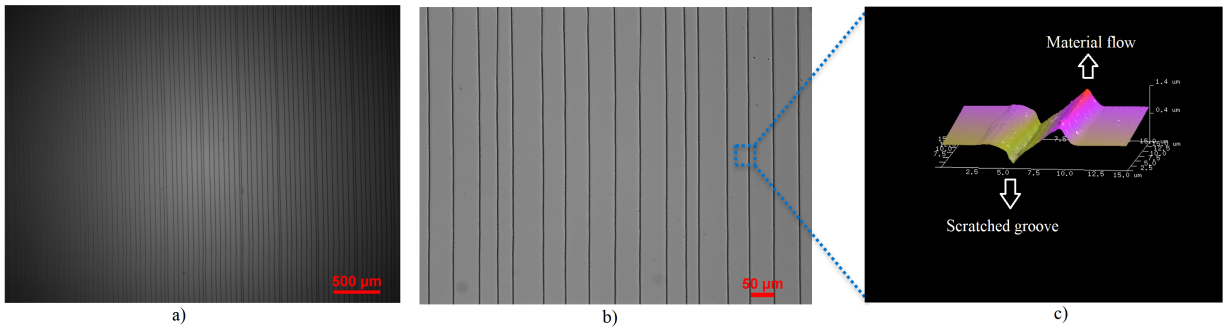


Figure 4.11: (a) A microscopic image of an array made of 85 pairs of NGs and NTPs in a $4 \times 3\,\mathrm{mm}^2$ area. (b) A close-up microscopic image of a $750 \times 565\,\mu\mathrm{m}^2$ area. (c) AFM image of the NGs and NTPs in a $0.75 \times 0.565\,\mathrm{mm}^2$ area illustrating plastic deformation and material flow.

triangular prism) on the edge of groove.

Increase in contact area due to the nano structures crated via the d-SPL method cannot be produced by conventional rapid fabrication methods. For instance, $CO_2$ laser engraving method can produce maximum fifteen microchannels in the area of $4 \times 3$ mm$^2$ (channel length: 4mm), and considering resolution of the laser and spacing between channels is 100 µm. Thus, further increase in contact area is limited to the resolution of laser engraving method. However, the d-SPL improves the number of the structures produced on the mold in the order of two magnitudes more than the laser engraving. The d-SPL method is also capable of producing the nano structures, thereby significantly increasing the number of fabricated structures in a given area.

The figure 4.12(a) and (b) shows flat and nano structured PMMA molds that are used to cast and to obtain flat and nano structured PDMS. Nano structured PMMA mold via d-SPL method includes six thousands of 2.5 µm wide, 600 nm deep, and 1 cm long NGs and exact same amount of NTPs structures on it. Figure 4.12(c) shows a optical image of

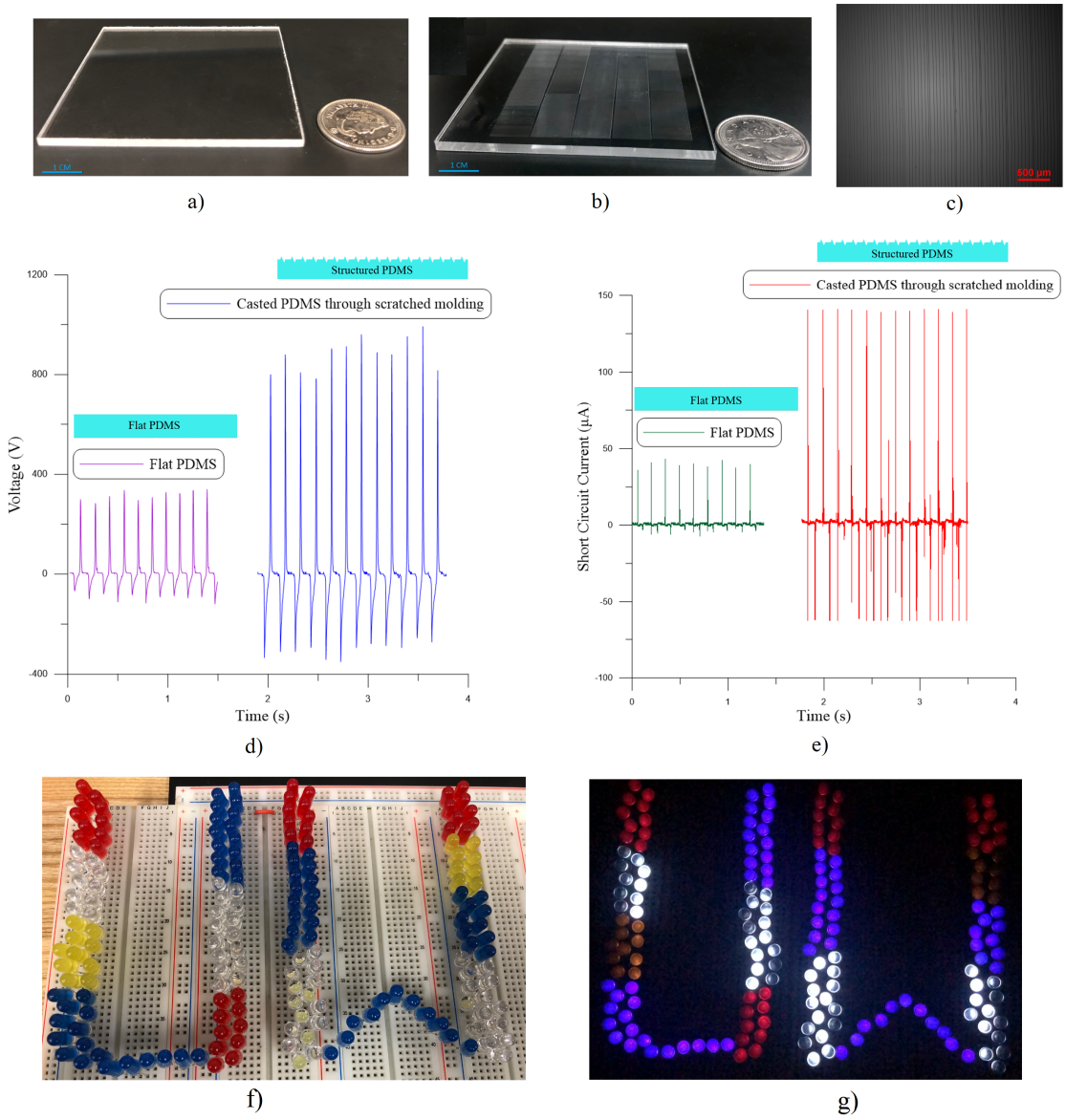


Figure 4.12: (a) Image of flat PMMA mold. (b) Image of nano structured PMMA mold including six thousands of one centimeter long NGs and NTPs. (c) Optical microscope image of the patterned mold. (d) Output voltage of flat PDMS and structured PDMS. (e) Output of short circuit current for flat and nano structured PDMS. (f) Different color LEDs connected in series when TENG is off. (g) Image of LEDs when when TENG is on.

structured patterns for the area of 4 × 3 $mm^2$.

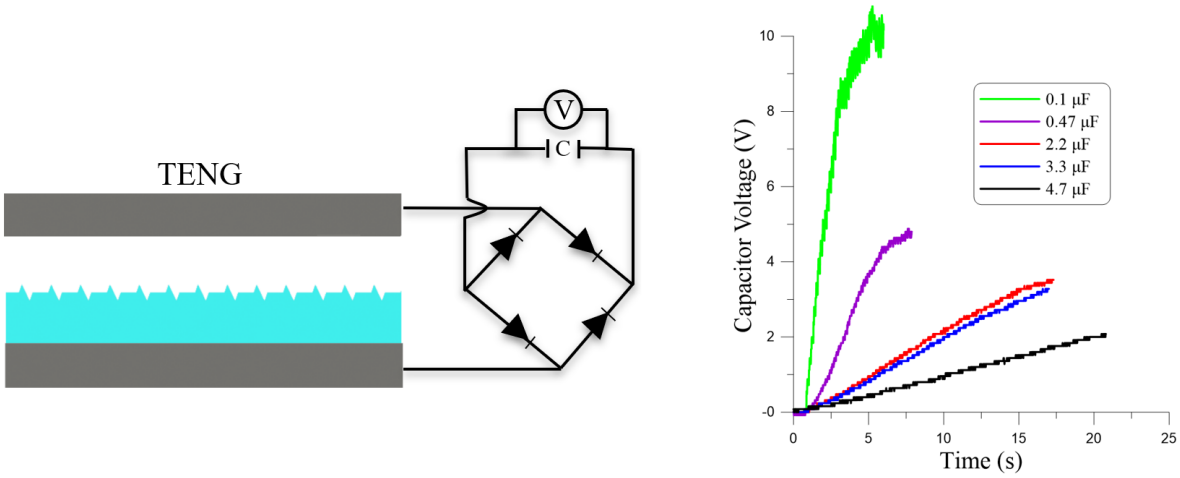


Figure 4.13: Charging the different size of capacitors directly connected to output of TENG employing nano structured PDMS.

PDMS including twelve thousands nano structures in total have been utilized as negative triboelectric material and compared to flat PDMS with under the same conditions. It is found that nano structured PDMS significantly improves output power of TENGs. The figure 4.12(d) depicts a comparison between output voltage of the TENGs deploying structured and flat surface PDMS using $R = 79\,M\Omega$ input impedance oscilloscope probe. TENGs using the structured PDMS produces 1200 voltage peak-to-peak while it remains 400 voltage peak-to-peak for flat PDMS. Also, figure 4.12(e) presents AC short circuit current comparison between TENGs employing nano structured and flat PDMS. AC current generated by TENGs employing the structured PDMS is measured to be 200 µA peak-to-peak while it is only 40 µA peak-to-peak for flat PDMS.

Uniformly and low costly fabricated NGs and NTPs on the PDMS increases effective total contact area of the TENGs, thereby improving the output power. Also, NTPs are

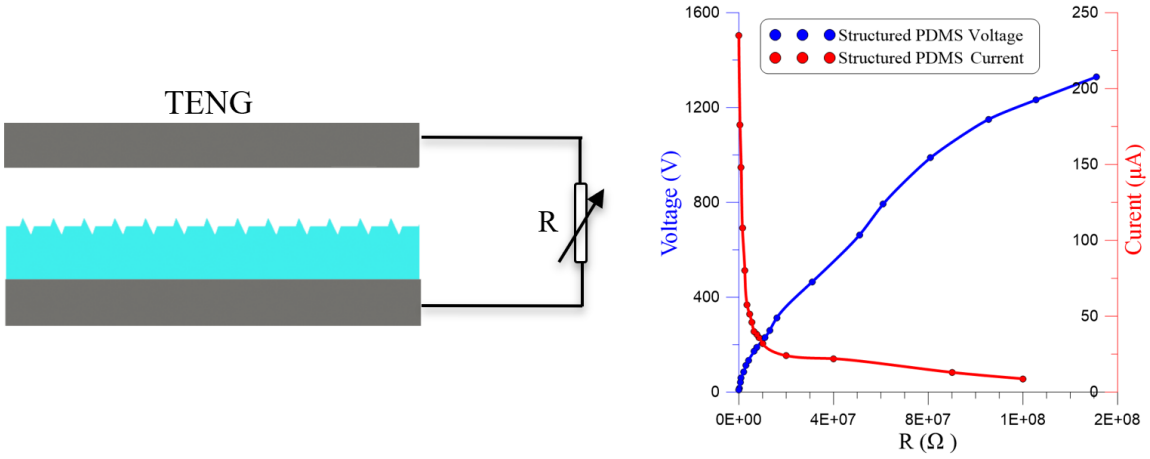


Figure 4.14: Output voltage and current response of TENG employing nano structured PDMS across a variable resistor.

bending during contact, which leads to sliding friction between PDMS and Al film. The friction force removes extra electrons on Al, which results in generation of more charges transferred to PDMS, therefore enabling further enhancement in output power of TENG.

A bridge rectifier consisting of four diodes are employed to output of TENG for conversion of alternating current (AC) to direct current (DC), then its output is connected to one hundred eighty different color LEDs in series. The figure 4.12(f) and (g) demonstrates images of LEDs when TENGs is off and on respectively. TENGs with NTPs and NGs can directly lit up a hundred eighty different color LEDs without charging a capacitor. However, TENGs with flat PDMS can only lit up sixty seven LEDs. Also, after the rectifying output of the TENG, output voltage of different size of capacitors ranging from 0.1 µF to 4.7 µF was measured. A schematic for charging the capacitor and experimental results of its output voltage versus time are shown in the figure 4.13.

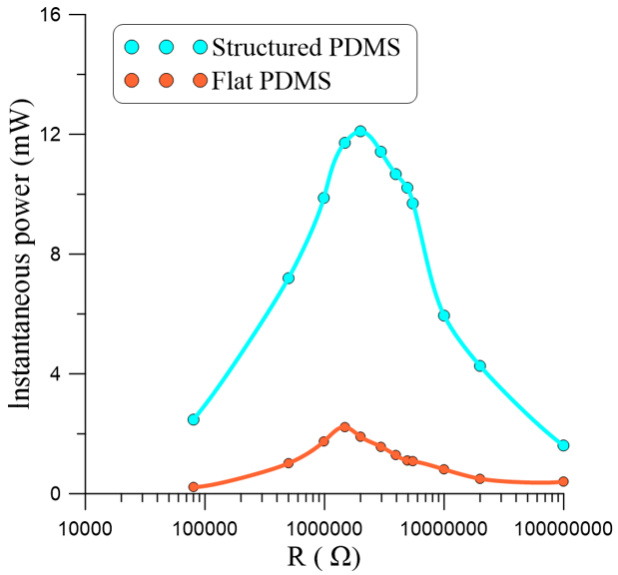


Figure 4.15: An output power comparison between flat and structured PDMS.

Voltage and current outputs of TENGs across a variable resistor are also measured and shown in the figure 4.14. The maximum voltage is measured to be 1350 voltage peak-to-peak through a resistive load of $R = 150\,\mathrm{M}\Omega$ and short circuit current is measured to be 220 µA peak-to-peak through a resistive load of $R = 50\,\Omega$.

Output power of the TENGs across a resistor is shown in the figure 4.15. Results show enhancement in the output power of TENG employing nano structured PDMS compared to TENG employing the flat PDMS. Instantaneous output power of the TENG employing flat PDMS is maximum of 2.2 mW at a resistive load of $R = 1.5\,\mathrm{M}\Omega$. The output power of TENG employing nano structured PDMS reaches to maximum of 12.2 mW at a resistive load of $R = 1.5\,\mathrm{M}\Omega$. The power is increased six fold by introducing the NTPs and NGs on its surface.

## 4.6 Summary

A coupled electromechanical model was developed to better understand fundamental behavior of the triboelectric energy harvesters. Then the model was deployed to design wide and low-frequency energy harvester prototypes to be able to harvest the most of free mechanical vibrations in the environment less than 10 Hz. The proposed prototype TENG can harvest the maximum mechanical energy in range between 4 and 7 Hz under base excitation with an amplitude of $a_\circ = 0.3\,\mathrm{g}$. Harvested maximum RMS voltage was found to be 8 V at the frequency of 6.5 Hz.

The d-SPL method has been also successfully deployed for rapid and low-cost surface modification of the triboelectric films. Nano Grooves and nano triangular prisms were created on the negative triboelectric film to increase the effective contact area, thereby enhancing the output power of the TENGs. We showed that the output power of the nanostructured TENG using the d-SPL method is significantly more than that of a TENG using a flat PDMS, at 12.2 mW compared to 2.2 mW, under the same operating conditions.

# Chapter 5

# Nanoscale Circuits

In this chapter, demonstration of the d-SPL for fabrication of nanoscale thin circuits is demonstrated. First, d-SPL method was used to fabricate conductive electrodes on the flexible and rigid substrates. Then, the d-SPL method was deployed to demonstrate for fabrication of back-gated graphene field effect transistors.

## 5.1 Introduction

Patterning of nanoscale thin metal films has attracted tremendous attention due to their potential use in fabrication of field effect transistors (FETs) [118]. Various fabrication methods have been employed in fabrication of FETs including standard lithography and inject printing [119]. Lithographic methods achieve high resolution using mask processes, but they are complicated and expensive [36]. Inject printing methods reduce the complexity and cost of fabrication but their resolution still needs improvement to increase the FETs' mobility, and sensitivity for bio applications [120]. Conventional scanning probe

lithography methods succeeded in reducing costs and alleviated need for vacuum while enabling high resolution fabrication [65, 121, 122]. However, they are very slow, requiring a feedback mechanism and limited to very small surface patterning area. We demonstrate here, a novel, low-cost, benchtop, and direct metal surface patterning method that can operate over large areas with a high velocity of 1 mm/s. Using the second fabrication stage prototype #2, and positive patterning method described in chapter 3 was employed for the direct nanoscale thin metal film patterning process. First, patterning of the metal film on the polymeric based flexible substrate was demonstrated. Then nano metal thin films deposited on silicon wafer (rigid) was patterned into interdigitated electrodes forming source and drain of the transistor. Then graphene was deposited between source and drain to create the channel using a microplotter.

## 5.2 Fabrication

### 5.2.1 Circuits on flexible substrates

First, the bio-compatible and flexible Kapton film was placed on the silicon wafer providing structural support during the whole fabrication process. Then silver ($Ag^+$) nanoparticle ink with the viscosity of 24 cP is spin coated onto the Kapton film with 700 rpm to obtain homogeneously thin layer of the silver. Later, the thin silver ink is pre-sintered on a hotplate at 120 °C for 20 minutes to ensure its suitability and stability for the patterning process. Prototype #2 (custom built 3D nanostage) is then used with positive patterning method to fabricate desired pattern on the substrate. Nanoscale thin silver film is removed through chip removal process until complete isolation of the design electrodes standing on the substrate. A needle made of stainless steel was used for the patterning of the silver.

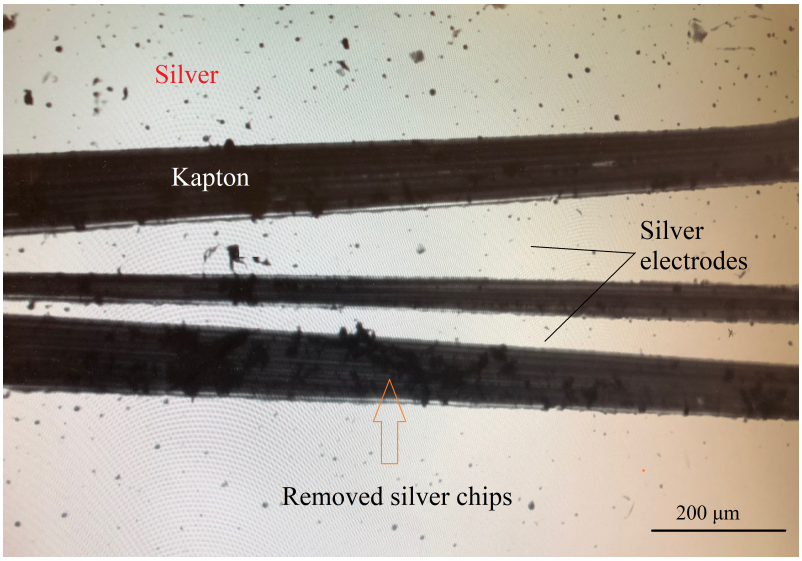


Figure 5.1: Electrodes fabricated on flexible substrate Kapton film.

Skipping a patterning step due to accuracy of the stages might result in failure of the fabrication process. Sintering is processed at 120 °C for 2 hours to have high conductivity for the patterned silver nanoparticle film.

Figure 5.1 shows fabricated silver electrodes on flexible and bio-compatible Kapton film. As it can be observed from the figure, the electrodes are completely isolated from bulk of silver by d-SPL method using positive patterning. Dark area in the figure corresponds the Kapton film surface as the white area is the silver film. Removed silver chips were also shown in the figure. Chips left on the device can be removed by applying compressed air.

### 5.2.2 Circuits on rigid substrates

Nanoscale thin silver film on silicon wafer was directly patterned using the second fabrication stage prototype #2 and positive patterning.

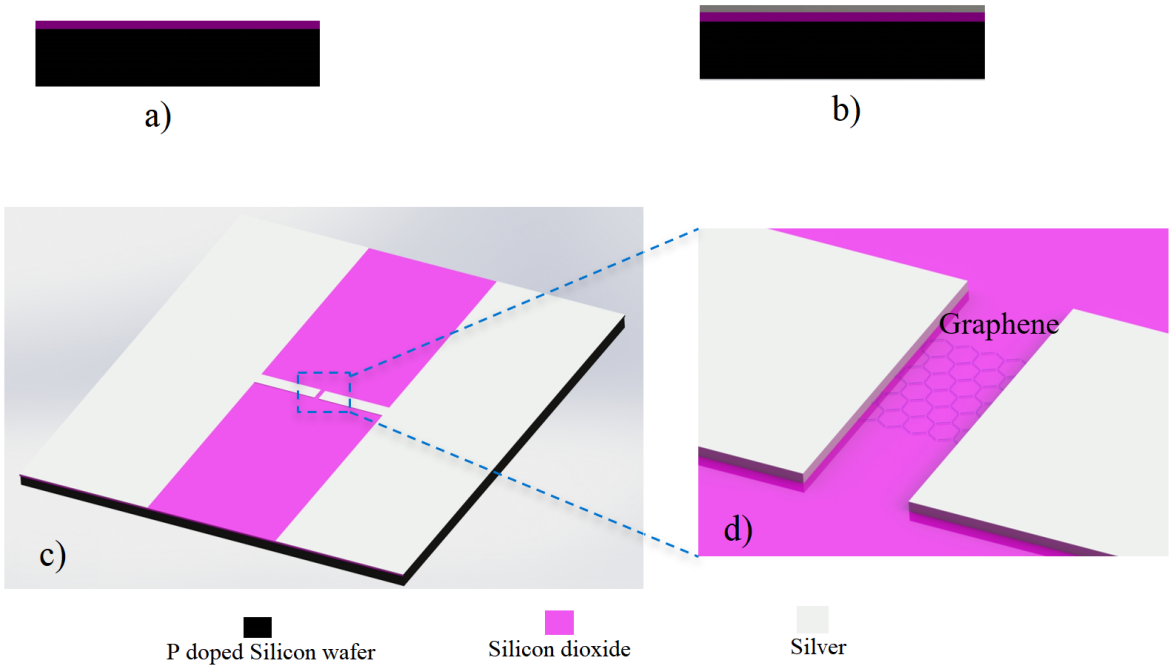


Figure 5.2: Fabrication flow process of back-gated graphene FET. (a) Commercially available substrate: $P^+$ doped silicon wafer has oxidation layer on its top. (b) Silver coating on the substrate using the sputtering. (c) Removing the silver and leaving the conductive parts of interest. (d) A drop cast of the graphene placed between source and drain.

Fabrication process flow for FET is shown in Figure 5.2. Commercially available $p^+$ doped silicon wafer with 285 nm thick $SiO_2$ layer is supplied and used as a substrate. It was then coated with 120 nm thick silver layer using the sputtering. The silver layer was patterned into interdigitated electrodes that form the source and drain of the FET using blood draw needle (stainless steel scriber). During the real time fabrication, optical image of the interdigitated electrode and its pad was obtained using the an optical camera monitoring the process, and it is depicted in the figure 5.3.

To complete the fabrication of back-gated graphene field effect transistors, deposition

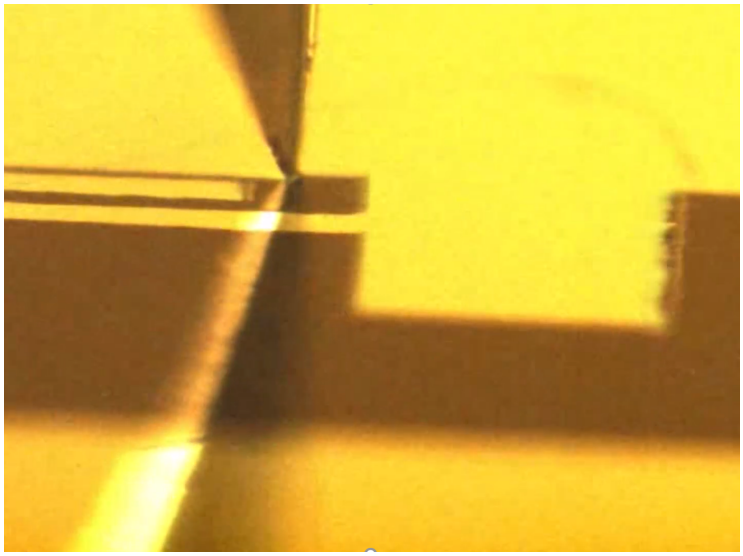

Figure 5.3: Optical image taken during real time fabrication process of interdigitated electrodes.

of the graphene between source and drain is a necessary step. The standard resolution of the prototype #1 is 5 µm along the z-axis and 25 µm for the two in-plane axes. While the planar resolution of the microplotter is adequate for deposition purposes, its vertical (z-axis) resolution is inadequate to prevent the tip and device failure. Placement errors along the z-axis can crash the pipette tip into interdigitated electrode. Therefore, the nanostage was integrated with the microplotter to improve the z-axis resolution. A hierarchical approach is adopted for z-axis positioning. It uses the microplotter for coarse positioning and the nanostage for fine positioning. The nanostage is driven by a DFRobot quad DC motor shield and it is controlled by a Teensy 4.0 development board.

An ethylene glycol-graphene mixture was deposited between the source and drain using the first fabrication stage prototype #1 (microplotter) to form the channel and allowed to dry naturally. First, graphene powder is mixed with ethylene glycol at weight ratio

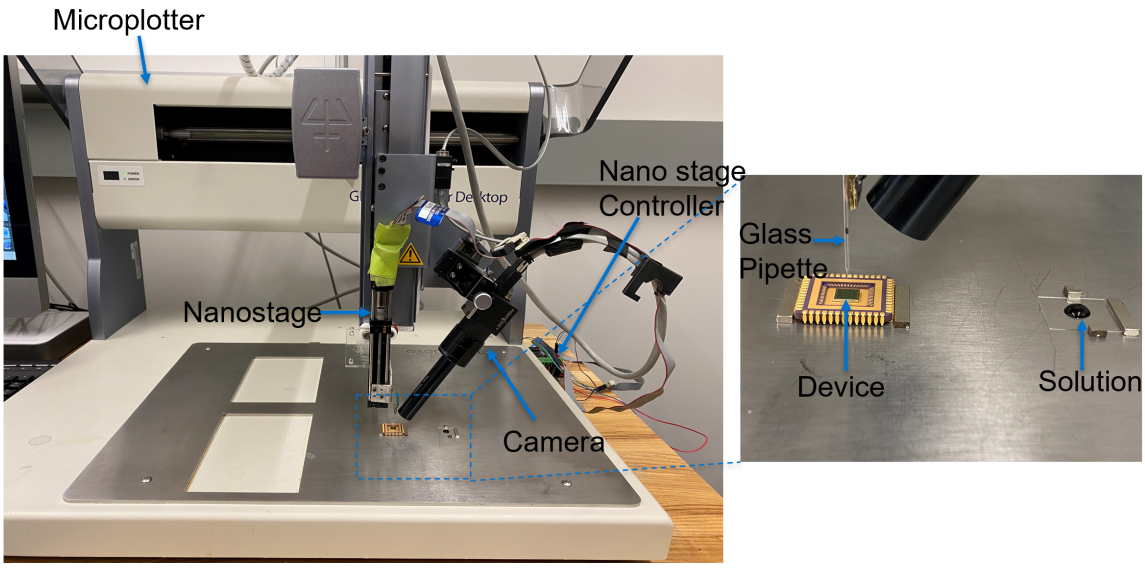


Figure 5.4: Deposition setup employed for transfer of the graphene between source and drain electrodes to create channel.

of 1:10. A drop of the mixture was placed on the glass with syringe pipette to form the solution well. The camera is equipped with a 6X lens and a 2X optical amplifier to enhance visualization. The camera is focused on the glass pipette which has diamter of 30 µm. Position of the source and drain interdigitated electrode and solution well are obtained and saved in the memory of the microplotter controller before the deposition process. Deposition commences with microplotter bringing the tip of the pipette into the well, thereby driving the solution into the pipette through capillary force. The pipette is then commanded to a pre-saved target positions in the vicinity of the interdigitated electrodes where it comes to stop without the tip coming into contact with surface. The nanostage controller takes charge of commanding the fine positioning steps until the tip reaches its target. After contacting the surface of the interdigitated electrode, the solution is released via surface tension. This process is repeated multiple times to reach desired

deposition of graphene between the electrodes. A typical picture of the deposition setup is shown in figure 5.4.

## 5.3 Characterization

First, the fabricated interdigitated electrode was optically inspected and a microscope image of the fabricated interdigitated electrode is shown in the figure 5.5.

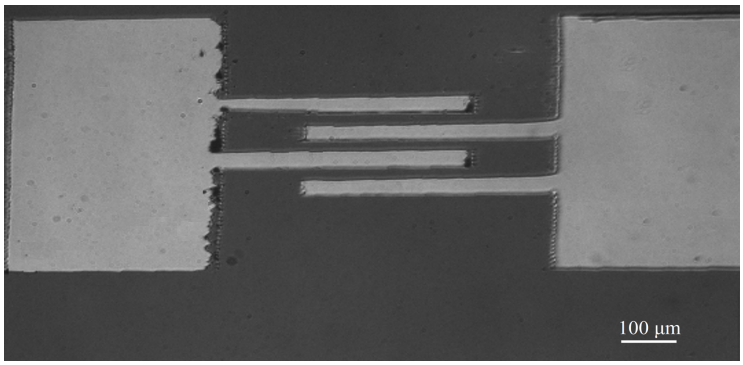


Figure 5.5: An optical image of the interdigitated electrode forming source and drain.

Also an optical surface profiler was used to measure surface topography of the fabricated interdigitated electrodes and demonstrated in the figure 5.6. Thickness of the silver interdigitated electrodes was found to be approximately 120 nm. After the deposition of the graphene, Keysight b2902a Source Measure Unit (SMU) was implemented to obtain IV characteristics of the fabricated FET using the Quick IV measurement software. A schematic of the experimental characterization setup of the back-gated graphene FET was demonstrated in the figure 5.7. Two probes are landed to pads of the interdigitated electrodes and they are deployed as source and drain terminals of the FET. $P^+$ doped silicon wafer was deployed as back gate of the FET. A constant DC current applied to the drain

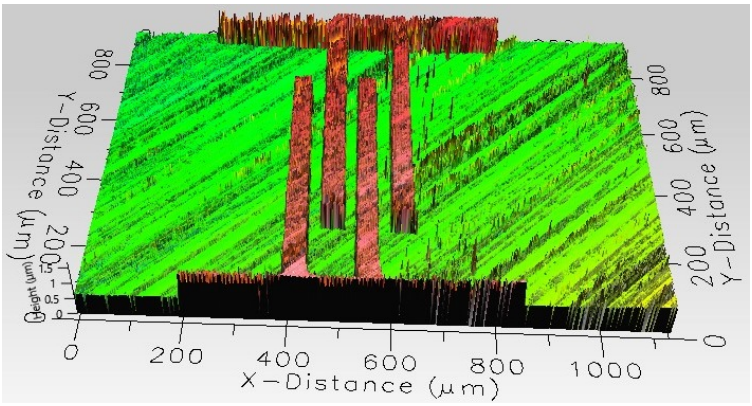


Figure 5.6: Optical profiler image of the fabricated interdigitated electrode using the d-SPL.

while gate voltage was swept. Current flowing from source to drain was then measured using the SMU.

## 5.4 Results and Discussion

Using d-SPL method, direct patterning of the silver on Kapton film was successfully demonstrated. Discontinuous chip removal process of the silver was observed during the whole process. Since stainless steel tip is much harder than Kapton film, there was also patterning occurred on the Kapton film. As the thickness of silver coated on the Kapton film increases, more chips are required to remove for isolation of the electrodes. This might cause complexity in surface-contact force and position of the tip, thereby leading to nonuniform surface patterning. Resolution of the patterning depends on two criteria: tip-substrate contact force and tip size of the scriber tool.

Moreover, the source and drain fabrication of back-gated graphene FET were achieved

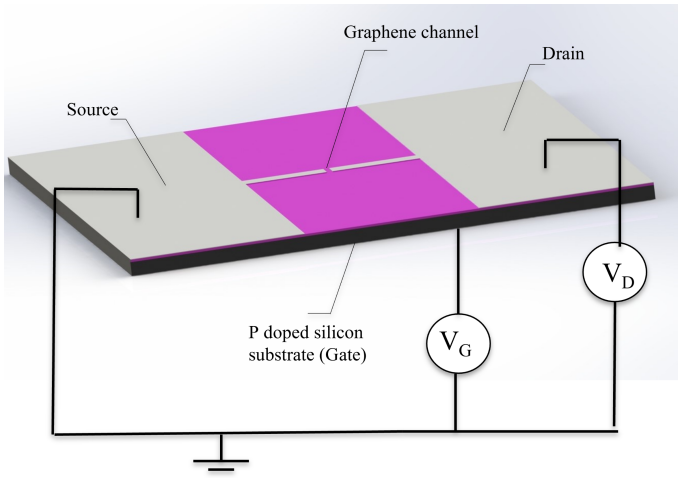


Figure 5.7: A schematic for characterization setup of the back-gated graphene FET.

in a 120 nm silver layer exhibiting a channel length of 20 µm via d-SPL. Interdigitated electrodes and deposition of the graphene was demonstrated in the figure 5.8. Five different DC voltage values ranging from 0 to 0.28 V was applied to drain terminal of the FET while sweeping the gate voltage from -1 to 1 V. Drain-source current measurement was found to be increasing between 0 and -1 V gate voltage as it is vice versa between 0 and 1 V.

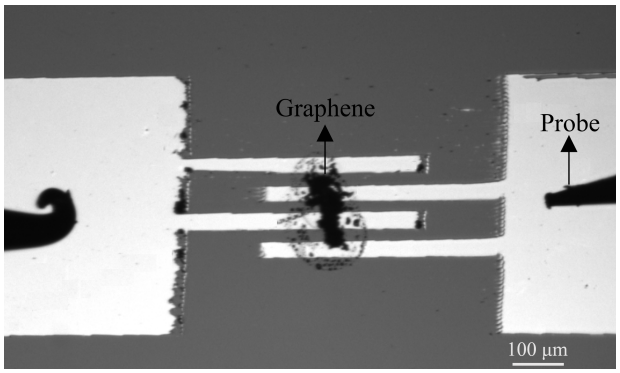


Figure 5.8: An microscope image of the deposited graphene between interdigitated electrodes.

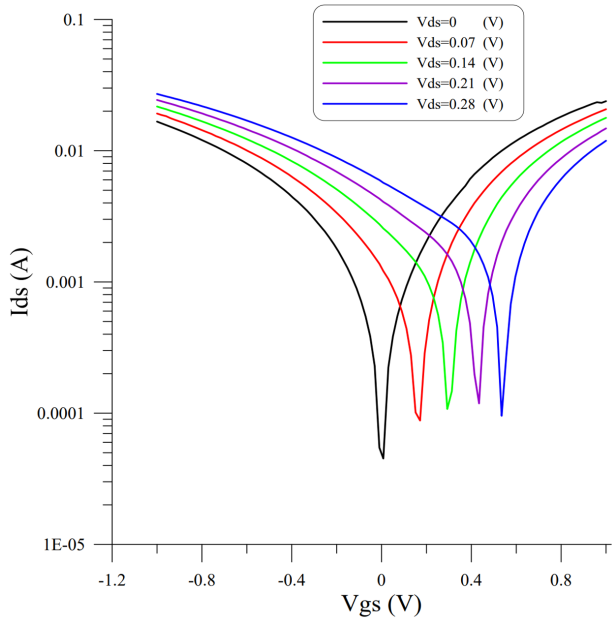


Figure 5.9: Characteristic I-V curves of the transistor for five values of the drain-source voltage difference Vds.

Experimental results of the back-gated graphene FET fabricated via d-SPL was demonstrated in the figure 5.9. The IV curves of the fabricated FETs show high carrier mobility and $I_{on}/I_{off}$ ratio on the order of $10^3$. Drain-source (Ids) current was found to be between 16 mA and 30 mA which shows that equivalent resistance including contact resistance between graphene and interdigitated electrodes (source-drain), and graphene channel resistance is very low.

Deposition of the graphene using the microplotter is found to be promising since the graphene deposition comes as a final step in fabrication flow process. However, fabrication step of graphene FET using conventional lithographic methods comes before the deposition of the source and drain electrodes, thereby graphene is exposed to other deposition

steps and it might cause an increase in contact resistance between the graphene and the electrodes. This problem was vanished by deposition of the graphene as a final step.

## 5.5 Summary

Direct patterning of nanoscale thin silver films on flexible and rigid substrates was successfully demonstrated via implementation of the d-SPL method. The d-SPL enabled uniform, direct and rapid metal patterning with a velocity of 1 mm/s which is two orders of magnitude faster than conventional scanning probe lithography methods. Complex structures like interdigitated electrodes with 10 µm spacing could be straightforwardly fabricated via d-SPL without use of expensive equipment in cleanroom. Deposition of the graphene between source and drain interdigitated electrodes was also successfully demonstrated to create the channel. Deposition of the graphene using the microplotter is found to be promising since the graphene deposition comes as a final step in fabrication flow process, thus not exposing it to prefabrication steps, which in turn, minimizes oxidation of the graphene during the fabrication of FET. Back-gated graphene FET fabricated via d-SPL shows high carrier mobility and $I_{on}/I_{off}$ ratio on the order of $10^3$.

# Chapter 6

# Conclusions and Future Work

## 6.1 Conclusions

We introduced dynamic Scanning Probe Lithography (d-SPL). A novel, low-cost, rapid, and benchtop fabrication method that does not require vacuum while offering unique features:

- Micro to nano scale thickness resolution with potential for angstrom scale.
- Centimeter long uniform patterning in seconds.
- Applicability to a wide range of materials.
- High throughput.

This method owes its distinctive abilities to a spring-damper suspension connecting a sharp scriber tip to a programmable 3D nano-resolution stage. The suspension mechanism enables the scriber to move up and down, thereby creating an adaptive working distance

without a need for complicated feedback systems. It compensates for variations in surface contact force, thus produces long and uniform surface patterns.

Using the d-SPL method, micro and nano wires can be fabricated through a continuous chip removal process. Some of these wires were observed to stand as suspended beams and were characterized under the thermal noise excitation. Their frequency response was measured using the LDV. It was experimentally found that these wires have a quality factor of 50. To fundamentally understand the d-SPL method, an analytical model was developed to investigate the operating principle and its limitations. It was found that chatter develops as patterning speed and cut width increase. The model was validated through experiments. In the process, micro-scale chatter was observed in patterning for the first time.

The d-SPL method was deployed for rapid and uniform surface modification of the triboelectric films. Nano Grooves (NGs) and nano triangular prisms (NTPs) were created on a negative triboelectric film to increase the effective contact area, thereby enhance the output power of the TENGs. We showed that the output power of TENGs nano structured using d-SPL is significantly more than that of a TENG using flat PDMS, at 12.2 mW compared to 2.2 mW.

To better understand behavior of triboelectric energy harvesters, a coupled analytical electromechanical model was developed. The model was deployed to design and build low-frequency and wide-band energy harvesters that can harvest environmental vibrations at frequencies below 10 Hz. We experimentally showed that the proposed TENG prototypes can harvest the energy in a wide and low-frequency range between 4 and 7 Hz. The maximum RMS voltage was found to be 8 V at 0.3 g and 6.5 Hz. The model was validated by comparing those experimental results to its predictions.

Direct patterning of nanoscale thin silver films on flexible and rigid substrates was successfully demonstrated via the d-SPL method. It enabled direct and rapid patterning of uniform metal features with a velocity of 1 mm/s which is at least two orders-of-magnitude faster than conventional scanning probe lithography methods. Interdigitated electrodes with 10 µm spacing were straightforwardly fabricated without use of expensive equipment or cleanroom.

Deposition of graphene between a source and a drain made of these interdigitated electrodes was successfully demonstrated, thereby creating the channel for a nano scale FET. Deposition of graphene using a microplotter was found to be a promising method for FET fabrication since it does not expose the channel graphene to subsequent fabrication steps. The back-gated graphene FET fabricated via d-SPL method shows high carrier mobility and an $I_{on}/I_{off}$ ratio on the order of $10^3$.

## 6.2 Future Work

Continuation of this dissertation in future are summarized as follows:

- The d-SPL method can be employed for direct surface patterning and fabrication of back-gated field effect transistors on PCB substrates. This would enable direct fabrication of transistors on PCB and further scaling down of the circuits.
- Back-gated graphene field effect transistor can be implemented as bio and chemical sensors such as gas sensor. This step would require polymer functionalization and use of deposition method developed in this dissertation.
- Uniform and long micro and nano wires can be produced and they can be implemented as pressure sensors.

- Since the deposition of the graphene between source and drain electrodes comes as final step, contact resistance between graphene and source-drain electrodes can be further studied to understand how mobility of the transistor changes with this fabrication method.

- Analytical model developed for triboelectric energy harvesters will be further studied to gain a deeper understanding of the system's behavior and its nonlinearity via investigating impacting and non-impacting branches of frequency response curve.

# References


[1] Andrea Jacassi, Francesco Tantussi, Michele Dipalo, Claudio Biagini, Nicolò MacCaferri, Angelo Bozzola, and Francesco De Angelis. Scanning Probe Photonic Nanojet Lithography. *ACS Applied Materials and Interfaces*, 9(37):32386–32393, 2017.

[2] James L Hedrick, Keith A Brown, Edward J Kluender, Maria D Cabezas, Peng-cheng Chen, Chad A Mirkin, Biological Engineering, United States, United States, United States, United States, Cummington Mall, and United States. Hard Transparent Arrays for Polymer Pen Lithography. *ACS Nano*, 10(3):3144–3148, 2017.

[3] Ricardo Garcia, Armin W Knoll, and Elisa Riedo. Advanced scanning probe lithography. *Nature nanotechnology*, 9(8):577–587, 2014.

[4] Lei Zhang, Hongtao Liu, Yan Zhao, Xiangnan Sun, Yugeng Wen, Yunlong Guo, Xike Gao, Chong An Di, Gui Yu, and Yunqi Liu. Inkjet printing high-resolution, large-area graphene patterns by coffee-ring lithography. *Advanced Materials*, 24(3):436–440, 2012.

[5] Jinxing Li, Wei Gao, Renfeng Dong, Allen Pei, Sirilak Sattayasamitsathit, and Joseph Wang. Nanomotor lithography. *Nature Communications*, 5:1–7, 2014.

[6] Allen Cowen, Busbee Hardy, Ramaswamy Mahadevan, and Steve Wilcenski. *PolyMUMPs Design Handbook*. MEMSCAP Inc., 2011.

[7] Anindya Lal, Hrishikesh Sarkar, Anupam Dutta, and Tarun Kanti. Sensors and Actuators A : Physical A high precision SOI MEMS – CMOS ± 4 g piezoresistive accelerometer. *Sensors and Actuators: A. Physical*, 210:77–85, 2014.

[8] Tim Scharnweber, Roman Truckenm, Andrea M Schneider, Alexander Welle, and Stefan Giselbrecht. Lab on a Chip Rapid prototyping of microstructures in polydimethylsiloxane ( PDMS ) by. *Lab on a Chip*, 11:1368–1371, 2011.

[9] Pieter F Moonen, Iryna Yakimets, and Jurriaan Huskens. Fabrication of Transistors on Flexible Substrates : from Mass-Printing to High-Resolution Alternative Lithography Strategies. *Advanced Materials*, pages 1–16, 2012.

[10] Shinji Okazaki. Resolution limits of optical lithography. *Journal of Vacuum Science & Technology B: Microelectronics and Nanometer Structures Processing, Measurement, and Phenomena*, 9(6):2829–2833, 1991.

[11] Siqi Ma, Celal Con, Mustafa Yavuz, and Bo Cui. Polystyrene negative resist for high-resolution electron beam lithography. *Nanoscale research letters*, 6(1):1–6, 2011.

[12] J Gierak, A Septier, and C Vieu. Design and realization of a very high-resolution fib nanofabrication instrument. *Nuclear Instruments and Methods in Physics Research Section A: Accelerators, Spectrometers, Detectors and Associated Equipment*, 427(1-2):91–98, 1999.

[13] Yang He, Yongda Yan, Yanquan Geng, and Emmanuel Brousseau. Fabrication of periodic nanostructures using dynamic plowing lithography with the tip of an atomic force microscope. *Applied Surface Science*, 427:1076–1083, 2018.

[14] Soroosh Daqiqeh Rezaei, Jinfa Ho, Tao Wang, Seeram Ramakrishna, and Joel K W Yang. Direct Color Printing with an Electron Beam. *Nano Letters*, 2020.

[15] Kishan Ashokbhai Patel, Ryan W. Grady, Kirby K.H. Smithe, Eric Pop, and Roman Sordan. Ultra-scaled MoS2 transistors and circuits fabricated without nanolithography. *2D Materials*, 7(1), 2020.

[16] Airán Ródenas, Min Gu, Giacomo Corrielli, Petra Paiè, Sajeev John, Ajoy K. Kar, and Roberto Osellame. Three-dimensional femtosecond laser nanolithography of crystals. *Nature Photonics*, 13(2):105–109, 2019.

[17] Wooyoung Shim, Adam B. Braunschweig, Xing Liao, Jinan Chai, Jong Kuk Lim, Gengfeng Zheng, and Chad A. Mirkin. Hard-tip, soft-spring lithography. *Nature*, 469(7331):516–521, 2011.

[18] He Liu, Stephanie Hoeppener, and Ulrich S. Schubert. Nanoscale Materials Patterning by Local Electrochemical Lithography. *Advanced Engineering Materials*, 18(6):890–902, 2016.

[19] Xiaolong Liu, Kan Sheng Chen, Spencer A. Wells, Itamar Balla, Jian Zhu, Joshua D. Wood, and Mark C. Hersam. Scanning Probe Nanopatterning and Layer-by-Layer Thinning of Black Phosphorus. *Advanced Materials*, 29(1), 2017.

[20] Valentyn Ishchuk, Elshad Guliyev, Cemal Aydogan, Ivan Buliev, Marcus Kaestner, Tzvetan Ivanov, Ahmad Ahmad, Alexander Reum, Steve Lenk, Claudia Lenk, Nikolay Nikolov, Thomas Glinsner, and Ivo W. Rangelow. Scanning probe-based high-accuracy overlay alignment concept for lithography applications. *Applied Physics A: Materials Science and Processing*, 123(1):1–12, 2017.

[21] Gang Yu Liu, Song Xu, and Yile Qian. Nanofabrication of self-assembled monolayers using scanning probe lithography. *Accounts of Chemical Research*, 33(7):457–466, 2000.

[22] Levente Tapasztó, Gergely Dobrik, Philippe Lambin, and László P. Biró. Tailoring the atomic structure of graphene nanoribbons by scanning tunnelling microscope lithography. *Nature Nanotechnology*, 3(7):397–401, 2008.

[23] Yu K. Ryu and Ricardo Garcia. Advanced oxidation scanning probe lithography. *Nanotechnology*, 28(14), 2017.

[24] Stephan Krämer, Ryan R. Fuierer, and Christopher B. Gorman. Scanning probe lithography using self-assembled monolayers. *Chemical Reviews*, 103(11):4367–4418, 2003.

[25] Arancha I. Dago, Yu K. Ryu, and Ricardo Garcia. Sub-20 nm patterning of thin layer WSe2 by scanning probe lithography. *Applied Physics Letters*, 109(16), 2016.

[26] Cong Wu, Tiffany G. Lin, Zhikun Zhan, Yi Li, Steve C.H. Tung, William C. Tang, and Wen J. Li. Fabrication of all-transparent polymer-based and encapsulated nanofluidic devices using nano-indentation lithography. *Microsystems and Nanoengineering*, 3, 2017.

[27] Kun Zhang, Qiang Fu, Nan Pan, Xinxin Yu, Jinyang Liu, Yi Luo, Xiaoping Wang, Jinlong Yang, and Jianguo Hou. Direct writing of electronic devices on graphene oxide by catalytic scanning probe lithography. *Nature Communications*, 3(May):1–6, 2012.

[28] Jaeho Choi, Wonhee Cho, Yeon Sik Jung, Hong Suk Kang, and Hee Tak Kim. Direct

Fabrication of Micro/Nano-Patterned Surfaces by Vertical-Directional Photofluidization of Azobenzene Materials. *ACS Nano*, 11(2):1320–1327, 2017.

[29] Samuel Tobias Zimmermann, Diederik W.R. Balkenende, Anna Lavrenova, Christoph Weder, and Jürgen Brugger. Nanopatterning of a Stimuli-Responsive Fluorescent Supramolecular Polymer by Thermal Scanning Probe Lithography. *ACS Applied Materials and Interfaces*, 9(47):41454–41461, 2017.

[30] Jinlong Gong, Darren J. Lipomi, Jiangdong Deng, Zhihong Nie, Xin Chen, Nicholas X. Randall, Rahul Nair, and George M. Whitesides. Micro-and nanopatterning of inorganic and polymeric substrates by indentation lithography. *Nano Letters*, 10(7):2702–2708, 2010.

[31] S. Masubuchi, M. Ono, K. Yoshida, K. Hirakawa, and T. MacHida. Fabrication of graphene nanoribbon by local anodic oxidation lithography using atomic force microscope. *Applied Physics Letters*, 94(8):2007–2010, 2009.

[32] Samuel Tobias Howell, Anya Grushina, Felix Holzner, and Juergen Brugger. Thermal scanning probe lithography—a review. *Microsystems and Nanoengineering*, 6(1):1–24, 2020.

[33] Fengwei Huo, Gengfeng Zheng, Xing Liao, Louise R. Giam, Jinan Chai, Xiaodong Chen, Wooyoung Shim, and Chad A. Mirkin. Beam pen lithography. *Nature Nanotechnology*, 5(9):637–640, 2010.

[34] Linhan Lin, Xiaolei Peng, Zhangming Mao, Wei Li, Maruthi N. Yogeesh, Bharath Bangalore Rajeeva, Evan P. Perillo, Andrew K. Dunn, Deji Akinwande, and Yuebing Zheng. Bubble-Pen Lithography. *Nano Letters*, 16(1):701–708, 2016.

[35] Martin Fuechsle, Jill A. Miwa, Suddhasatta Mahapatra, Hoon Ryu, Sunhee Lee, Oliver Warschkow, Lloyd C.L. Hollenberg, Gerhard Klimeck, and Michelle Y. Simmons. A single-atom transistor. *Nature Nanotechnology*, 7(4):242–246, 2012.

[36] Lianqing Liu, Jialin Shi, Meng Li, Peng Yu, Tie Yang, and Guangyong Li. Fabrication of Sub-Micrometer-Sized MoS2 Thin-Film Transistor by Phase Mode AFM Lithography. *Small*, 14(49):2–7, 2018.

[37] Soojin Lim, Boseok Kang, Donghoon Kwak, Wi Hyoung Lee, Jung Ah Lim, and Kilwon Cho. Inkjet-printed reduced graphene oxide/poly(vinyl alcohol) composite electrodes for flexible transparent organic field-effect transistors. *Journal of Physical Chemistry C*, 116(13):7520–7525, 2012.

[38] Qiyuan He, Chaoliang Tan, and Hua Zhang. Recent Advances in Cantilever-Free Scanning Probe Lithography: High-Throughput, Space-Confined Synthesis of Nanostructures and beyond. *ACS Nano*, 11(5):4381–4386, 2017.

[39] Shuping Pang, Hoi Nok Tsao, Xinliang Feng, and Klaus Mullen. Patterned graphene electrodes from solution-processed graphite oxide films for organic field-effect transistors. *Advanced Materials*, 21(34):3488–3491, 2009.

[40] Luis M. Campos, Ines Meinel, Rosette G. Guino, Martin Schierhorn, Nalini Gupta, Galen D. Stucky, and Craig J. Hawker. Highly versatile and robust materials for soft imprint lithography based on thiol-ene click chemistry. *Advanced Materials*, 20(19):3728–3733, 2008.

[41] Alee N. Broers, A. C.F. Hoole Andrew, and Joseph M. Ryan. Electron beam lithography - Resolution limits. *Microelectronic Engineering*, 32(1-4 SPEC. ISS.):131–142, 1996.

[42] John Melngailis. Focused ion beam lithography. *Nuclear Inst. and Methods in Physics Research, B*, 80-81(PART 2):1271–1280, 1993.

[43] Younan Xia and George M. Whitesides. Soft lithography. *Angewandte Chemie - International Edition*, 37(5):550–575, 1998.

[44] Ainhoa Urtizberea, Michael Hirtz, and Harald Fuchs. Ink transport modelling in Dip-Pen Nanolithography and Polymer Pen Lithography. *Nanofabrication*, 2(1):43–53, 2016.

[45] Laixia Yang, Iskander Akhatov, Mohammed Mahinfalah, and Bor Z. Jang. Nano-fabrication: A review. *Journal of the Chinese Institute of Engineers, Transactions of the Chinese Institute of Engineers,Series A/Chung-kuo Kung Ch'eng Hsuch K'an*, 30(3):441–446, 2007.

[46] Stephen Chou. Nanoimprint lithography. *Technology Review*, 106(1):42, 2003.

[47] David J. Guckenberger, Theodorus E. De Groot, Alwin M.D. Wan, David J. Beebe, and Edmond W.K. Young. Micromilling: A method for ultra-rapid prototyping of plastic microfluidic devices. *Lab on a Chip*, 15(11):2364–2378, 2015.

[48] Muhammad Imran, Rosly A. Rahman, Mukhtar Ahmad, Majid N. Akhtar, Arslan Usman, and Abdul Sattar. Fabrication of microchannels on PMMA using a low power CO 2 laser. *Laser Physics*, 26(9):96101, 2016.

[49] Daniel Day and Min Gu. Microchannel fabrication in PMMA based on localized heating using high-repetition rate femtosecond pulses. *Device and Process Technologies for Microelectronics, MEMS, and Photonics IV*, 6037(December 2005):603704, 2005.

[50] Eric MacDonald, Rudy Salas, David Espalin, Mireya Perez, Efrain Aguilera, Dan Muse, and Ryan B. Wicker. 3D printing for the rapid prototyping of structural electronics. *IEEE Access*, 2:234–242, 2014.

[51] Resul Saritas, Majed Al-Ghamdi, Taylan Das, and Eihab M Abdel-Rahman. A novel method for rapid microfabrication. In *International Design Engineering Technical Conferences and Computers and Information in Engineering Conference*, volume 51791, page V004T08A022. American Society of Mechanical Engineers, 2018.

[52] Brandon L. Thompson, Yiwen Ouyang, Gabriela R.M. Duarte, Emanuel Carrilho, Shannon T. Krauss, and James P. Landers. Inexpensive, rapid prototyping of microfluidic devices using overhead transparencies and a laser print, cut and laminate fabrication method. *Nature Protocols*, 10(6):875–886, 2015.

[53] Xueye Chen, Jienan Shen, and Mengde Zhou. Rapid fabrication of a four-layer PMMA-based microfluidic chip using CO2-laser micromachining and thermal bonding. *Journal of Micromechanics and Microengineering*, 26(10), 2016.

[54] Mohammad Yeakub Ali. Fabrication of microfluidic channel using micro end milling and micro electrical discharge milling. *International Journal of Mechanical and Materials Engineering*, 4(1):93–97, 2009.

[55] Shashi Prakash and Subrata Kumar. Fabrication of microchannels: A review. *Proceedings of the Institution of Mechanical Engineers, Part B: Journal of Engineering Manufacture*, 229(8):1273–1288, 2015.

[56] Muhammad Imran, Rosly A. Rahman, Mukhtar Ahmad, Majid N. Akhtar, Arslan Usman, and Abdul Sattar. Fabrication of microchannels on PMMA using a low power CO2 laser. *Laser Physics*, 26(9):0–7, 2016.

[57] Ting Fu Hong, Wei Jhong Ju, Ming Chang Wu, Chang Hsien Tai, Chien Hsiung Tsai, and Lung Ming Fu. Rapid prototyping of PMMA microfluidic chips utilizing a CO2 laser. *Microfluidics and Nanofluidics*, 9(6):1125–1133, 2010.

[58] Karthik Tappa and Udayabhanu Jammalamadaka. Novel biomaterials used in medical 3D printing techniques. *Journal of Functional Biomaterials*, 9(1), 2018.

[59] Germán Comina, Anke Suska, and Daniel Filippini. PDMS lab-on-a-chip fabrication using 3D printed templates. *Lab on a Chip*, 14(2):424–430, 2014.

[60] Dishit P Parekh, Collin Ladd, Lazar Panich, Khalil Moussa, and Michael D Dickey. 3d printing of liquid metals as fugitive inks for fabrication of 3d microfluidic channels. *Lab on a Chip*, 16(10):1812–1820, 2016.

[61] Yongda Yan, Yanquan Geng, Zhenjiang Hu, Xuesen Zhao, Bowen Yu, and Qi Zhang. Fabrication of nanochannels with ladder nanostructure at the bottom using AFM nanoscratching method. *Nanoscale Research Letters*, 9(1):1–13, 2014.

[62] B. Arda Gozen and O. Burak Ozdoganlar. Design and evaluation of a mechanical nanomanufacturing system for nanomilling. *Precision Engineering*, 36(1):19–30, 2012.

[63] Xiaohong Jiang, Guoyun Wu, Jingfang Zhou, Shujie Wang, Ampere A. Tseng, and Zuliang Du. Nanopatterning on silicon surface using atomic force microscopy with diamond-like carbon (DLC)-coated Si probe. *Nanoscale Research Letters*, 6:1–7, 2011.

[64] Nan Shen, Tayyab Suratwala, William Steele, Lana Wong, Michael D. Feit, Philip E. Miller, Rebecca Dylla-Spears, Richard Desjardin, and G. Pharr. Nanoscratching of

Optical Glass Surfaces Near the Elastic-Plastic Load Boundary to Mimic the Mechanics of Polishing Particles. *Journal of the American Ceramic Society*, 99(5):1477–1484, 2016.

[65] Xiaorui Zheng, Annalisa Calò, Edoardo Albisetti, Xiangyu Liu, Abdullah Sanad M. Alharbi, Ghidewon Arefe, Xiaochi Liu, Martin Spieser, Won Jong Yoo, Takashi Taniguchi, Kenji Watanabe, Carmela Aruta, Alberto Ciarrocchi, Andras Kis, Brian S. Lee, Michal Lipson, James Hone, Davood Shahrjerdi, and Elisa Riedo. Patterning metal contacts on monolayer MoS 2 with vanishing Schottky barriers using thermal nanolithography. *Nature Electronics*, 2(1):17–25, 2019.

[66] Robert Szoszkiewicz, Takashi Okada, Simon C. Jones, Tai De Li, William P. King, Seth R. Marder, and Elisa Riedo. High-speed, sub-15 nm feature size thermochemical nanolithography. *Nano Letters*, 7(4):1064–1069, 2007.

[67] E. Albisetti, K. M. Carroll, X. Lu, J. E. Curtis, D. Petti, R. Bertacco, and E. Riedo. Thermochemical scanning probe lithography of protein gradients at the nanoscale. *Nanotechnology*, 27(31), 2016.

[68] Richard D. Piner, Jin Zhu, Feng Xu, Seunghun Hong, and Chad A. Mirkin. 'Dip-pen' nanolithography. *Science*, 283(5402):661–663, 1999.

[69] Guoqiang Liu, Michael Hirtz, Harald Fuchs, and Zijian Zheng. Development of Dip-Pen Nanolithography (DPN) and Its Derivatives. *Small*, 15(21):1–9, 2019.

[70] Xuechang Zhou, Xiaolong Wang, Youde Shen, Zhuang Xie, and Zijian Zheng. Fabrication of arbitrary three-dimensional polymer structures by rational control of the spacing between nanobrushes. *Angewandte Chemie - International Edition*, 50(29):6506–6510, 2011.

[71] Yu K Ryu and Ricardo Garcia. Advanced oxidation Scanning Probe Lithography Instituto de Ciencia de Materiales de Madrid , CSIC , c / Sor Juana Inés de la Cruz 3 , 28049 Madrid , Spain * Present address : IBM Zurich Research Laboratory , Säumerstrasse 4 , 8803 Rüschlikon , Switzerland. Technical report, IBM Zurih Research Labaratory, 2016.

[72] Sacha Gómez-Moñivas, Juan José Sáenz, Montserrat Calleja, and Ricardo García. Field-Induced Formation of Nanometer-Sized Water Bridges. *Physical Review Letters*, 91(5):1–4, 2003.

[73] Yu K Ryu and Ricardo Garcia. Advanced oxidation scanning probe lithography. *Nanotechnology*, 28(14):142003, 2017.

[74] Antonio Garcia-Martin and Ricardo Garcia. Formation of nanoscale liquid menisci in electric fields. *Applied Physics Letters*, 88(12):1–3, 2006.

[75] Ricardo Garcia, Montserrat Calleja, and Heinrich Rohrer. Patterning of silicon surfaces with noncontact atomic force microscopy: Field-induced formation of nanometer-size water bridges. *Journal of Applied Physics*, 86(4):1898–1903, 1999.

[76] Jeong Heon Lee, Hyo Seong Lee, and Jae B Kwak. Mechanical characterization of polymeric thin films using nano cutting method. *International Journal of Precision Engineering and Manufacturing*, 21(6):1091–1097, 2020.

[77] SonoPlot sonoguide software. https://www.sonoplot.com/. Accessed: 2021-09-07.

[78] H E Enahoro and P L B Oxley. AN INVESTIGATION OF THE TRANSITION FROM A CONTINUOUS TO A DISCONTINUOUS CHIP IN ORTHOGONAL MACHINING tool rake angle depth of cut effective natural strain hydrostatic stress (

tensile positive ) shear yield stress of material distance along slip-lines of. Technical report, Manchester College of Science and Technology, 1961.

[79] J. M. Rodríguez, J. M. Carbonell, J. C. Cante, and J. Oliver. Continuous chip formation in metal cutting processes using the Particle Finite Element Method (PFEM). *International Journal of Solids and Structures*, 120:81–102, 2017.

[80] M. M'Hamdi, S. Bensalem, M. Boujelbene, D. Katundi, and E. Bayraktar. Effect of cutting parameters on the chip formation in orthogonal cutting. *AIP Conference Proceedings*, 1315(October 2014):1101–1106, 2010.

[81] Peng Bai, Guang Zhu, Zong Hong Lin, Qingshen Jing, Jun Chen, Gong Zhang, Jusheng Ma, and Zhong Lin Wang. Integrated multilayered triboelectric nanogenerator for harvesting biomechanical energy from human motions. *ACS Nano*, 7(4):3713–3719, 2013.

[82] Zhong Lin Wang, Jun Chen, and Long Lin. Progress in triboelectric nanogenerators as a new energy technology and self-powered sensors. *Energy and Environmental Science*, 8(8):2250–2282, 2015.

[83] Jinhui Nie, Zewei Ren, Jiajia Shao, Chaoran Deng, Liang Xu, Xiangyu Chen, Meicheng Li, and Zhong Lin Wang. Self-Powered Microfluidic Transport System Based on Triboelectric Nanogenerator and Electrowetting Technique. *ACS Nano*, 12(2):1491–1499, 2018.

[84] Jun Chen, Guang Zhu, Weiqing Yang, Qingshen Jing, Peng Bai, Ya Yang, Te Chien Hou, and Zhong Lin Wang. Harmonic-resonator-based triboelectric nanogenerator as a sustainable power source and a self-powered active vibration sensor. *Advanced Materials*, 25(42):6094–6099, 2013.

[85] Muhammed Kayaharman, Taylan Das, Gregory Seviora, Resul Saritas, Eihab Abdel-Rahman, and Mustafa Yavuz. Long-term stability of ferroelectret energy harvesters. *Materials*, 13(1):42, 2020.

[86] M Taylan Das, Kavinaath Murugan, Adam Tetreault, Connor Irvine, Andrej Rosic, Resul Saritas, Mustafa Yavuz, and Eihab M Abdel-Rahman. A triboelectric nanogenerator (teng) for pipeline monitoring. In *International Design Engineering Technical Conferences and Computers and Information in Engineering Conference*, volume 51852, page V008T10A055. American Society of Mechanical Engineers, 2018.

[87] Sun Woo Kim, Tae Gon Lee, Dae Hyeon Kim, Ku Tak Lee, Inki Jung, Chong Yun Kang, Seung Ho Han, Hyung Won Kang, and Sahn Nahm. Determination of the appropriate piezoelectric materials for various types of piezoelectric energy harvesters with high output power. *Nano Energy*, 57(December 2018):581–591, 2019.

[88] Mohamed Bendame, Eihab Abdel-Rahman, and Mostafa Soliman. Wideband, low-frequency springless vibration energy harvesters: Part i. *Journal of Micromechanics and Microengineering*, 26(11), 2016.

[89] Simiao Niu, Ying Liu, Sihong Wang, Long Lin, Yu Sheng Zhou, Youfan Hu, and Zhong Lin Wang. Theory of sliding-mode triboelectric nanogenerators. *Advanced Materials*, 25(43):6184–6193, 2013.

[90] Wei Xu, Long Biao Huang, Man Chung Wong, Li Chen, Gongxun Bai, and Jianhua Hao. Environmentally Friendly Hydrogel-Based Triboelectric Nanogenerators for Versatile Energy Harvesting and Self-Powered Sensors. *Advanced Energy Materials*, 7(1):1–8, 2017.

[91] Feng Ru Fan, Zhong Qun Tian, and Zhong Lin Wang. Flexible triboelectric generator. *Nano Energy*, 1(2):328–334, 2012.

[92] Jinsung Chun, Byeong Uk Ye, Jae Won Lee, Dukhyun Choi, Chong Yun Kang, Sang Woo Kim, Zhong Lin Wang, and Jeong Min Baik. Boosted output performance of triboelectric nanogenerator via electric double layer effect. *Nature Communications*, 7(May):1–9, 2016.

[93] R. D.I.G. Dharmasena, K. D.G.I. Jayawardena, C. A. Mills, J. H.B. Deane, J. V. Anguita, R. A. Dorey, and S. R.P. Silva. Triboelectric nanogenerators: Providing a fundamental framework. *Energy and Environmental Science*, 10(8):1801–1811, 2017.

[94] Congrui Jin, Danial Sharifi Kia, Matthew Jones, and Shahrzad Towfighian. On the contact behavior of micro-/nano-structured interface used in vertical-contact-mode triboelectric nanogenerators. *Nano Energy*, 27:68–77, 2016.

[95] Simiao Niu, Sihong Wang, Long Lin, Ying Liu, Yu Sheng Zhou, Youfan Hu, and Zhong Lin Wang. Theoretical study of contact-mode triboelectric nanogenerators as an effective power source. *Energy and Environmental Science*, 6(12):3576–3583, 2013.

[96] C. T. Pan, Y. J. Chen, Z. H. Liu, and C. H. Huang. Design and fabrication of LTCC electro-magnetic energy harvester for low rotary speed. *Sensors and Actuators, A: Physical*, 191:51–60, 2013.

[97] Yunlong Zi, Jie Wang, Sihong Wang, Shengming Li, Zhen Wen, Hengyu Guo, and Zhong Lin Wang. Effective energy storage from a triboelectric nanogenerator. *Nature Communications*, 7:1–8, 2016.

[98] Yang Wang, Ya Yang, and Zhong Lin Wang. Triboelectric nanogenerators as flexible power sources. *npj Flexible Electronics*, 1(1):1–9, 2017.

[99] Sihong Wang, Long Lin, and Zhong Lin Wang. Nanoscale triboelectric-effect-enabled energy conversion for sustainably powering portable electronics. *Nano Letters*, 12(12):6339–6346, 2012.

[100] Hassan Askari, Amir Khajepour, Mir Behrad Khamesee, Zia Saadatnia, and Zhong Lin Wang. Piezoelectric and triboelectric nanogenerators: Trends and impacts. *Nano Today*, 22:10–13, 2018.

[101] Guangguang Huang, Asif Abdullah Khan, Md Masud Rana, Chao Xu, Shuhong Xu, Resul Saritas, Steven Zhang, Eihab Abdel-Rahmand, Pascal Turban, Soraya Ababou-Girard, et al. Achieving ultrahigh piezoelectricity in organic–inorganic vacancy-ordered halide double perovskites for mechanical energy harvesting. *ACS Energy Letters*, 6(1):16–23, 2020.

[102] Myeong Lok Seol, Jin Woo Han, Dong Il Moon, and M. Meyyappan. Triboelectric nanogenerator for Mars environment. *Nano Energy*, 39(May):238–244, 2017.

[103] Seongsu Kim, Manoj Kumar Gupta, Keun Young Lee, Ahrum Sohn, Tae Yun Kim, Kyung Sik Shin, Dohwan Kim, Sung Kyun Kim, Kang Hyuck Lee, Hyeon Jin Shin, Dong Wook Kim, and Sang Woo Kim. Transparent flexible graphene triboelectric nanogenerators. *Advanced Materials*, 26(23):3918–3925, 2014.

[104] Sihong Wang, Long Lin, and Zhong Lin Wang. Triboelectric nanogenerators as self-powered active sensors. *Nano Energy*, 11:436–462, 2015.

[105] Guang Zhu, Zong Hong Lin, Qingshen Jing, Peng Bai, Caofeng Pan, Ya Yang, Yusheng Zhou, and Zhong Lin Wang. Toward large-scale energy harvesting by

a nanoparticle-enhanced triboelectric nanogenerator. *Nano Letters*, 13(2):847–853, 2013.

[106] Md Masud Rana, Asif Abdullah Khan, Guangguang Huang, Nanqin Mei, Resul Saritas, Boyu Wen, Steven Zhang, Peter Voss, Eihab Abdel-Rahman, Zoya Leonenko, et al. Porosity modulated high-performance piezoelectric nanogenerator based on organic/inorganic nanomaterials for self-powered structural health monitoring. *ACS Applied Materials & Interfaces*, 12(42):47503–47512, 2020.

[107] Asif Abdullah Khan, Md Masud Rana, Guangguang Huang, Nanqin Mei, Resul Saritas, Boyu Wen, Steven Zhang, Peter Voss, Eihab-Abdel Rahman, Zoya Leonenko, et al. Maximizing piezoelectricity by self-assembled highly porous perovskite–polymer composite films to enable the internet of things. *Journal of Materials Chemistry A*, 8(27):13619–13629, 2020.

[108] Zong Hong Lin, Yannan Xie, Ya Yang, Sihong Wang, Guang Zhu, and Zhong Lin Wang. Enhanced triboelectric nanogenerators and triboelectric nanosensor using chemically modified TiO2 nanomaterials. *ACS Nano*, 7(5):4554–4560, 2013.

[109] Zong Hong Lin, Gang Cheng, Wenzhuo Wu, Ken C. Pradel, and Zhong Lin Wang. Dual-mode triboelectric nanogenerator for harvesting water energy and as a self-powered ethanol nanosensor. *ACS Nano*, 8(6):6440–6448, 2014.

[110] Yeong Hwan Ko, Goli Nagaraju, Soo Hyun Lee, and Jae Su Yu. PDMS-based triboelectric and transparent nanogenerators with ZnO nanorod arrays. *ACS Applied Materials and Interfaces*, 6(9):6631–6637, 2014.

[111] Sang Jae Park, Myeong Lok Seol, Seung Bae Jeon, Daewon Kim, Dongil Lee, and

Yang Kyu Choi. Surface Engineering of Triboelectric Nanogenerator with an Electrodeposited Gold Nanoflower Structure. *Scientific Reports*, 5(July):1–7, 2015.

[112] Bhaskar Dudem, Nghia Dinh Huynh, Wook Kim, Dong Hyun Kim, Hee Jae Hwang, Dukhyun Choi, and Jae Su Yu. Nanopillar-array architectured PDMS-based triboelectric nanogenerator integrated with a windmill model for effective wind energy harvesting. *Nano Energy*, 42(September):269–281, 2017.

[113] Guang Zhu, Caofeng Pan, Wenxi Guo, Chih Yen Chen, Yusheng Zhou, Ruomeng Yu, and Zhong Lin Wang. Triboelectric-generator-driven pulse electrodeposition for micropatterning. *Nano Letters*, 12(9):4960–4965, 2012.

[114] Guang Zhu, Caofeng Pan, Wenxi Guo, Chih Yen Chen, Yusheng Zhou, Ruomeng Yu, and Zhong Lin Wang. Triboelectric-generator-driven pulse electrodeposition for micropatterning. *Nano Letters*, 12(9):4960–4965, 2012.

[115] Xianming He, Xiaojing Mu, Quan Wen, Zhiyu Wen, Jun Yang, Chenguo Hu, and Haofei Shi. Flexible and transparent triboelectric nanogenerator based on high performance well-ordered porous PDMS dielectric film. *Nano Research*, 9(12):3714–3724, 2016.

[116] M. A.E. Mahmoud, E. M. Abdel-Rahman, R. R. Mansour, and E. F. El-Saadany. Out-of-plane continuous electrostatic micro-power generators. *Sensors (Switzerland)*, 17(4):1–21, 2017.

[117] Alwathiqbellah Ibrahim, Abdallah Ramini, and Shahrzad Towfighian. Experimental and theoretical investigation of an impact vibration harvester with triboelectric transduction. *Journal of Sound and Vibration*, 416:111–124, 2018.

[118] Lina Chen, Xiaoling Wei, Xuechang Zhou, Zhuang Xie, Kan Li, Qifeng Ruan, Chaojian Chen, Jianfang Wang, Chad A. Mirkin, and Zijian Zheng. Large-Area Patterning of Metal Nanostructures by Dip-Pen Nanodisplacement Lithography for Optical Applications. *Small*, 13(43):1–6, 2017.

[119] Giorgio Mattana, Alberto Loi, Marion Woytasik, Massimo Barbaro, Vincent Noël, and Benoît Piro. Inkjet-Printing: A New Fabrication Technology for Organic Transistors. *Advanced Materials Technologies*, 2(10):1–27, 2017.

[120] Inés Temiño, Freddy G. Del Pozo, M. R. Ajayakumar, Sergi Galindo, Joaquim Puigdollers, and Marta Mas-Torrent. A Rapid, Low-Cost, and Scalable Technique for Printing State-of-the-Art Organic Field-Effect Transistors. *Advanced Materials Technologies*, 1(5):1–7, 2016.

[121] Yu Kyoung Ryu Cho, Colin D. Rawlings, Heiko Wolf, Martin Spieser, Samuel Bisig, Steffen Reidt, Marilyne Sousa, Subarna R. Khanal, Tevis D.B. Jacobs, and Armin W. Knoll. Sub-10 Nanometer Feature Size in Silicon Using Thermal Scanning Probe Lithography. *ACS Nano*, 11(12):11890–11897, 2017.

[122] Qiyuan He, Chaoliang Tan, and Hua Zhang. Recent Advances in Cantilever-Free Scanning Probe Lithography: High-Throughput, Space-Confined Synthesis of Nanostructures and beyond. *ACS Nano*, 11(5):4381–4386, 2017.

[123] Shashi Prakash and Subrata Kumar. Fabrication of microchannels: A review. *Proceedings of the Institution of Mechanical Engineers, Part B: Journal of Engineering Manufacture*, 229(8):1273–1288, 2015.

[124] Cong Wu, Tiffany G. Lin, Zhikun Zhan, Yi Li, Steve C.H. Tung, William C. Tang, and Wen J. Li. Fabrication of all-transparent polymer-based and encapsulated

nanofluidic devices using nano-indentation lithography. *Microsystems and Nanoengineering*, 3(October 2016), 2017.

[125] B. Arda Gozen and O. Burak Ozdoganlar. A rotating-tip-based mechanical nanomanufacturing process: Nanomilling. *Nanoscale Research Letters*, 5(9):1403–1407, 2010.

[126] Feng Ru Fan, Long Lin, Guang Zhu, Wenzhuo Wu, Rui Zhang, and Zhong Lin Wang. Transparent triboelectric nanogenerators and self-powered pressure sensors based on micropatterned plastic films. *Nano Letters*, 12(6):3109–3114, 2012.

[127] Van Long Trinh and Chen Kuei Chung. A Facile Method and Novel Mechanism Using Microneedle-Structured PDMS for Triboelectric Generator Applications. *Small*, 13(29):1–11, 2017.

[128] Mustafa Emre Karagozler, Ivan Poupyrev, Gary K Fedder, and Yuri Suzuki. Paper Generators : Harvesting Energy from Touching , Rubbing and Sliding. *User Interface Software and Technology (UIST)*, pages 23–30, 2013.

[129] Kai Tao, Lihua Tang, Jin Wu, Sun Woh Lye, Honglong Chang, and Jianmin Miao. Investigation of Multimodal Electret-Based MEMS Energy Harvester with Impact-Induced Nonlinearity. *Journal of Microelectromechanical Systems*, 27(2):276–288, 2018.

[130] J. Awrejcewicz, V. A. Krysko, M. V. Zhigalov, and A. V. Krysko. Contact interaction of two rectangular plates made from different materials with an account of physical nonlinearity. *Nonlinear Dynamics*, 91(2):1191–1211, 2018.

[131] Alwathiqbellah Ibrahim, Abdallah Ramini, and Shahrzad Towfighian. Experimental and theoretical investigation of an impact vibration harvester with triboelectric transduction. *Journal of Sound and Vibration*, 416:111–124, 2018.

[132] Jie Wang, Changsheng Wu, Yejing Dai, Zhihao Zhao, Aurelia Wang, Tiejun Zhang, and Zhong Lin Wang. Achieving ultrahigh triboelectric charge density for efficient energy harvesting. *Nature Communications*, 8(1):1–7, 2017.

[133] V. L. Trinh and C. K. Chung. Harvesting mechanical energy, storage, and lighting using a novel PDMS based triboelectric generator with inclined wall arrays and microtopping structure. *Applied Energy*, 213(June 2017):353–365, 2018.

[134] Meurig W. Williams. Triboelectric charging of insulators-evidence for electrons versus ions. *IEEE Transactions on Industry Applications*, 47(3):1093–1099, 2011.

[135] Meurig W. Williams. Triboelectric charging of insulators - Mass transfer versus electrons/ions. *Journal of Electrostatics*, 70(2):233–234, 2012.

# APPENDICES

# Appendix A

# Programming of nano 3D stage

## A.1 Using Arduino Software and Teensyduino Interface

Custom built 3D nanostage was driven via Teensy microcontroller. All programming and algorithm flow was coded using Arduino software then uploaded to the controller by an Teensyduino interface. A design of an interest was drawn and Gerber files (G code computer numerical control programming language) was obtained and then sent to Processing 3 software, which sends commands to the controller to drive 3D nanostage for fabrication.

## A.2 From Arduino Script Line

```
#define LINE_BUFFER_LENGTH 512
const int E1 = 3;
const int M1 = 4;
const int E2 = 11;
const int M2 = 12;
const int E3 = 5;
const int M3 = 8;
int EncoderAX=1;
int EncoderBX=2;
int EncoderAY=9;
int EncoderBY=14;
int EncoderAZ=0;
int EncoderBZ=6;
int ReverseLimitX=A1;
int ReverseLimitY=A2;
int ReverseLimitZ=A3;
int dirx;
int diry;
int dirz;
float TipDownPosition;
float TipSafePosition=800;
/*******global variable*****/
//counters variables
double Xpos;
double Ypos;
```

```
double Zpos;
int XaLastState;
int XaState;
int YaLastState;
int YaState;
int ZaLastState;
int ZaState;
int homeSpeedX=50;
int homeSpeedY=50;
int homeSpeedZ=50;
int scale=1;
boolean verbose = false;
boolean displacementNotdone=true;
int current_commandeG=100;
float speedX;
float speedY;
float countX;
struct point {
float x;
float y;
float z;
float f;};
void setup() {
Serial.begin( 9600 );
pinMode(M1, OUTPUT);
```

```
pinMode(E1, OUTPUT);
pinMode(M2, OUTPUT);
pinMode(E2, OUTPUT);
pinMode(M3, OUTPUT);
pinMode(E3, OUTPUT);
pinMode(EncoderAX,INPUT);
pinMode(EncoderBX,INPUT);
pinMode(EncoderBX,INPUT);
pinMode(EncoderBY,INPUT);
pinMode(EncoderAZ,INPUT);
pinMode(EncoderBZ,INPUT);
pinMode(ReverseLimitX,INPUT);
pinMode(ReverseLimitY,INPUT);
pinMode(ReverseLimitZ,INPUT);
XaLastState = digitalRead(EncoderAX);
YaLastState = digitalRead(EncoderAY);
ZaLastState = digitalRead(EncoderAZ);
Xpos=0;
Ypos=0;
Zpos=0;
attachInterrupt(digitalPinToInterrupt(EncoderAX), countx, CHANGE);
attachInterrupt(digitalPinToInterrupt(EncoderAY), county, CHANGE);
attachInterrupt(digitalPinToInterrupt(EncoderAZ), countz, CHANGE);}
void countx(){
XaState = digitalRead(EncoderAX);
```

```
if (XaState != XaLastState){
if (digitalRead(EncoderBX) != XaState) {
Xpos=Xpos+0.248045 ;
} else {
Xpos= Xpos-0.248045 ;}}
XaLastState = XaState;}
void county(){
YaState = digitalRead(EncoderAY);
if (YaState != YaLastState){
if (digitalRead(EncoderBY) != YaState) {
Ypos=Ypos+0.99609 ;
} else {
Ypos= Ypos-0.99609 ;}}
YaLastState = YaState;}
void countz(){
ZaState = digitalRead(EncoderAZ);
if (ZaState != ZaLastState){
if (digitalRead(EncoderBZ) != ZaState) {
Zpos=Zpos-0.248045 ;
} else {
Zpos= Zpos+0.248045 ;}}
ZaLastState = ZaState;}
void drawlineX(float newx, float SpeedX){
int value;
float dx=newx-Xpos;
```

```
boolean  displacementNotdone=true;
float i;
int dirmotorx;
int dirmotory;
Serial.print("dx=");
Serial.println(dx);
dx>= 0?dirx=1:dirx=-1;
if (dirx>0){
dirmotorx=LOW;
}else {dirmotorx=HIGH;}
while (displacementNotdone){
dirx >= 0?dx=newx-Xpos:dx=-newx+Xpos;
PWMX(SpeedX,dirmotorx);
if (analogRead(ReverseLimitY)==0 || analogRead(ReverseLimitX)==0){
digitalWrite(M2,HIGH);
analogWrite(E2, 0);
digitalWrite(M1,HIGH);
analogWrite(E1, 0);
digitalWrite(M3,HIGH);
analogWrite(E3, 0);
displacementNotdone=false;  }
if (dx<50){  SpeedX=60;}
else if (dx<200)
{ SpeedX=60;}
else if (dx<250)
```

```
{ SpeedX=60;}
{ SpeedX=60;}
else { SpeedX=SpeedX;}
//   Serial.print("SpeedX=");
//Serial.println(SpeedX);
if (dx<=0 ){
analogWrite(E1, 0);
//digitalWrite(M2,HIGH);
//analogWrite(E2, 0);
displacementNotdone=false;}}
displacementNotdone=true;}
void drawlineY(float newy, float SpeedY){
int value;
double b;
double slope;
float dy=newy-Ypos;
boolean  displacementdoneY=true;
float i;
int dirmotory;
dy>= 0?diry=1:diry=-1;
if (diry>0){
dirmotory=LOW;
}else {dirmotory=HIGH;}
Serial.print("dy: ");
Serial.println(dy);
```

```
while (displacementdoneY){
diry >= 0?dy=newy-Ypos:dy=-newy+Ypos;
PWMY(SpeedY,dirmotory);
if (analogRead(ReverseLimitY)==0 || analogRead(ReverseLimitX)==0){
digitalWrite(M2,HIGH);
analogWrite(E2, 0);
digitalWrite(M1,HIGH);
analogWrite(E1, 0);
digitalWrite(M3,HIGH);
analogWrite(E3, 0);
displacementdoneY=false;}
if (dy<130){  SpeedY=58;}
else if (dy<250)
{ SpeedY=59;}
else if (dy<500)
{ SpeedY=59;}
else { SpeedY=SpeedY;}
if (dy<=0 ){
digitalWrite(M2,HIGH);
analogWrite(E2, 0);
displacementdoneY=false;}}
displacementdoneY=true;
Serial.print("Ypos: ");
Serial.println(Ypos);}
void drawlineXY(float newx, float SpeedX, float newy, float SpeedY){
```

```
int value;
double b;
double Aslope;
double Tslope;
double ErrorY;
double ErrorX;
float dx=newx-Xpos;
float dy=newy-Ypos;
float Xposi=Xpos;
float Yposi=Ypos;
boolean  displacementNotdoneX=true;
boolean  displacementNotdoneY=true;
float i;
double Slopeerror;
int dirmotorx;
int dirmotory;
Serial.print("dy=");
Serial.println(dy);
Serial.print("dx=");
Serial.println(dx);
dx>= 0?dirx=1:dirx=-1;
dy>= 0?diry=1:diry=-1;
if (dirx>0){
dirmotorx=LOW;
}else {dirmotorx=HIGH;}
```

```
if (diry>0){
dirmotory=LOW;
}else {dirmotory=HIGH;}
diry >= 0?dy=newy-Ypos:dy=-newy+Ypos;
while (displacementNotdoneX){
dirx >= 0?dx=newx-Xpos:dx=-newx+Xpos;
if (analogRead(ReverseLimitY)==0 || analogRead(ReverseLimitX)==0){
digitalWrite(M2,HIGH);
analogWrite(E2, 0);
digitalWrite(M1,HIGH);
analogWrite(E1, 0);
digitalWrite(M3,HIGH);
analogWrite(E3, 0);
displacementNotdoneX=false;
return;}
PWMX(SpeedX, dirmotorx);
if (dx<130){  SpeedX=55;}
else if (dx<250)
{ SpeedX=55;}
else if (dx<500)
{ SpeedX=55;}
else { SpeedX=SpeedX;}
if (dx<=0 ){
digitalWrite(M1,HIGH);
analogWrite(E1, 0);
```

```
// digitalWrite(M2,HIGH);
// analogWrite(E2, 0);
displacementNotdoneX=false;}}
while (displacementNotdoneY){
diry >= 0?dy=newy-Ypos:dy=-newy+Ypos;
if (analogRead(ReverseLimitY)==0 || analogRead(ReverseLimitX)==0){
digitalWrite(M2,HIGH);
analogWrite(E2, 0);
digitalWrite(M1,HIGH);
analogWrite(E1, 0);
digitalWrite(M3,HIGH);
analogWrite(E3, 0);
displacementNotdoneY=false;
return;}
PWMY(SpeedY, dirmotory);
if (dy<130){  SpeedY=57;}
else if (dy<250)
{ SpeedY=59;}
else if (dy<500)
{ SpeedY=59;}
else { SpeedY=SpeedY;}
if (dy<=0 ){
analogWrite(E2, 0);}}
displacementNotdoneY=true;
displacementNotdoneX=true;}
```

```
void drawlineZ(float newz, float SpeedZ){
int dirmotorz;
int dzdir;
int dz;
displacementNotdone=true;
if (Zpos>TipDownPosition){dzdir==
(-Zpos+(TipDownPosition-TipSafePosition));} else
 {dzdir=(Zpos-(TipDownPosition-TipSafePosition));}
Serial.print("SpeedZ=");
if (newz>=0 and Zpos<(TipDownPosition-TipSafePosition)){
dirmotorz=LOW;
SpeedZ=75;
}else if(newz>=0 and Zpos>(TipDownPosition-TipSafePosition)){
dirmotorz=HIGH;
SpeedZ=75;}
else if(newz<0 and Zpos<(TipDownPosition-TipSafePosition)){
dirmotorz=LOW;
SpeedZ=75;}
else if(newz<0 and Zpos>(TipDownPosition-TipSafePosition)){
dirmotorz=LOW;
SpeedZ=75;}
while (displacementNotdone){//while the displament is not done
if
(newz>=0){dzdir>=0?dz=(Zpos-(TipDownPosition-TipSafePosition))://
dz=(-Zpos+(TipDownPosition-TipSafePosition));}
```

```
else {dz=-Zpos+TipDownPosition;}
if (analogRead(ReverseLimitY)==0 || analogRead(ReverseLimitX)==0){
digitalWrite(M2,HIGH);
analogWrite(E2, 0);
digitalWrite(M1,HIGH);
analogWrite(E1, 0);
digitalWrite(M3,HIGH);
analogWrite(E3, 0);
displacementNotdone=false;
return;}
PWMZ(SpeedZ, dirmotorz);
if (dz<150){ SpeedZ=75;}
else if (dz<300)
{ SpeedZ=75;}
else { SpeedZ=SpeedZ;}
if (dz<0){
digitalWrite(M3,LOW);
analogWrite(E3, 0);   //PWM Speed Control
displacementNotdone=false;}}
//    displacementNotdone=true;}
void Home_pos(){
bool Homepos=true;
int homeSpeedX=100;
int homeSpeedY=100;
int homeSpeedZ=150;
```

```
int counter=0;
if (analogRead(ReverseLimitZ)!=0){
while (counter<200){
if (analogRead(ReverseLimitZ)==0){
digitalWrite(M3,LOW);
analogWrite(E3, 0);
}else {
digitalWrite(M3,HIGH);
analogWrite(E3, homeSpeedZ);  }
delay(10);
counter++;}}
while (Homepos){
delay(100);
if (analogRead(ReverseLimitX)==0  and analogRead(ReverseLimitY)==0
and analogRead(ReverseLimitZ)==0 ){
Homepos=false; }
if (analogRead(ReverseLimitX)==0 ){
homeSpeedX=0;
}else {homeSpeedX=150;}
//check Y HomePosition and set speed motor 0
if (analogRead(ReverseLimitY)==0){
homeSpeedY=0;
}else {homeSpeedY=150;}
if (analogRead(ReverseLimitZ)==0){
homeSpeedZ=0;
```

```
}else {homeSpeedZ=150;}
digitalWrite(M2,HIGH);
analogWrite(E2, homeSpeedY);
digitalWrite(M1,HIGH);
analogWrite(E1, homeSpeedX);
digitalWrite(M3,HIGH);
analogWrite(E3, homeSpeedZ);
void RelativeX(float newx){
float SpeedX=60;
boolean displacementdoneX=true;
float SpeedY=50;
float relativespeed=100;
float dx;
float dirx;
float dirmotorx;
newx>= 0?dirx=1:dirx=-1;
if (dirx>0){
dirmotorx=LOW;
}else {dirmotorx=HIGH;}
Serial.print("newx=");
Serial.println(newx);
while (displacementdoneX){
if ( newx >0) {dx=newx-Xpos;}else {dx=-newx+Xpos;}
PWMX(SpeedX,dirmotorx);
if (analogRead(ReverseLimitY)==0 || analogRead(ReverseLimitX)==0){
```

```
digitalWrite(M2,HIGH);
analogWrite(E2, 0);
digitalWrite(M1,HIGH);
analogWrite(E1, 0);
digitalWrite(M3,HIGH);
analogWrite(E3, 0);
displacementdoneX=false;  }
//  Serial.print("dx=");
//Serial.println(dx);
if (dx<75){  SpeedX=50;}
else if (dx<300)
{ SpeedX=57;}
else { SpeedX=SpeedX;}
if (dx<=0 ){
digitalWrite(M1,HIGH);
analogWrite(E1, 0);
Serial.print("Xpos=");
Serial.println(Xpos);
// digitalWrite(M2,HIGH);
// analogWrite(E2, 0);
displacementdoneX=false;}}
displacementdoneX=true;
Xpos=0; }
void RelativeY(float newy){
boolean displacementdoneY=true;
```

```
float SpeedY=50;
float relativespeed=100;
float dy;
float diry;
float dirmotory;
newy>= 0?diry=1:diry=-1;
if (diry>0){
dirmotory=LOW;
}else {dirmotory=HIGH;}
while (displacementdoneY){
if ( newy >0) {dy=newy-Ypos;}else {dy=-newy+Ypos;}
PWMY(SpeedY,dirmotory);
if (analogRead(ReverseLimitY)==0 || analogRead(ReverseLimitX)==0) {
digitalWrite(M2,HIGH);
analogWrite(E2, 0);
digitalWrite(M1,HIGH);
analogWrite(E1, 0);
digitalWrite(M3,HIGH);
analogWrite(E3, 0);
displacementdoneY=false;}
else {SpeedY=SpeedY;}
if (dy<200){  SpeedY=57;}
else if (dy<500)
{ SpeedY=59;}
else { SpeedY=SpeedY;}
```

```
if (dy<=0 ){
digitalWrite(M2,HIGH);
analogWrite(E2, 0);
displacementdoneY=false;}} displacementdoneY=true;
delay(400);
Ypos=0;}
void RelativeZ(float newz){
boolean displacementdoneZ=true;
float SpeedZ=65;
float dz;
float dirz;
float dirmotorz;
newz>= 0?dirz=1:dirz=-1;
if (dirz>0){
dirmotorz=LOW;
}else {dirmotorz=HIGH;}
while (displacementdoneZ){
if ( newz >0) {dz=newz-Zpos;}else {dz=-newz+Zpos;}
PWMZ(SpeedZ,dirmotorz);
if (analogRead(ReverseLimitY)==0
|| analogRead(ReverseLimitX)==0 || analogRead(ReverseLimitZ)==0) {
digitalWrite(M2,HIGH);
analogWrite(E2, 0);
digitalWrite(M1,HIGH);
analogWrite(E1, 0);
```

```
digitalWrite(M3,HIGH);
analogWrite(E3, 0);
displacementdoneZ=false;}
if (dz<75){  SpeedZ=75;}
else if (dz<300)
{ SpeedZ=75;}
else { SpeedZ=SpeedZ;}
if (dz<=0 ){
digitalWrite(M3,HIGH);
analogWrite(E3, 0);
displacementdoneZ=false;}
if (analogRead(ReverseLimitZ)==0){
digitalWrite(M3,LOW);
analogWrite(E3, 0);  }}
displacementdoneZ=true;
delay(400);
Serial.print("Zpos=");
Serial.println(Zpos);
Zpos=0; }
void PWMX(int SpeedX, int dirmotorx){
digitalWrite(M1,dirmotorx);
analogWrite(E1, SpeedX);   //PWM Speed Control }
void PWMY(int SpeedY, int dirmotory){
digitalWrite(M2, dirmotory);
analogWrite(E2, SpeedY);   //PWM Speed Control             }
```

```
void PWMZ(float SpeedZ, float dirmotorz){
digitalWrite(M3, dirmotorz);
analogWrite(E3, SpeedZ); }  //PWM Speed Control  }
void PWMXY(int SpeedX, int dirmotorx, int SpeedY, int dirmotory ){
digitalWrite(M1,dirmotorx);
analogWrite(E1, SpeedX);   //PWM Speed Control
digitalWrite(M2,dirmotory);
analogWrite(E2, SpeedY);   //PWM Speed Control
}}
```